10-22-2018

Observation of High-Energy Gamma-Rays with the Calorimetric Electron Telescope (CALET) On-board the International Space Station

Nicholas Wade Cannady
Louisiana State University and Agricultural and Mechanical College

OBSERVATION OF HIGH-ENERGY GAMMA-RAYS WITH THE CALORIMETRIC ELECTRON TELESCOPE (CALET) ON-BOARD THE INTERNATIONAL SPACE STATION

A Dissertation

Submitted to the Graduate Faculty of the
Louisiana State University and
Agricultural and Mechanical College
in partial fulfillment of the
requirements for the degree of
Doctor of Philosophy

in

The Department of Physics and Astronomy

by
Nicholas Wade Cannady
B.S., Louisiana State University, 2011
December 2018

To Laura and Mom

Acknowledgments

First and foremost, I would like to thank my partner, Laura, for the constant and unconditional support that she has provided during the research described in this thesis and my studies in general. Without her, this undertaking would not have been possible.

I would also like to thank my parents and grandparents for encouraging me to follow my dreams and for pushing me throughout my life to be my best.

There have been several other teachers, mentors, and friends that have kindled my interest in discovery and learning, believed in me when I needed it, and helped me to grow into the person I am today. I will not attempt to enumerate these people for fear of omission, but my deepest appreciation is extended to them as well.

I would like to thank my advisor, Dr. Michael Cherry, for his guidance in this and in other research efforts in which I have participated while at LSU. I have benefited immeasurably from his experience, both scientific and diplomatic. I look forward to hopefully continuing some of the work I have begun with Mike as my career continues.

In addition, I would like to thank Dr. T. Gregory Guzik for his close involvement and leadership in my research on the CALET project. His knowledge and rigor have been a great inspiration for me, and his discipline is a shining example for my own developing planning and organizational skills.

Other CALET collaborators have been instrumental and indispensable in the following work. I would like to personally thank Dr. Yoichi Asaoka for his contributions and discussions to the gamma-ray analysis and the CALET results as a whole. I would also like to thank Profs. Shoji Torii and Masaki Mori for their close attention to my work and the suggestions that they have offered me through the past few years.

I would like to thank the Board of Regents for the research fellowship which supported me for my first four years of graduate work and enabled my involvement in the Saturday Science outreach program. In addition, I would like to thank the LaSPACE Program for the Graduate Student Research Award that has provided additional financial support for my

work. My travel to conferences has been, in part, paid for by the graduate student travel awards donated by the Coates family. These travel experiences have been enormously beneficial to my growth as a scientist, and for that I am deeply grateful.

Of course, this work would not have been possible without the funding for the CALET project from JAXA, NASA (via grant NNX11AE01G), and ASI and the leadership provided by the PIs, including Professors Shoji Torii, John Wefel, and Pier Simone Marrocchesi. I appreciate the opportunity to be a part of the CALET Collaboration and am thankful to many other members for their foundational work as well as their insights and feedback to my own efforts.

Preface

This thesis is intended to satisfy the requirements for the Doctor of Philosophy degree in Physics. As such, it is structured to motivate the observation of photons in the GeV energy regime, to motivate and present the instrumentation and response of the CALET instrument as they pertain to gamma-ray detection, and to demonstrate the capability of the calorimeter to contribute results to the gamma-ray community in a meaningful way.

The first of these three aims is addressed by the introductory chapter of the thesis. In it, an overview of high-energy gamma-ray transients is presented, with an emphasis on the multi-messenger observation opportunities now available with the LIGO and Virgo gravitational wave observatories and the IceCube neutrino observatory.

In the following chapters, the CALET instrument is described in detail, including a discussion of the structure and calibration of the calorimeter. The reconstruction of electromagnetic events and the selection process for gamma-rays is presented, and the resulting instrument response functions are derived.

Finally, observations of high-energy gamma-ray sources made by CALET are shown and discussed. These include measurement of the signal from bright point-sources and the diffuse galactic emission. These sources have been well-characterized prior to the CALET launch and the consistency of our results provides a valuable validation of the derived instrument response. Finally, the results and prospects for observing transient counterpart emission to gamma-ray bursts and gravitational wave events with the calorimeter are discussed in detail.

Table of Contents

List of Tables

List of Figures

Abstract

The CALorimetric Electron Telescope (CALET) is a multi-instrument high-energy astrophysics observatory deployed to the International Space Station (ISS) in August 2015. The primary instrument is the calorimeter (CAL), which is intended for measurement of the cosmic ray electron flux in the energy range 10 GeV - 20 TeV. The CAL is also sensitive to gamma-rays in the energy range 1 GeV - 10 TeV and protons and nuclei up to PeV energies. Also present on the CALET payload are an Advanced Stellar Compass (ASC) for the fine determination of the pointing direction and the CALET Gamma-ray Burst Monitor (CGBM) for the observation of hard x-ray/soft gamma-ray emission from gamma-ray bursts (GRBs). This work focuses on the capabilities and current results of the CAL for observation of gamma-ray sources in the GeV-energy regime. The methodology for the isolation of a gamma-ray dataset is presented and the resulting efficiencies and instrument response functions (IRFs) are derived from Monte Carlo simulated events. These results are validated by comparison with the first two years of flight data from CALET and the consistency with established measurements from other instruments is shown. Finally, independent CALET observations are presented, with an emphasis on the potential for detection of high-energy electromagnetic emission from transient events, including short and long GRBs, gravitational wave events seen by the LIGO/Virgo observatories, and high-energy astrophysical neutrino observations.

Chapter 1. Introduction

1.1 Gamma Rays and Cosmic Ray Accelerators

Cosmic rays are high-energy charged particles from space, originally seen by Victor Hess in the early twentieth century. Over the following decades, the composition, energy distribution, and incident directions of these particles were studied in great detail and the search for astrophysical systems which accelerate these particles was launched. In the process, the study of cosmic rays has been instrumental in advancing the field of high-energy physics, long serving as the laboratory source of high-energy nuclear interactions before the advent of large particle colliders. To this day, cosmic rays provide a window to fundamental physics in energy regimes unreachable in terrestrial experiments.

The presence of galactic and intergalactic magnetic fields creates a critical challenge to probing the sources of cosmic rays. The galactic magnetic field effectively diffuses these particles during propagation such that the signal we see at Earth is largely isotropic, although tantalizing recent results by the Auger experiment suggest a dipole anisotropy at ultra-high-energies (UHE) (Aab et al., 2017). While this is strong evidence that UHE cosmic rays have an extragalactic origin, energy loss rates for lower energy charged particles require a galactic origin. Unfortunately, due the loss of directionality during propagation, it is impossible to directly point a galactic cosmic ray back to the system where it was accelerated. Therefore, although the spectral shapes of various cosmic-ray species and the energy budgets of potential source classes can be very suggestive when combined, confirmation of an astrophysical system as a cosmic accelerator and direct analysis of the mechanisms acting therein require observations by different means.

The production of high-energy gamma rays is tied closely to cosmic ray acceleration and interaction. Galactic diffuse gamma rays originate primarily from the nuclear interactions of cosmic-ray protons (and other nuclei) with gas clouds in the interstellar medium, creating π^0 (in addition to $\pi^{\pm}$) that subsequently decay to photons. Leptonic modes of emission are seen clearly in systems such as pulsars, where electrons are accelerated in strong magnetic

fields. These electrons directly emit synchrotron x-rays and gamma rays, in addition to boosting the energies in existing photon fields through inverse Comptonization. Critically, photons lack electric charge and are therefore not deflected by magnetic fields, allowing for the clear investigation of individual systems that potentially act as cosmic ray accelerators.

1.2 Gamma-ray Transients

Although other observational results are included in the following chapters as a matter of validation, this thesis is focused primarily on the establishment of a framework for the analysis of gamma-ray transient events in GeV energies with the CALET calorimeter, which is described in detail in the following chapter. Gamma-ray transients are systems associated with intense energy release over relatively short timescales. The high-energy photon signal from these events is key in understanding the acceleration mechanisms in these systems. At GeV energies, two source classes are predominantly seen: gamma-ray bursts (GRBs) and flares of active galactic nuclei (AGN).

GRBs are extremely bright events with characteristic timescales on the order of seconds that are distributed isotropically on the sky. The durations (T_{90}, the time within which 90% of total associated events are seen) span the range from milliseconds to kiloseconds and are observed to follow a bimodal distribution (Kouveliotou et al. (1993); see let panel of Figure 1.1). GRBs are classified as either short (sGRBs; $T_{90} < 2$ seconds) or long (lGRBs; $T_{90} > 2$ seconds), and these populations are thought to arise from different astrophysical phenomena. Progenitors of sGRBs are generally considered to be compact binary mergers (NS-NS or NS-BH), whereas lGRBs are associated with core-collapse supernovae. In spite of the different classes of progenitors, the HE (GeV) emission from GRBs, initially observed by the EGRET (Merck et al. (1994), Gonzàlez et al. (2003)) instrument on board the Compton Gamma Ray Observatory and subsequently studied in depth by the Large Area Telescope (LAT; Ackermann et al. (2013a)) on the Fermi Gamma Ray Observatory, is thought to arise from similar underlying physical processes in both sGRBs and lGRBs.

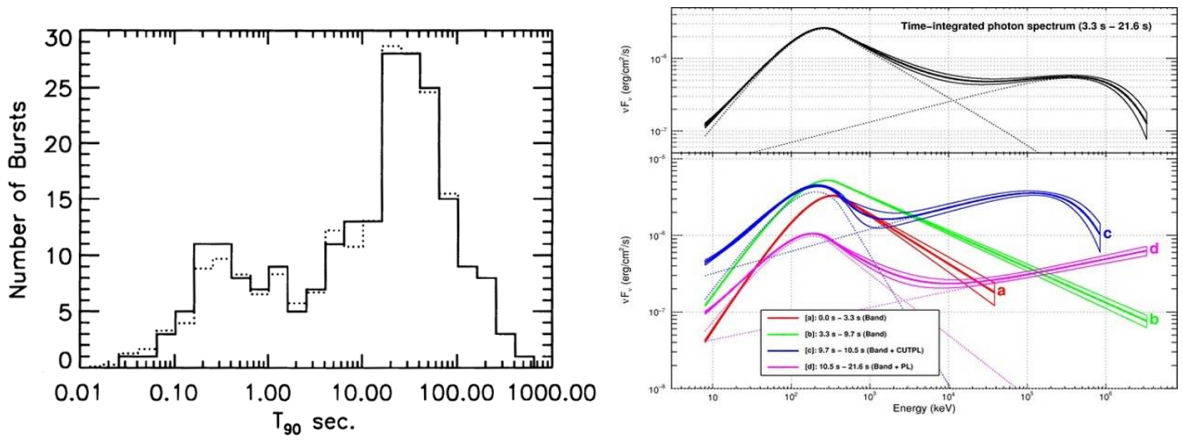

Figure 1.1: Time- and energy-dependence of GRBs. *Left:* The distribution of T_{90} for the 222 GRBs in the first CGRO/BATSE catalog. The division between the populations at 2 seconds is chosen to classify short vs. long GRBs. *Image credit:* Kouveliotou et al. (1993). *Right:* Spectral energy distribution for the GRB 090926A as measured by Fermi-GBM and Fermi-LAT. The top panel shows the time-averaged best-fit curve and the bottom panel shows the emergence of the high-energy afterglow component. *Image credit:* Ackermann et al. (2011).

The gamma-ray spectra of GRBs are highly non-thermal and can be separated into prompt and afterglow components (Nava, 2018). The prompt emission is likely generated by the acceleration of charged particles to relativistic energies in the cataclysmic explosion of the progenitor system, although the exact nature of this emission is still not fully understood. Relativistic beaming of thermal and/or synchrotron emission of these accelerated particles could be responsible for the prompt phase signal. The afterglow component (see right panel of Figure 1.1) is thought to arise from so-called external shocks as the accelerated material interacts with the surrounding medium, slowing down and producing bremsstrahlung. The necessity of jet formation in these systems as opposed to a more isotropic breakout of the particles from a surrounding cocoon of ejecta (such as with a Wolf-Rayet star) is still a point of debate.

AGN are a broad class of systems which result from accretion onto the supermassive black holes at the centers of distant galaxies. Initially seen in radio as quasars, these systems exhibit broadband emission and characteristic emission lines. Ejected material

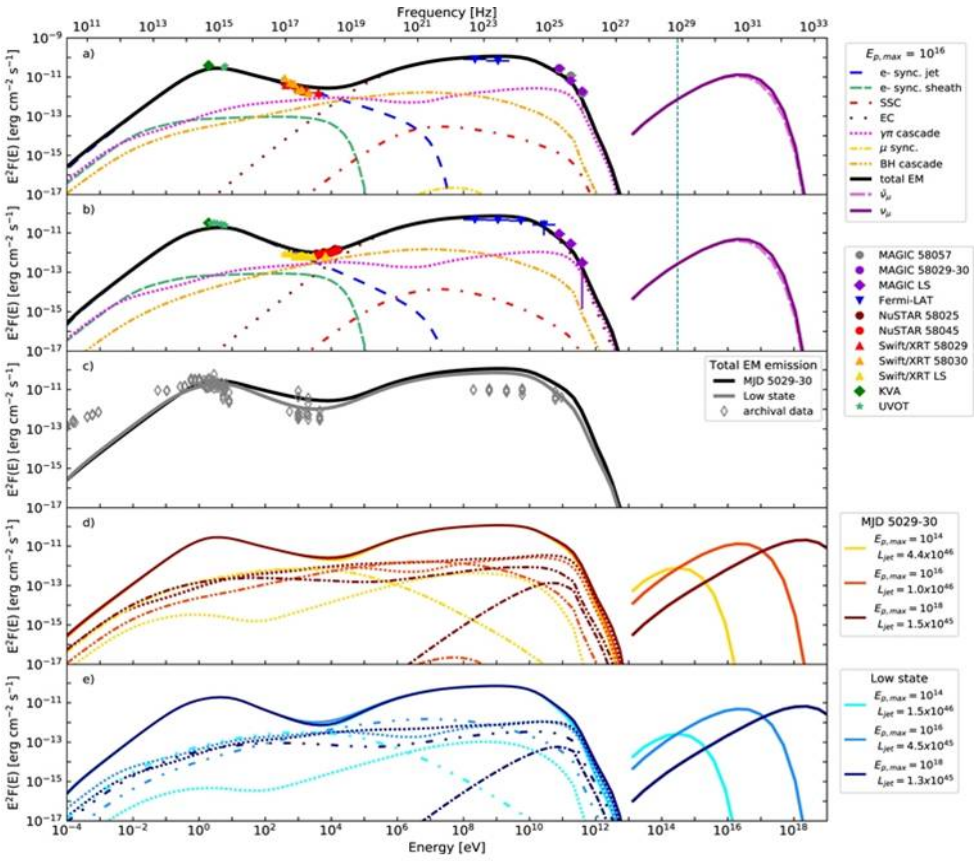

Figure 1.2: Broadband spectrum of the blazar TXS 0506+056. Flux in electromagnetic radiation and modeled neutrinos for the flare and quiescent states. Curves show the modeled contributions from various physical processes assuming some hadronic acceleration in the jets. *Image credit:* Ansoldi et al. (2018).

is thrown off in large polar jets of relativistic particles. When viewed on-axis of the jet, the systems are known as blazars, and gamma ray detectors at the Earth can see the boosted emission (thermal, synchrotron, inverse Compton) from these relativistic particles. Although these systems can be persistent sources (especially in VHE gamma rays seen from large ground-based arrays), strong flares are also seen. Typical spectral energy diagrams of blazars show two strong, distinct components (e.g. Figure 1.2). The lower component peaks in soft x-ray energies and is attributed to synchrotron emission of a leptonic (electron + positron) population with magnetic fields in the jet. The peak at higher (GeV) energies

is less well-understood, and could have contributions from inverse Comptonization from the leptonic population, synchrotron emission from protons, and π^0 decay.

1.3 Multi-Messenger Observations

Recently, multi-messenger observations of astrophysical systems have begun to bear fruit with the beginning of the science runs of the Advanced LIGO and Virgo gravitational wave (GW) interferometers and the continued operation of the IceCube Neutrino Observatory (among others). In the past year, joint detections of electromagnetic (EM) signals with triggers from these instruments have been used to make valuable observations. First, the NS-NS merger event GW170817 by LIGO (with the non-detection by Virgo reducing the error region on the sky) was detected in coincidence (Abbott et al., 2017a) with a sGRB (GRB 170817A) by the Fermi Gamma-ray Burst Monitor (GBM). This detection, in addition to providing the first clear connection between a sGRB and a progenitor system, allowed for the optical discovery by the Swope telescope (Coulter et al., 2017), which in turn allowed for a broadband EM follow-up campaign.

Although the joint detections by LIGO and GBM establish a connection between NS-NS mergers and sGRBs, it remains unclear how typical this evolutionary path is. The sGRB associated with GW170817 was considered underluminous based on the GBM measurements given the redshift inferred by the GW and follow-up detections. Unfortunately, HE observations were not available from Fermi because the LAT was turned off for passage through the South Atlantic Anomaly (SAA). The relatively high peak energy observed by GBM together with the externally inferred system parameters disfavors an isotropic shock in a cocoon of material, suggesting that a relativistic jet was formed in the merger (Veres et al., 2018). The viewing of this jet off-axis potentially explains the underluminosity of the gamma-ray signal. While afterglows were seen at other frequency bands, follow-up observations in GeV energies yielded only upper limits on HE emission.

An additional breakthrough in multi-messenger observations was announced in July 2018, when the IceCube collaboration announced the detection of a HE neutrino event

with direction consistent with a flaring AGN (TXS 0506+056) seen by Fermi-LAT (IceCube Collaboration et al., 2018). The subsequent investigation of background signals for the IceCube experiment demonstrated an excess of events seen in this direction in 2015, suggesting that the system could have exhibited a neutrino flare. While IceCube had previously shown HE neutrinos from cosmogenic origins (such as cosmic-ray interactions with interstellar material), this detection marked the first event consistent with an acceleration site, potentially giving direct evidence for the acceleration of cosmic-ray hadrons in a system.

The scientific value of these events demonstrates the wealth of information available from multi-messenger observations. With the potential for broadband EM follow-up, gamma ray detection not only has merit in its own energy regime, but can provide the localization necessary for subsequent detection at other frequencies. It is therefore critical in the upcoming observation campaigns for large field-of-view (FOV) gamma ray detectors with localization potential consistently viewing as much of the sky as possible. CALET, designed as a telescope for very high energy electrons, is one such detector, with sensitivity to photons in the range from one to several hundreds of GeV in a FOV of radius $> 45°$.

Chapter 2. The CALorimetric Electron Telescope (CALET)

2.1 Motivation - Cosmic-ray electrons

The motivations for focused study of cosmic-ray electrons are twofold. First, due to the relatively fast energy loss of electrons due to synchrotron radiation in the galactic magnetic field, the range of these particles is very short compared to their hadronic counterparts. Radiative energy losses in the interstellar medium for electrons suggest a lifetime on the order of 10^5 years at 1 TeV, corresponding to a pathlength of $\sim$300 parsec. The ratios of secondary to primary cosmic-ray nuclei can be used to estimate the age of the primary species, typically on the order of $\sim 10^7$ years. This suggests that any broad feature in the energy spectrum of cosmic-ray electrons would be due to nearby sites of acceleration. Since cosmic rays are effectively diffused by the galactic magnetic field, their trajectories are scrambled and tracing their direction back to individual sites is impossible. Thus the association of a population of electrons (and the details of their energy distribution) to a particular source with observable magnetic field strength, surrounding environment, and other attributes opens the door for greatly advancing the modeling of cosmic ray acceleration. Second, many theoretical models for dark matter constituent particles predict a decay mode to an electron-positron pair with center-of-mass energy equal to the original particle mass, typically in the GeV-TeV regime. The detection of a narrow resonance peak in the cosmic-ray electron spectrum at these energies would potentially be a huge step forward in the understanding of dark matter, a fundamental unresolved question in modern physics.

Results from previous experiments in the GeV to hundreds of GeV energy range have at times suggested features beyond a smooth spectrum, although often inconsistent (e.g. Yoshida et al. (2008), Chang et al. (2008), Ackermann et al. (2010)). These experiments have either been borne by high-altitude balloon flights or put into Earth orbit, and have detected particles primarily using a magnet or a calorimeter. Balloon flights are both scientifically valuable and are often used as proof-of-concept for instruments intended for

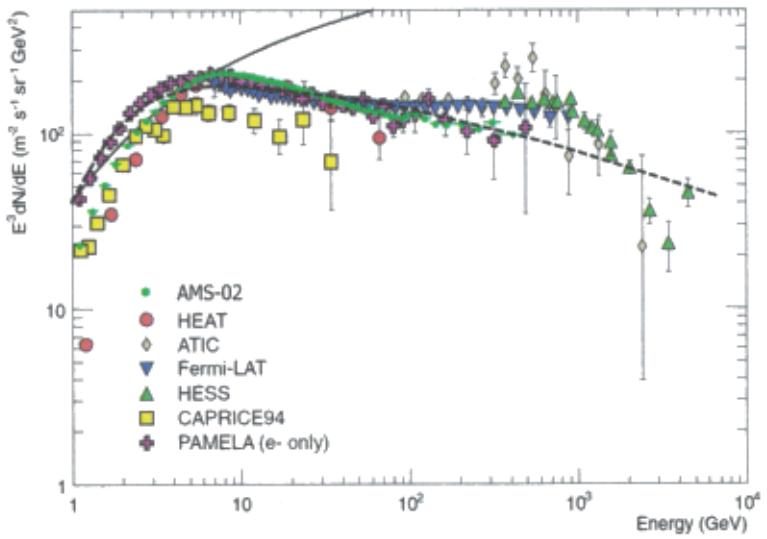

Figure 2.1: Cosmic-ray electron spectrum. Electron flux as measured by several previous experiments. The solid and dashed lines give the proton flux and the prediction for electrons based on cosmic-ray hadron interactions with interstellar material, respectively. *Figure credit:* Spurio (2015)

eventual deployment to space. Calorimetric instruments are composed of large, dense scintillators to contain the particle showers from cosmic rays for reconstruction of the kinetic energy with high accuracy. Due to the high weight of deep calorimeters, these detectors have until fairly recently been restricted to balloon flights. Payloads with a magnetic spectrometer use powerful electromagnets to determine both the sign and the magnitude of an incident particle's charge. Due to the power requirements, cost, and the size of the magnets, any accompanying calorimeter is necessarily small, limiting the energy range of these experiments. There have been numerous examples of magnetometers flown both in balloon-borne and on-orbit payloads (e.g. Picozza et al. (2007), Yamamoto et al. (2013)).

Figure 2.1 shows the electron flux times E^3 for several previous experiments (some still operational). PAMELA and AMS-02 are space-based magnetometers and show good agreement to hundreds of GeV. The results from the gamma-ray telescope Fermi-LAT, shown in green diamonds, show a somewhat flatter spectrum, which connects well to the

ground-based HESS spectrum shown by the green triangles (HESS data are only available at very high energies, as it is operates by imaging the light from particle showers in the atmosphere). The results from the balloon-borne ATIC calorimeter (Chang et al., 2008) exhibit an excess at roughly 500 GeV, a feature that was found to be consistent with the measurement from PPB-BETS (Yoshida et al., 2008). No other experiment duplicates the relatively sharp ATIC peak, but multiple experiments do show an excess over GALPROP[1] (shown as the dotted line in Figure 2.1) and other propagation calculations.

2.2 The CALET Calorimeter (CAL)

CALET was specifically designed to identify and contain high energy electrons up to TeV energies. Given the relatively low intensity of the electron flux compared to protons ($1{:}10^3$) at these energies, efficient discrimination between showers induced by electron (or photon) and hadronic primaries is critical. The payload (Figure 2.2) contains the primary calorimeter (CAL) (Torii et al., 2015), the CALET Gamma-ray Burst Monitor (CGBM) (Yamaoka et al., 2017) for detection of hard x-rays/soft gamma-rays arising from transient events, and an Advanced Stellar Compass (Jørgensen and Liebe, 1996) that provides high-accuracy pointing information through correlation of images and star catalogs. The instrument was launched and mounted to the Japanese Experiment Module Exposed Facility (JEM-EF) in August 2015 for a planned 5-year mission. Since the CAL is the instrument used for this work, a detailed description follows.

2.2.1 Instrumentation and Sub-detectors

As a dedicated electron telescope, CAL boasts a normal incidence depth of 30 radiation lengths (X_0) and comprises three primary sub-detectors: the CHarge Detector (CHD), the IMaging Calorimeter (IMC), and the Total AbSorption Calorimeter (TASC) (Figure 2.3).

The CHD is made up of two orthogonal layers of plastic scintillating paddles (32 mm $\times$ 450 mm $\times$ 10 mm each) read out by photomultiplier tubes (PMTs). It provides measurement of the absolute charge of primary particles passing through the top of the instrument.

[1] https://galprop.stanford.edu/

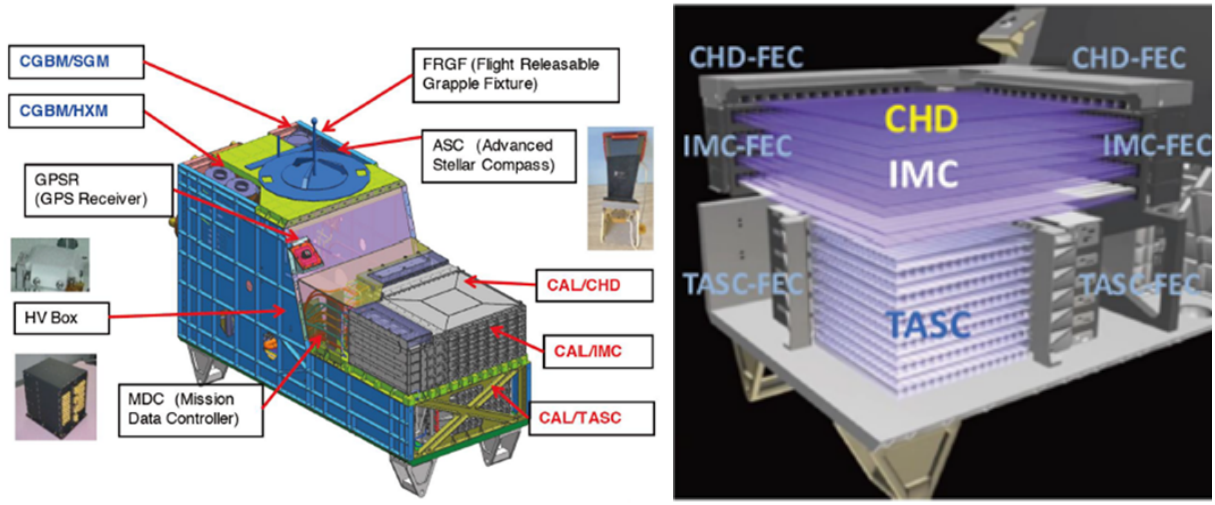

Figure 2.2: CALET schematics. The left panel shows the flight payload with individual subsystems and subdetectors labeled. The right panel shows the structure of the CAL subdetectors.

The IMC is a sampling calorimeter (sampling fraction ∼12% of energy deposited in active layers, see Figure 2.4) with pairs of crossed x-y layers (8 pairs × 2 layers × 448 fibers) of finely segmented plastic scintillating fiber (SciFi; 1 mm × 1 mm × 448 mm each) read out by multi-anode PMTs (MAPMTs), with 7 tungsten sheets interspersed between the layer pairs. The total thickness of the IMC is ∼3 radiation lengths (X_0), with the overwhelming majority of the material provided by the tungsten sheets (upper 5: 0.7 mm each, lower 2: 3.5 mm each). This stimulates the start and development of the particle shower, while the layers of SciFi provide high spatial resolution imaging of the cascade useful for particle identification and tracking.

The TASC is 12 crossed layers (6 pairs × 2 layers × 16 logs, each 19 mm × 326 mm × 20 mm) of lead tungstate ($PbWO_4$, or PWO) logs for a total thickness of 27 X_0. The top layer of PWO logs is read out by PMTs, while the lower layers are attached to photo-diode and avalanche photo-diode (PD/APD) readouts. The PMTs have two separate gain ranges and the PD/APDs have four, which enables the high dynamic range of the TASC. The TASC is deep and is entirely active detector material, providing high-accuracy energy reconstruction.

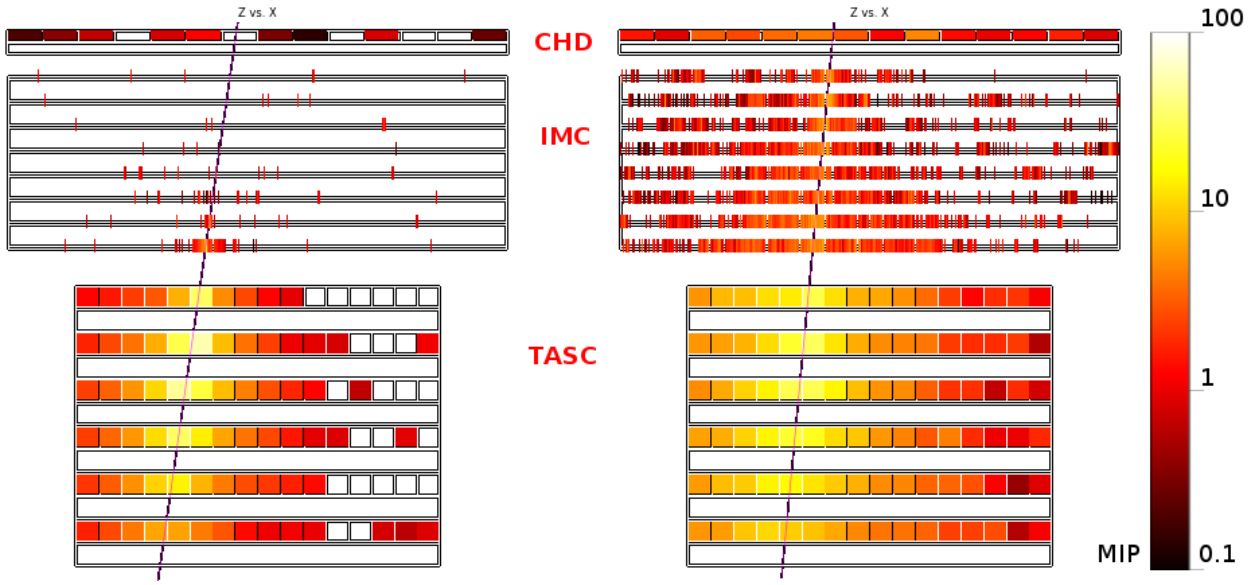

Figure 2.3: Flight data event views. (*left*) a gamma-ray candidate with TASC energy 450 GeV and (*right*) a hadronic primary with TASC energy 400 GeV. The roles of the CAL subdetectors are illustrated here, showing the measurement of charge in the CHD, the development of the shower and the tracking information from the IMC, and the majority of the energy deposit in the TASC. The difference in shower topologies for electromagnetic vs. hadronic primaries is illustrated by the greater lateral and longitudinal spreads for the hadronic event.

The depth of the calorimeter allows for nearly total containment of electromagnetic showers from primary electrons and photons with energies up to tens of TeV. Because of this efficient collection, the reconstruction of kinetic energies requires only a small adjustment to the energy deposit sum in the TASC for electrons with energy above ∼10 GeV. In contrast, the calorimeter depth only corresponds to 1.3 proton interaction lengths and a considerable fraction of the energy in showers from hadronic primaries is lost due to the escape of secondary hadrons (mainly pions). While the resultant energy resolution for hadronic primaries is worse than that for electrons and photons, the difference in shower topologies in the CAL gives a powerful rejection of the dominant proton flux.

In the discussions that follow, the CHD layers will be referred to as CHDx and CHDy and IMC/TASC layers will be labeled with a number 1-8 and an orientation axis (e.g. IMC 1x or TASC 5y).

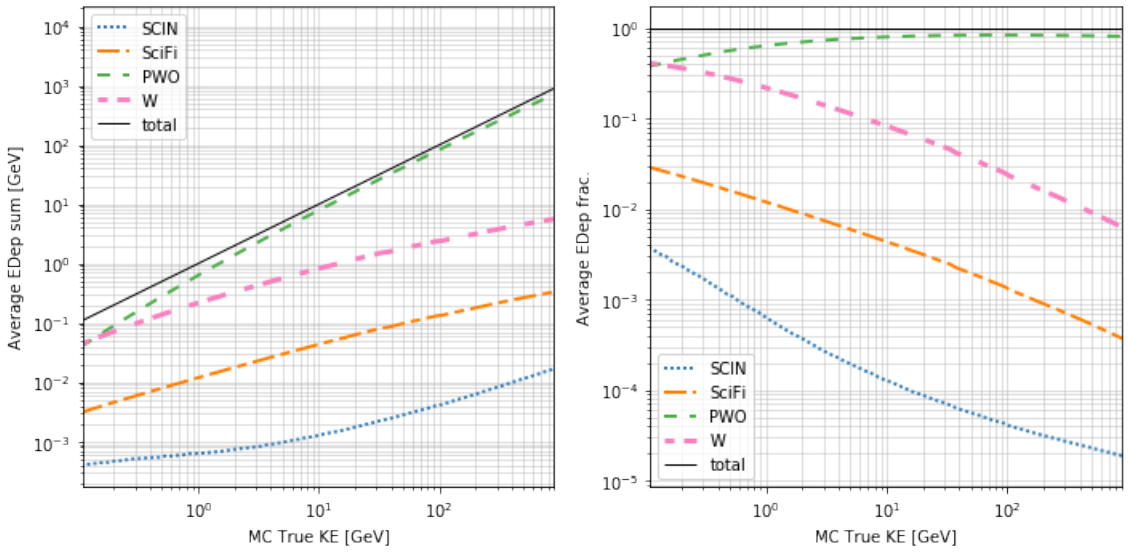

Figure 2.4: Energy deposit fractions. Fraction of in-geometry photon kinetic energy deposited in each detector material in the calorimeter as a function of energy. At 1 GeV, ∼65% of the total energy is deposited in the TASC, while a significant ∼20% is lost in the tungsten layers of the IMC.

2.2.2 Calibration

The accuracy of the conversion of digitized signals in the front-end electronics from individual detector components to real energy deposits is determined by the quality of the detector calibration. For the CAL, this consists of an initial, pre-flight calibration and frequent, time-dependent on-orbit updates to the calibration parameters. The discussion in this section summarizes work contained in Asaoka et al. (2018) and references therein.

The pre-flight calibrations consisted of laboratory experiments, measurement of cosmic ray muons, and a series of accelerator beam exposures that established the key performance of the subdetectors and the consistency with Monte Carlo simulations using the EPICS/Cosmos package (Kasahara et al., 1995). To investigate the linearity of the PD/APD response in all four gain ranges in the TASC readout, the PWO logs were exposed to UV laser pulses to excite the atomic electrons in the lattice responsible for the scintillation emission. The subsequent scintillation from the de-excitation was measured, characterizing the photo-detector response as a function of the energy of the input pulse.

Adjacent gain ranges in the PD/APD are set to have regions of overlapping utility. Cross-calibration of these gain ranges provides continuously non-saturated signals in the TASC elements over six orders of magnitude of energy deposits.

Additionally, a thermal model of the instrument was developed pre-flight such that the temperatures at any position in the instrument can be determined. The model is necessitated by the temperature-dependence of scintillator response and electronic noise in the readout system. Although temperature sensor readings are available to give direct measurements at various places on the calorimeter, it was impossible to incorporate sensors at multiple locations on each detector element. Instead, the temperature readings at the known positions were recorded in many trials along with independent measurements of the temperature elsewhere in the calorimeter. The thermal model was then tuned such that the measurements from the sensors could be interpolated to a complete temperature profile of the detectors with high accuracy.

With the scaling of the response established by the UV laser calibration, the absolute scale of energy deposited in each detector element can be set by the energy deposited by minimum-ionizing particles (MIPs). The charge of the incident particle is determined using the signal in the CHD, and the ionization signal from a penetrating (non-interacting) particle is measured in digitized ADC units for the components traversed by the MIP. In each channel, after scaling to account for path-length differences at different incidence angles, the distribution from mono-energetic penetrating particles is expected to follow a so-called Langau function, a convolution of the Landau function that describes the physical distribution of energy deposits from MIPs with a Gaussian function representing the electronic noise in the readout electronics.

The noise distribution is characterized for each channel by measuring the signal from events with zero energy deposit in each detector and is referred to as the pedestal distribution. Introducing the unique pedestal distribution (accounting for differences in the temperature) to events simulated with EPICS/Cosmos, a simulated MIP deposit distri-

bution can be calculated in units of energy. By comparison of these distributions with the measured distributions in the real instrument, an ADC-to-energy correspondence is derived. This is, by necessity, an iterative procedure due to the observed pedestal distributions being measured in digitized units. Fortunately, the process converges quickly, with a stable result emerging after one additional iteration.

Furthermore, it is necessary to account for the energy spectrum of the incident particles. The energy deposited by relativistic penetrating particles of a given species is only approximately constant, and particles below the minimum ionizing region are present in the data sample obtained on-orbit. This energy-dependence is complicated by the change in the local geomagnetic cutoff rigidity as the ISS moves along its orbital path. The ATMNC3 software (Honda et al., 2004) with input spectra from the AMS-01 instrument (Aguilar et al., 2002) was used to weight the input energies of the simulated dataset to guarantee the consistency of the simulated and measured distributions.

After an initial application of this MIP calibration method, higher-order effects are studied. Among these are position dependence of the energy deposit in the scintillator, which is driven by absorption in the material and reflection from boundary surfaces between the locus of the scintillation and the photo-detector. Additionally, the temperature-dependence of the scintillator response is measured using the thermal model described previously. These effects are characterized and corrected in the conversion to real energy units.

The systematic error and measurement accuracy was evaluated for the combined sum of deposited energy in all active detector elements as a function of the true energy deposit. For energy deposits greater than 10 GeV, this is consistently on the order of 2-3%. Below 10 GeV this consistently increases with decreasing energy to a level of approximately 10% at 1 GeV. Furthermore, the accuracy of kinetic energy determination for incident electrons as a function of particle energy is approximately 3% at 10 GeV, increasing with decreasing energy to 12-14% at 1 GeV. Due to the extreme similarity between electron- and photon-

induced electromagnetic showers, these results are also applicable to the reconstruction of incident photon kinetic energies. Realistic energy reconstruction of LE-γ candidates (with a wider geometrical acceptance) is described in Section 3.4.2.

2.2.3 On-orbit Operations

The scientific operation of CALET on-orbit commenced in October, 2015 and has remained approximately stable to present. The data collection is driven by a collection of hardware trigger conditions discussed in Asaoka et al. (2018) and described in some detail in this section.

The hardware trigger logic is divided into a single-particle trigger (Si), a low-energy shower trigger (LE), and a high-energy shower trigger (HE). These trigger conditions are based on combinations of logical discriminators (LD) on the CHD layers, the IMC layers, and the TASC 1x layer. Due to the arrangement of the fiber belts and MaPMTs in the IMC, the quantities from consecutive IMC x and IMC y layers are summed (i.e. IMC 1x + IMC 2x, IMC 1y + IMC 2y, IMC 3x + IMC 4x, and so forth). An additional LD threshold is applied to the CHD layers to allow for hardware-level identification of high-Z (heavy) nuclei by requiring a very large energy deposit in these layers. The three basic hardware triggers (Si, LE, HE), along with the heavy modifier, yield a total of 6 independent hardware triggers in the calorimeter (Si, LE, HE, Si-H, LE-H, HE-H).

To address the requirements of different scientific objectives and the challenges presented by the change of the instrument's environment with varying location, sets of LD thresholds are compiled into *run modes* that are enabled periodically. Always operational is the High-Energy shower mode (HE). The HE mode facilitates measurement of electrons and hadrons at energies above $\sim$10 GeV. Due to the high LD thresholds possible for such high-energy primary particles, the decrease of the geomagnetic cutoff at high declinations does not introduce a saturating low-energy-dominated event rate. This is contrasted to the Low-Energy Gamma Ray (LE-γ) run mode, which is less restrictive and is only operational at low declinations to avoid saturating rates at lower rigidity cutoff regions.

For the purposes of this thesis and the instrument characterization in Chapter 3, we assume the LE-γ run mode for gamma-ray observations. The trigger logic requires signals corresponding to energy deposits equivalent to 2.5 MIP in IMC 7x + IMC 8x, 2.5 MIP in IMC 7y + IMC 8y, and 7 MIP in TASC 1x. The resulting primary energy threshold for triggering events is reduced to below 1 GeV. Observations with this trigger are available when the instrument is at geomagnetic latitude $|\lambda_m| \leq 20^\circ$ and not in transit through the South Atlantic Anomaly (SAA).

2.3 Advanced Stellar Compass (ASC)

For high-accuracy pointing capabilities, CALET is equipped with an Advanced Stellar Compass (ASC) following the design used on the Oersted satellite (Jørgensen and Liebe, 1996). The ASC is an autonomous star tracker which correlates images from the on-board camera to reference star maps to determine a rotation quaternion from the instrument frame to celestial coordinates. The CALET ASC captures images twice per second and provides arcsecond resolution for the coordinate transformation. As will be shown in the following chapter, this is far better than accuracy of the direction determination for individual events, which is instead limited by the accuracy of primary trajectory reconstruction.

2.4 CALET Gamma-ray Burst Monitor (CGBM)

In addition to the CAL, CALET observes gamma-ray transients at lower energies using the CGBM (Yamaoka et al., 2017). CGBM (Figure 2.2) comprises a Hard X-ray Monitor (HXM), sensitive to photon energies 7 keV - 1 MeV, and a Soft Gamma-ray Monitor (SGM), sensitive to photon energies 100 keV - 20 MeV. Continuous observations are made with 8 energy channels at a period of 125 ms, and with 512 energy channels with a period of 4 s. When a significant excess over the expected background rate is measured, the CGBM trigger initiates data collection with 4096 energy bins and a period of 45 μs. Alerts are distributed for triggering events on the Gamma-ray Coordinates Network (GCN)[2]. Since it is not an imaging detector and has a field-of-view (FOV) of 120° for the HXM and 180° for

[2]https://gcn.gsfc.nasa.gov/calet.html

the SGM, CGBM does not provide directional information for events; source localization requires co-detection by other instruments.

Although analysis of the CGBM data is not in the scope of this thesis, CGBM triggers contribute to the duty cycle of the high-energy observations with the calorimeter. As described in Section 2.2.3, the LE-γ run mode is only active at low declinations. For other observation times, the energy threshold for the CAL is $\sim$10 GeV and significant detection of high-energy counterpart emission from transients such as GRBs is not expected. To increase the counterpart search capabilities of the CAL, the CGBM trigger prompts a change in the calorimeter observational mode to enable LE-γ observations for a limited time with a nominal delay on the order of milliseconds.

Chapter 3. Instrument Response Characterization

In this section, the performance of the CALET calorimeter for gamma-ray observations is characterized using simulated data. Validation using the first two years of flight data is described in Section 4. This work is central to the CAL gamma-ray analysis and is largely described in Cannady et al. (2018).

3.1 Simulated Dataset

To assess the sensitivity of the CAL to high-energy photon events, to tune the event selection to isolate the gamma-ray data sample, and to estimate the contamination of charged particle events in this sample, the EPICS/COSMOS software package is used to generate event data. A detailed CAD model of the calorimeter was developed in conjunction with the construction of the real physical payload and fine-tuned to describe the positions and sizes of the active detectors in addition to the various support structures.

The simulated events generated for this study were thrown isotropically from an upper hemisphere which completely contains the instrument and provides incidence angles up to 90°. The energies of the events in each sample were generated with a distribution following a power law of E^{-1}, which gives equal statistics in logarithmically spaced energy bins. Photons for the characterization of the instrument response were generated with primary energies ranging from 100 MeV - 1 TeV with statistics of 3.2×10^8 events per decade of energy. This dataset was generated using the High-Performance Computing (HPC) SuperMike-II cluster at LSU using a time allocation to CALET over the time period April 2017 - April 2018.

3.2 Tracking Algorithms

The reconstruction of incident particle trajectory using the IMC is key to the CALET data analysis of gamma rays and cosmic rays. Several algorithms have been developed within the CALET collaboration for different analysis targets, of which three are relevant to the analysis of photon events. These algorithms are described briefly in the following.

The Elemag Track (EM Track; Akaike et al. (2013)) algorithm is designed for the analysis of pure electromagnetic showering events and is used in the CALET cosmic-ray electron analysis (Adriani et al. (2017), Adriani et al. (2018a)). SciFi fibers are grouped in rolling sets of five, referred to as clusters. For each IMC layer and axis projection, the cluster with the maximum energy deposit is found and its center of energy is calculated. If no cluster significant above pedestal fluctuations is found in a given layer, that layer and all layers above it are not used in the fitting. To clarify, the algorithm uses consecutive layers starting from the bottom of the IMC until no usable signal is found. The remaining clusters are fitted with straight-line trajectories by chi-squared minimization in each axis projection. Together, these fully define the trajectory, which is then checked for consistency with the energy deposit distributions in the upper TASC.

EM Track is very efficient for the higher energy events for which it was designed, but exhibits a decreased efficiency for E below $\sim$10 GeV, where events first interacting via pair production in the upper layers of the IMC have a less well-defined signal in the lower layers. To recover some of these lower energy gamma-ray events, the CC Track (Cannady et al., 2018) algorithm was developed. For CC Track, the five fibers with the highest energy deposits are chosen from each axis projection for each of the lower three layers of the IMC. Clusters are again formed by including the neighboring fibers for each of these, and straight-line trajectories are fitted to each combination of these clusters (5 in IMC 6 $\times$ 5 in IMC 7 $\times$ 5 in IMC 8 = 125 combinations). These track candidates are then extrapolated to the higher layers, where additional clusters are added for each layer where a signal is found near the track. The extension continues for each candidate track until the reduced chi-squared statistic increases above 2. After this process concludes for all of the candidate tracks, the energy deposits along each are summed and the candidate with the largest sum is kept.

For both EM Track and CC Track, events are further filtered based on the number of layers that are used in the reconstruction. We define N_{p_x} and N_{p_y} to be the number

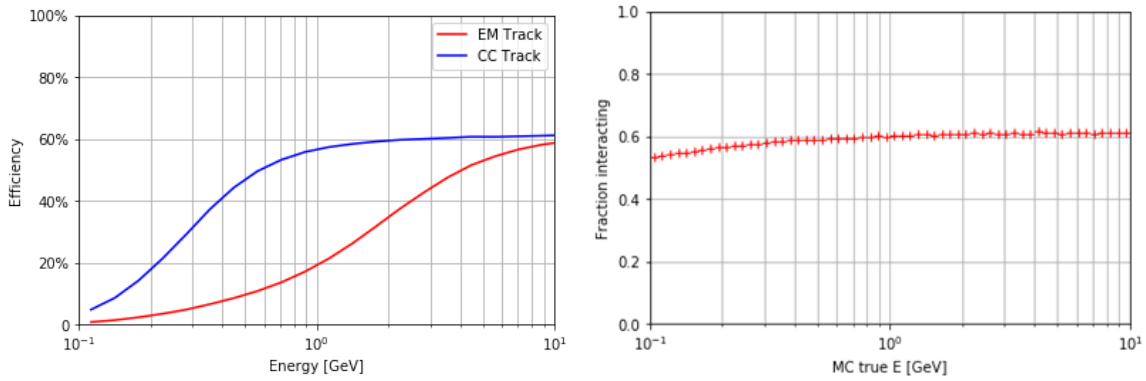

Figure 3.1: Efficiency for EM Track and CC Track. *Left:* The number of in-geometry simulated events reconstructed with the requirements on N_{p_x} and N_{p_y}. *Right:* The number of simulated events with first interaction in the fiducial volume restricted with the requirements on N_{p_x} and N_{p_y}.

of layers used for the x- and y-projections, respectively. Events with $|N_{p_x} - N_{p_y}| > 1$ are inconsistent in the assumed layer of first interaction, suggesting that the reconstruction has failed. Separately, N_{p_x} and N_{p_y} are required to satisfy $3 \leq N_p < 8$. Events where fewer than three layers used are typically due to side-entering charged particle events with secondary charged particle tracks. If all 8 layers are used, this suggests that the conversion layer is in or above the CHD. Checking simulated events confirms that primarily charged particle events are reconstructed with all 8 layers, and photon events satisfying this condition are typically poorly reconstructed.

Taking the region between IMC 1 and IMC 6 as a fiducial volume for initial pair production for photons, we can compare the fraction of simulated photon events in LE-γ geometry (see Section 3.3) that are satisfactorily tracked and the fraction that have their first interaction point in the fiducial volume. The left panel of Figure 3.1 demonstrates the ability of the CC Track to reconstruct a significant number of events in the energy range 1 GeV - 10 GeV that are missed by the EM Track. Comparing to the right panel, which shows that the efficiency for pair production in the fiducial volume is nearly constant at 60% above 1 GeV, we can derive efficiencies at 3 GeV of 67% and 92% for EM Track and CC Track, respectively. At 10 GeV, the difference has narrowed, with EM Track and CC

Track efficiencies of 93% and 97%, respectively. At energies higher than 10 GeV, the CC Track algorithm begins to show a bimodal distribution in angular reconstruction error, an effect which is still under investigation. This effect is discussed further in Section 3.4.3.

The third tracking algorithm relevant to the gamma-ray analysis is based on the Kalman Filter technique (KF Track; Maestro et al. (2017)). KF Track was developed specifically for the tracking of hadronic events, where the profile of the shower is not as uniform and the number of secondary tracks is high. Because of this tuning, straightforward application of the KF Track algorithm is not efficient for the reconstruction of photon events. However, we have found several auxiliary quantities calculated in the process of the fitting to have a high discriminating power between electromagnetic and hadronic events. The specific quantities used and their application in the event selection are discussed in some detail in the following section.

3.3 Gamma-ray Event Selection

Several stages of cuts are included in the isolation of photon event candidates: an offline trigger, tracking requirements, hadronic event rejection, and charge zero selection. In the following discussion, the motivation and details of these cuts are presented.

Offline trigger: The thresholds on the discriminators are in terms of ADC units, which, as discussed in Section 2.2.2, are variable with temperature and are also subject to small, long-term variations. To remove this variation, an offline trigger is used. The offline thresholds applied are significantly higher than those in place for the hardware trigger, and eliminate the time-dependent variation of the hardware discriminators. For the LE-γ run mode, the offline trigger used for both flight and simulated events has thresholds of 7 MIP for each IMC 7x + IMC 8x and IMC 7y + IMC 8y, and a threshold of 10 MIP for TASC 1x. The efficiency for passing this trigger is $> 90\%$ for E > 3 GeV, decreasing sharply for lower energies to $\sim$50% at 1 GeV and 0% at $\sim$500 MeV.

Tracking: In addition to the tracking requirements based on N_{p_x} and N_{p_y} discussed in the previous section, geometrical requirements are imposed to isolate a sample of events

which have charges measured in the CHD and a long enough path length in the TASC for a reliable energy reconstruction. For the electron and charged particle analysis at higher energies, the standard CALET geometrical conditions are referred to as A, B, C, and D. Geometry A (as defined in Table 3.1) is the most restrictive, requiring passage from the top to the bottom of the calorimeter with at least one full PWO log between the shower axis and the edge of the TASC to eliminate losses out the sides. Geometry B relaxes this edge requirement at the top and bottom planes of the TASC. Geometry C requires the middle of the IMC instead of the CHD, and geometry D requires a path length in the TASC equal to the normal incidence path length rather than passage through the TASC bottom.

The conditions used for the LE-γ analysis allow for a somewhat shorter path length in the TASC and demand passage through the CHD and the top of the TASC. A boundary of 2 cm (corresponding roughly to 1 PWO log width) is vetoed at the top of the TASC so that the shower is somewhat contained. The full definitions of geometries A, EB, ED, EB3, ED3, and E are then given in Table 3.1, with the most strict requirement at the top. The geometrical factors (Sullivan, 1971) were checked with a custom Monte Carlo simulation. Trajectories were generated isotropically on an upper hemisphere and the positions were calculated at the depths of the CALET detector planes. Equating the fluxes incident on the throw surface and the detector, the ratio of the acceptance condition geometrical factor to that of the throw surface is simply equal to the fraction of events that were thrown which pass the requirements. Over 10^{12} trajectories were thrown, and the statistical error in the calculation is on the order of $10^{-3} cm^2 sr$.

Shower shape/hadronic rejection: The flux of protons and Helium is several orders of magnitude higher than the galactic diffuse gamma-ray emission so that efficient rejection of hadronic events is critical. Several different cuts are in-place to exploit the differences in topologies for electron- or photon-induced and hadron-induced showers in the calorimeter.

A powerful technique first developed for the electron analysis (Adriani et al., 2017) uses the average shower spread in the TASC (R_E) and the fraction of the total energy deposited

Table 3.1: Requirements for the LE-γ geometrical conditions. The conditions marked with asterisks denote that the intersection point must be more than 2 cm from the edge of the layer boundary. Note that the geometrical conditions are defined exclusively, such that EB does not contain A, etc. The total geometrical factor for the LE-γ acceptance derived by Monte Carlo simulation is 1184 cm^2 sr.

Acceptance	Conditions			Geom. Fact. $[cm^2 sr]$
A	CHD top	TASC top*	TASC 6y bottom*	419.1
EB	CHD top	TASC top*	TASC 6y bottom	91.03
ED	CHD top	TASC top*	TASC path $>$ 24 cm	121.6
EB3	CHD top	TASC top*	TASC 3y bottom*	51.97
ED3	CHD top	TASC top*	TASC 3y bottom	127.9
E	CHD top	TASC top*		373.8

that is seen in the bottom TASC layer (F_E). In general, the width of the shower from hadronic events will be larger due to secondary pions created in the nuclear interactions of the primary. Furthermore, due to the TASC having a depth of 27 radiation lengths but only $\sim$1 proton interaction length, showers from protons or nuclei will be longer compared to showers from electrons with comparable kinetic energies due to the penetrating nature of these pions. That is, both R_E and F_E are expected to be larger for hadronic primaries than electrons or photons (c.f. right and left panels of Figure 2.3). The discriminating parameter is then defined as $K = \log_{10}(F_E) + R_E/2$ cm. The threshold for the K cut is placed based on simulated photon events as a function of energy and reconstructed acceptance condition, and is tuned to give a 95% efficiency for photons.

Also exploiting the increased average shower width for hadronic primaries is a cut on the concentration of the energy deposited in the lower IMC layers close to the reconstructed track position. It is required for gamma-ray candidates that at least 40% of the energy deposited in the layer is within 1 tungsten Molière radius ($\pm$9 fibers) of the track hit position for both IMC 8x and IMC 8y.

An additional challenge for the low-energy gamma-ray observations with the CAL is the contamination from low-energy protons which enter the side of the instrument near the top of the TASC. These events can interact and produce a secondary track which

travels upward a few layers into the IMC and then stops. For the tracking and selection algorithms, these events mimic photons since they provide a clear track in the lower IMC, and no ionization signal above. To remove these events, a filter is placed on the ratio of the energy deposited in the bottom layer of the IMC and the energy deposited in the highest layer used in the tracking - the nominal pair conversion layer. For real photon events, the fraction of energy in the bottom of the IMC should be large due to the development of the electromagnetic shower. For the upward-moving, sub-minimum ionizing charged particles, however, the energy loss rate via ionization increases as the particle slows down, resulting in a higher energy loss higher in the detector. The threshold on the ratio is therefore set at 1, removing events which deposit more energy in their nominal conversion layer than in the bottom of the IMC.

Finally, the KF Track parameters (Section 3.2) are used as an additional discriminator. Since the KF Track algorithm exhibits a high efficiency for proton events and a quite low efficiency for photon events, we reject events that it reconstructs well, but that disagree with the EM Track or CC Track result. Specifically, if KF Track algorithm results in a reduced chi-squared statistic of less than 3.5 for both the x- and y-projection and finds a trajectory with an angular difference of more than 6° with respect to the EM Track or CC Track result, the event is removed. Additionally, if more than 400 clusters in the IMC are found for tracking by KF Track, the event is removed.

Charge zero: Finally, we use the signals in the CHD and the top of the IMC to remove events that have measured charge $Z > 0$. Three filters were developed from the simulated data to remove events that consistently measure charge 1 or more in both the x- and y-projections. The quantities tested are the signals in the CHD strips traversed by the reconstructed trajectory, the maximum of the CHD strips, and the signals in the IMC 1x and IMC 1y clusters along the reconstructed trajectory. Figure 3.2 shows the CHD Y signal vs. CHD X for flight data events which passed the tracking and hadron removal cuts, and the result of cutting on the CHD X and CHD Y strips along the trajectory. The

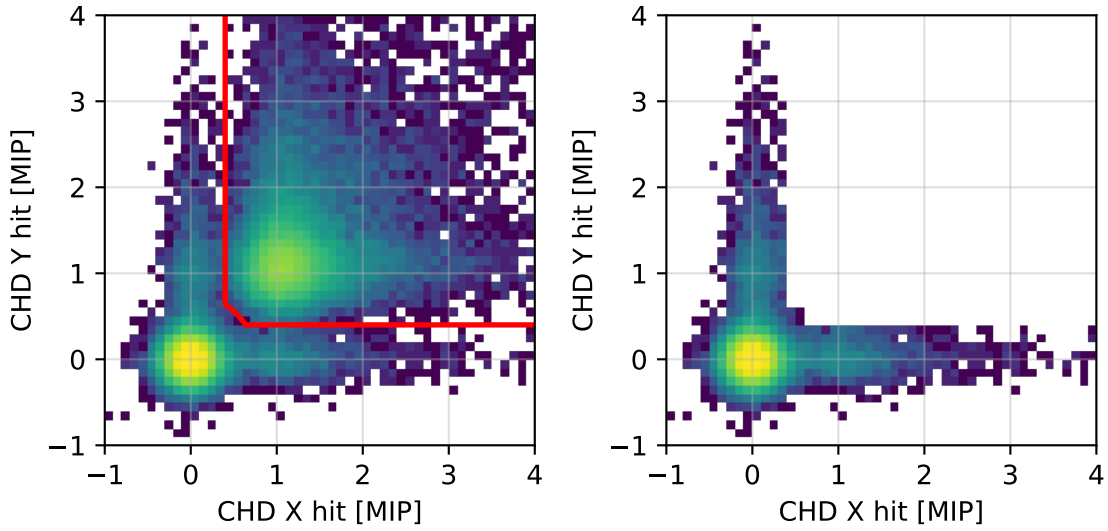

Figure 3.2: Flight data distribution of CHD Y hit vs. CHD X hit events. The red line in the left panel indicates the cut, where events in the upper-right region are removed. The right panel shows the distribution after the cut.

Table 3.2: Requirements for events to pass the charge zero filter. All numerical quantities are in MIP-equivalent energy deposits.

Quantity	Requirement
CHD hit	$X < 0.4$ or $Y < 0.4$ or $\sqrt{X^2 + Y^2} < 0.75$
CHD max	$X < 1.0$ or $Y < 1.0$ or $\sqrt{X^2 + Y^2} < 2.0$
IMC 1 hit	$X < 0.1$ or $Y < 0.1$

distribution for the CHD max is similar in character, and the cut placed on CHD Y vs. CHD X is similar in shape. For the IMC 1x and IMC 1y hit clusters, the concentration at zero is more pronounced due to the zero suppression of the IMC fibers in readout. As a result, the cut placed on the IMC 1y vs. IMC 1x distribution is simpler. All three filters are detailed in Table 3.2.

After the application of this charge zero filter, simulated events demonstrate that the effect on gamma-ray events is minimal while the charged particle contamination is greatly reduced. For reconstructed energies 1 GeV - 10 GeV, the fraction of contaminating electrons

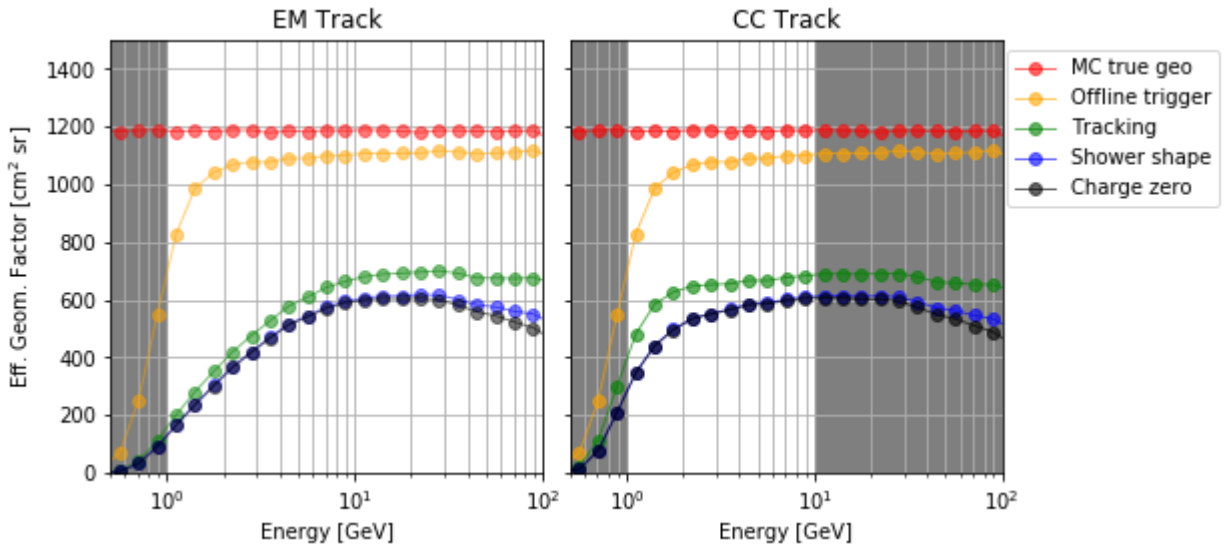

Figure 3.3: Effective geometrical factor for photon events. Curves show effect of each category of cuts. The shaded regions indicate energies not considered in the current analysis.

and protons drops to 1.65% and 16.0% of the number surviving after all previous selections, respectively, while the filter has a 99.6% efficiency for photons. At higher energies, the number of accepted events (charged particles and photons) drops due to the increasing contamination of the CHD and IMC signals from backscattered secondary particles.

The gamma-ray selection efficiency as a function of energy is given in Figure 3.3 as an effective geometrical factor. This neglects any angular dependence of the efficiency, which is discussed in detail in Section 3.4.1. The largest decrease in the efficiency is seen from the tracking requirements. The convergence of the tracking efficiencies to the pair production efficiency in Figure 3.1 demonstrates that for energies ∼10 GeV, the efficiency for reconstructing events converting in the required volume is over 90%. The ability to increase the number of successfully tracked events is thus limited by the number of photons which actually interact in the region of the IMC where reconstruction is possible. After application of the tracking requirements, the effect of the hadron rejection and charge zero

selection on the remaining photon events is rather small, indicating a high efficiency for these selections.

One final selection applied before the calculation of the instrument response functions is a mask on ISS structures. Due to the wide field-of-view (FOV; out to $\sim 60^{\circ}$) allowed by the LE-γ acceptance conditions, several fixed structures from the ISS become visible. These represent a significant background source because of secondary photons produced by cosmic-ray interactions with the material. A mask is used to remove those parts of the FOV from the analysis given the extremely high event rate as compared to real astrophysical gamma rays. The effect of this mask can be seen in Figure 3.4. In Chapter 4, the observed background due to moving structures associated with the ISS and its maintenance will be discussed.

3.4 Response Functions

3.4.1 Effective Area

With the selection cuts finalized, the effective area of the instrument can be characterized. For the discussions that follow, we use the HEALPix scheme (Górski et al., 2005) to divide the sky into pixels equal in solid angle. Considering bins in energy (subscript i) and position in the FOV (subscript j), an observation over a range of energy and direction is converted to a differential flux by the relation

$$\left(\frac{d^2\Phi}{dEd\Omega}\right)_{ij} = \frac{N_{ij}}{\Delta E_i \Delta\Omega_j (S_{eff})_{ij} \Delta t} \tag{3.1}$$

where ΔE_i is the width of energy bin i, $\Delta\Omega_j$ is the solid angle subtended by FOV pixel j, N_{ij} is the number of events seen in this bin, $(S_{eff})_{ij}$ is the effective area in this bin, and Δt is an observation time. If we consider the throw surface as a perfect detector and equate the thrown and detected fluxes, we find that the bin sizes and arbitrary observation time cancel, leaving

$$(S_{eff})_{ij} = \frac{N_{ij}^{obs}}{N_{ij}^{thr}} A_j \tag{3.2}$$

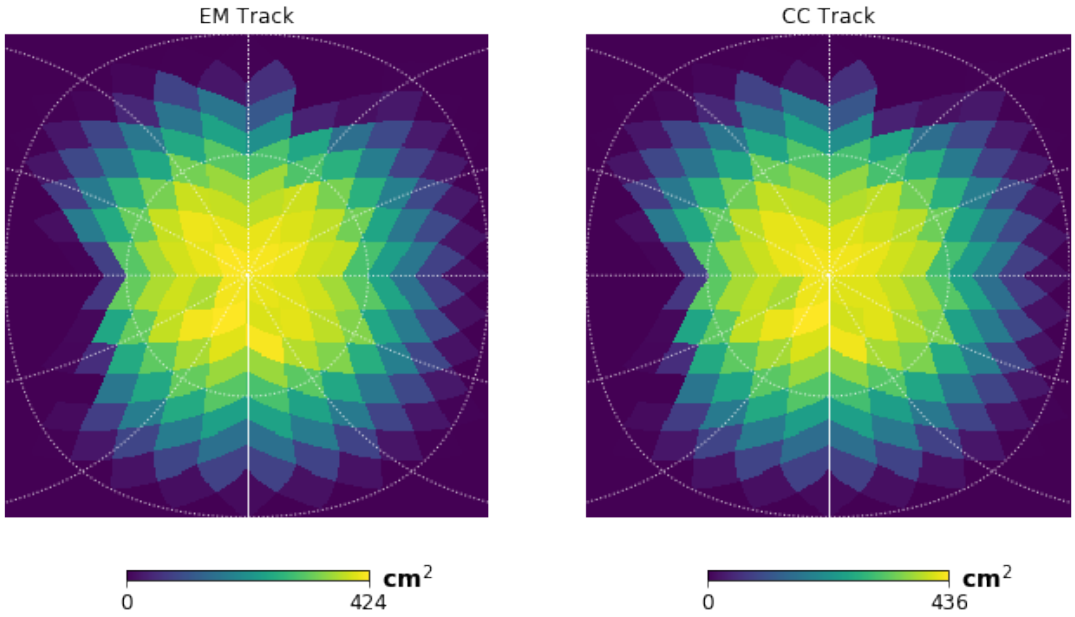

Figure 3.4: Effective area variation in the FOV at 10 GeV. The asymmetry in the response is due to the ISS structure mask. White lines indicate 30° divisions in zenith and azimuthal angle.

where A_j is the projected area of the throw surface onto pixel j. In the case of our simulations, the throw surface is spherical, so this reduces simply to the area. Since HEALPix pixels are equally sized, this can be calculated as the surface area of the throw sphere divided by the number of pixels. Figure 3.5 shows the decrease in the effective area with increasing zenith angle. A peak value of ∼400 cm^2 is achieved at roughly 2 GeV and 7 GeV for CC Track and EM Track, respectively, and is maintained up to 100 GeV by the EM Track analysis.

3.4.2 Energy Resolution

The design of the CAL is such that the majority of the kinetic energy of the primary will be deposited in the deep calorimeter of the TASC. However, as seen in Figure 2.4, the fraction of energy deposited in the inactive tungsten layers of the IMC is significant, especially for events with lower kinetic energy. A reconstruction method taking into account this invisible energy loss is thus necessary.

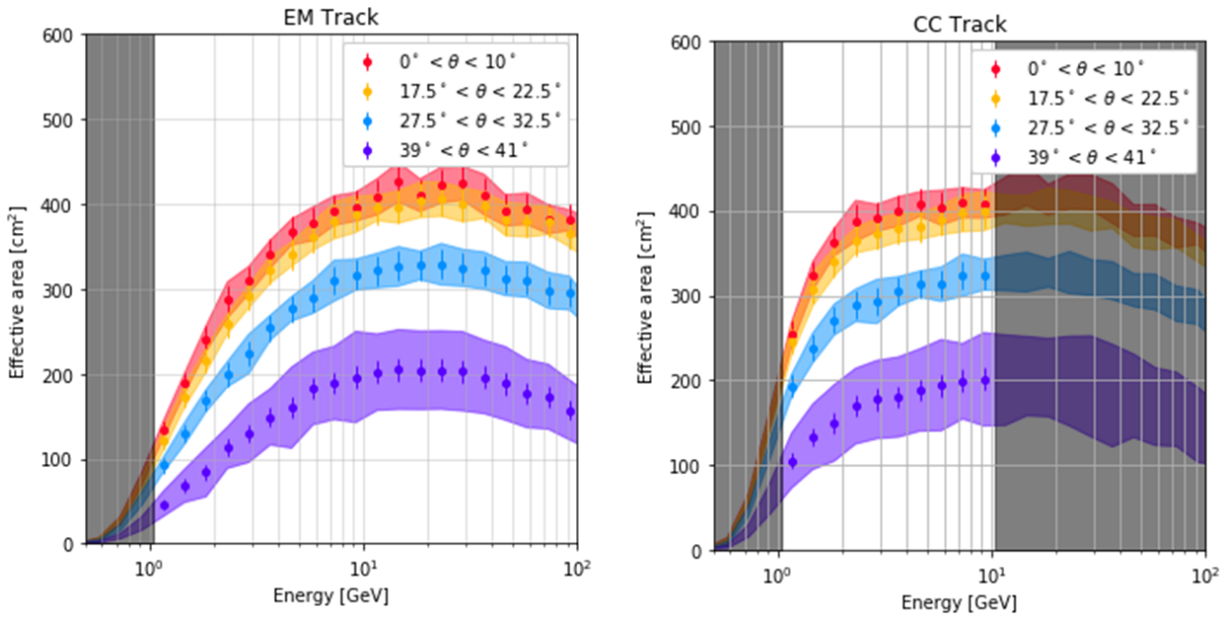

Figure 3.5: Effective area in zenith-angle bins. The error bars are statistical, while the shaded region includes the standard deviation of the bins in the zenith-angle bin. The large shaded region at high zenith angle results from the masking of some regions due to ISS structure obstructions. Gray shaded regions indicate the limits of applicability for this analysis; events below 1 GeV are not analyzed. For CC Track, events above 10 GeV are also not analyzed.

Again pointing to Figure 2.4, the energy lost in the tungsten, on average, corresponds closely to the energy deposited in the fibers of the IMC. Using the simulated dataset, weights can be assigned to each of the active IMC layers to scale the energy deposited therein to account for the effect of the tungsten. To achieve this, the simulated candidate dataset was binned in energy and divided into subsets for each of the acceptance conditions. The added complexity from considering the energy reconstruction for each geometric acceptance separately is warranted by the increased confidence in the result for the more restrictive conditions.

Figures 3.6 and 3.7 show the distributions of the reconstructed energy as a function of the Monte Carlo energy for EM Track and CC Track, respectively, as a heat map. Each panel shows the results for an individual geometrical acceptance condition (e.g. A, EB, etc.). The distributions are normalized in true energy, such that the integration along

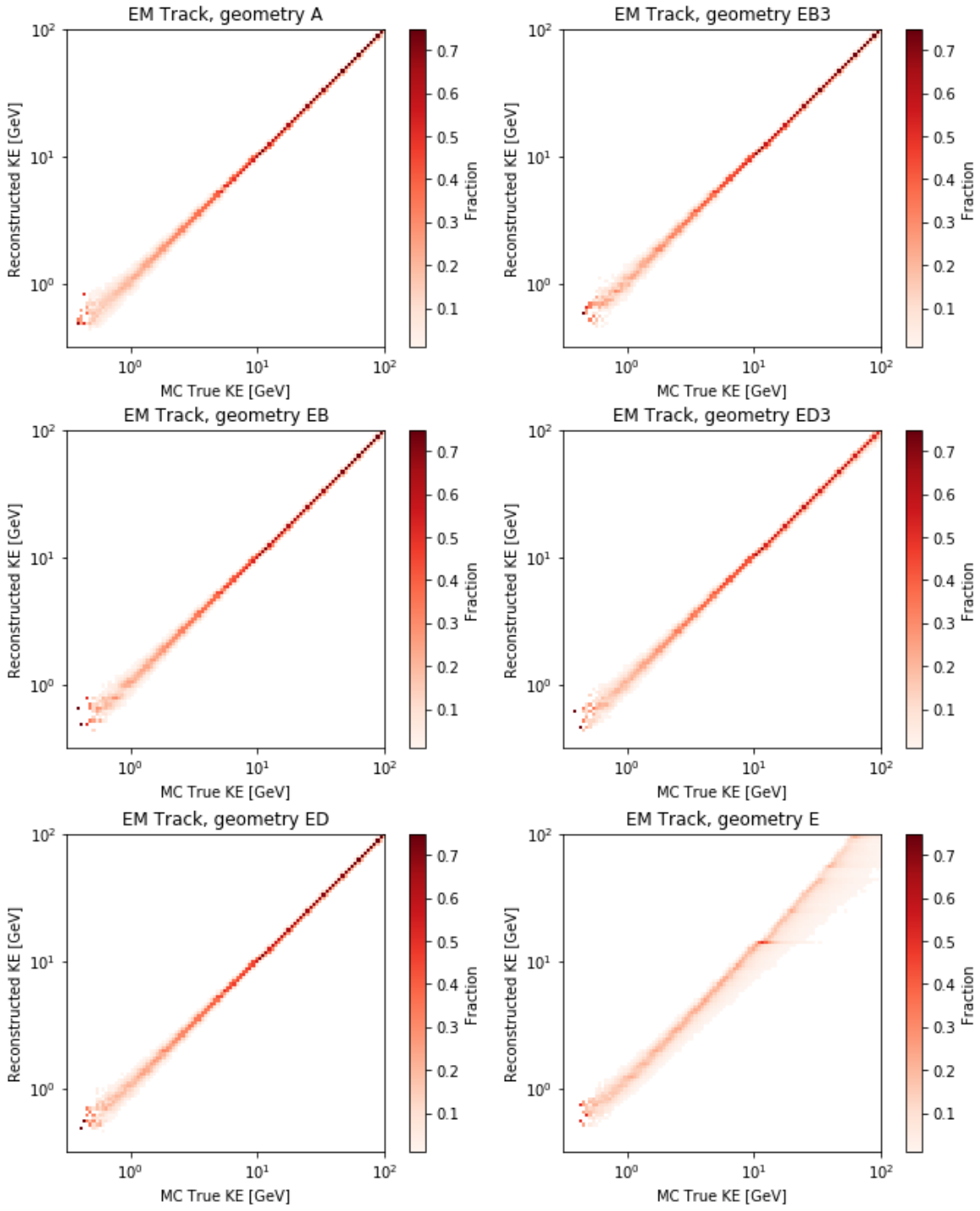

Figure 3.6: EM Track energy reconstruction. Reconstructed energy as a function of Monte Carlo true energy for EM Track reconstructed events.

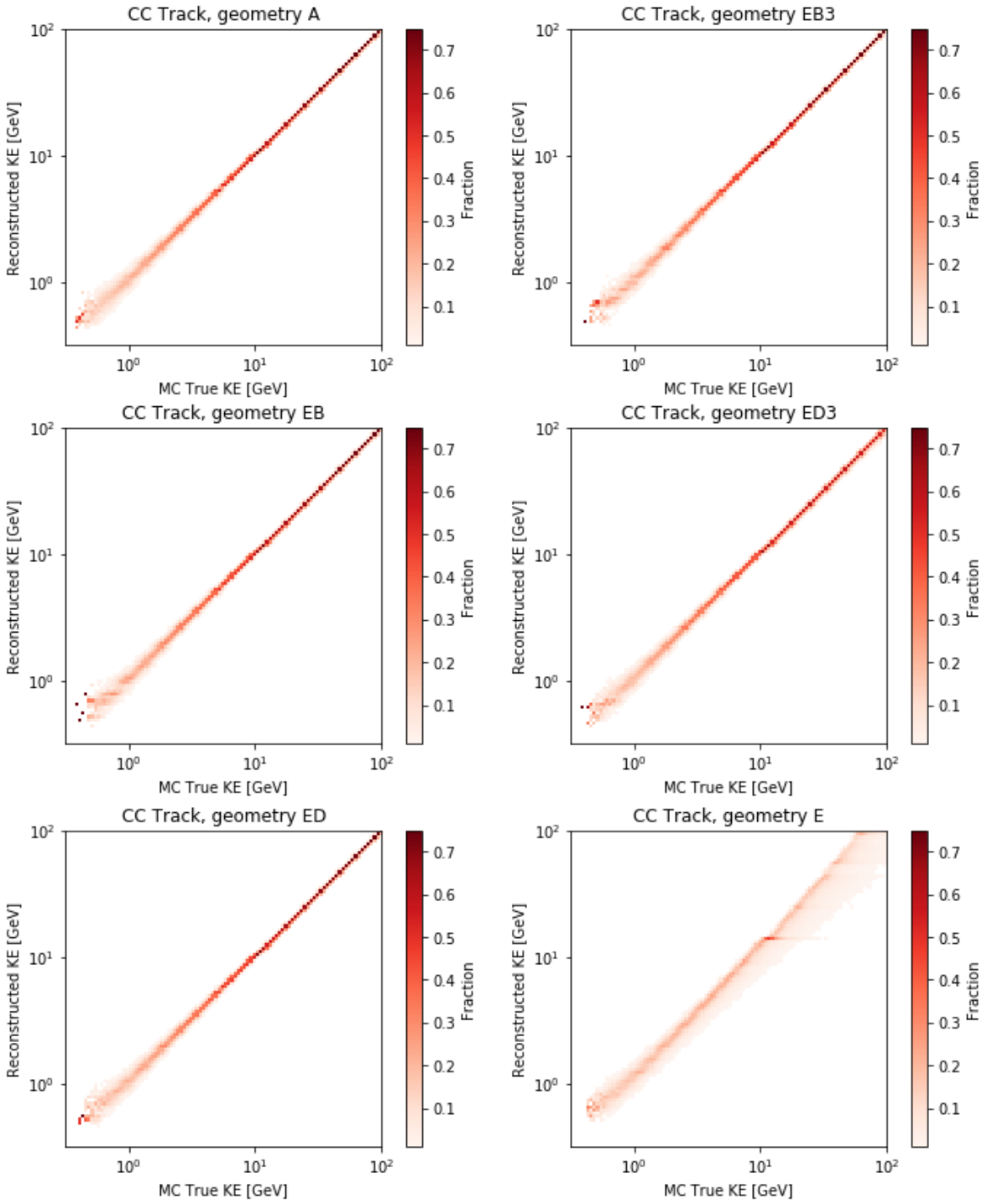

Figure 3.7: CC Track energy reconstruction. Reconstructed energy as a function of Monte Carlo true energy for CC Track reconstructed events.

each column yields 1. The behavior for EM Track and CC Track is notably similar. The reconstruction is reliable with fair accuracy for both algorithms for the more restrictive geometries, with error on the order of a few percent above 10 GeV and on the order of 10% below 10 GeV. The exceptional case is geometry E, where many trajectories have a rather short length in the TASC and the leakage of energy out of the instrument increases the uncertainty greatly, increasing the resolution to nearly 100% for low energies and even higher for $E > 30$ GeV.

3.4.3 Angular Resolution

The angular resolution of the instrument describes the accuracy with which the arrival direction of a photon candidate is reconstructed by the tracking algorithms. It is here characterized as a function of energy and the number of layers used in the tracking. The methodology used roughly follows the treatment of the Fermi-LAT angular resolution as presented in Ackermann et al. (2012). Recalling the definitions of N_{p_x} and N_{p_y} from Section 3.2, we define here a single corresponding variable for the classification of tracks, $N_p = \min(N_{p_x}, N_{p_y})$. In general, tracks with a smaller number of layers used in the fitting will have poorer accuracy, while those leveraging more of the IMC have higher accuracy.

The angular separation between the true and reconstructed tracks can be calculated simply using a dot product. With $\hat{u}$ and $\hat{v}$ representing unit vectors pointing along the reconstructed and Monte Carlo true directions, respectively, we denote the angular error

$$\delta\nu = \arccos(\hat{u} \cdot \hat{v}) \tag{3.3}$$

Calculating this quantity for each of our simulated candidate events, we consider the bins in energy and N_p separately. The distribution of angular errors is determined for each of the bins and the 68% containment radii of these distributions are calculated. This is the quantity henceforth referred to as the angular resolution (C_{68}): the angular error within which 68% of events are reconstructed.

As a function of energy, the value of C_{68} for each bin in N_p is well-fitted by the empirical function

$$S_p(E; N_p) = \sqrt{(c_0 E^{-\beta})^2 + c_1^2} \times (1 + E^{\delta}) \tag{3.4}$$

which is referred to as the scaling function or simply as S_p in the following discussion. Here the free parameters for the fitting are c_0, c_1, β, and δ. The power-law indices on the energy, β and δ, give the steepness of the decreasing trend at low energies and the increasing trend at high energies, respectively. The amplitudes c_0 and c_1 are related to the amplitude of the function at $E = 1$ GeV and the absolute floor of the function, respectively. The angular resolution, C_{68}, is calculated using simulated events and a chi-squared fitting of the functions S_p is performed. The results are shown in Figure 3.8. For LE-γ analysis the energies being considered are in the range 1 GeV $\leq E \leq$ 100 GeV. The fits in this region represent the angular resolution quite well, although the fitting included energies slightly beyond this range to ensure good fits at the edges of the range.

As seen from the data points in the figure, the angular resolution of the CAL is better than 2° for $E > 1$ GeV, and above 10 GeV, this further improves to better than $\sim 0.5°$.

3.4.4 Point-spread Function

For the study of point-like sources of gamma rays, it is necessary to determine how the spatial distribution of events associated with a source will be affected by the angular resolution as characterized in the previous section through the derivation of a probability density known as a point-spread function (PSF). To this end, this section is focused on determining the point-spread function of the CAL, and again roughly follows the treatment for Fermi-LAT described in Ackermann et al. (2012).

Starting from the simulated sample of gamma-ray candidates, we use the fits for the scaling functions S_p shown in Figure 3.8 to define the scaled angular error for an event i as a function of its reconstructed energy and N_p,

$$x_i = \frac{\delta\nu_i}{S_p(E_i, N_{p_i})} \tag{3.5}$$

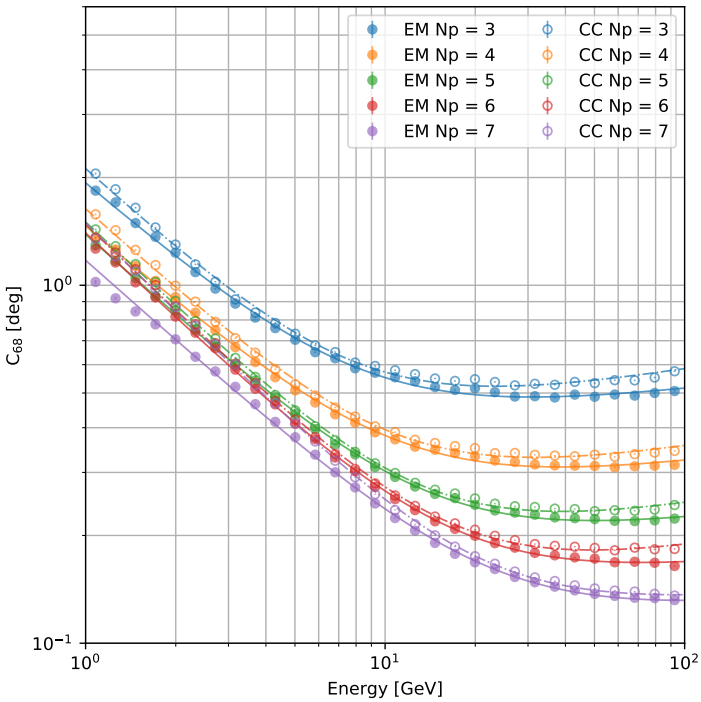

Figure 3.8: Angular resolution as a function of energy. Shown independently for EM Track and CC Track and for each possible value of N_p. The solid and dashed lines show the fits to the scaling function for the EM Track and CC Track distributions, respectively.

The empirical probability density functions for the tracking algorithms are then obtained using the cumulative dataset of scaled angular errors. For EM Track, this covers the energy range from 1 GeV to 100 GeV, while for the CC Track events, it is limited to the 10 GeV cap imposed by the validity for the algorithm. Each event is weighted by its corresponding $1/\sin \delta\nu$ to account for the differential solid angle corresponding to the real angular separation. The content of each bin is scaled by its width so that it will be properly normalized under integration.

A first check of the distribution was performed using unscaled angular errors in various energy bins. A fit was attempted with a Gaussian function, which gave a reasonable approximation, but examination of the residuals showed the existence of tail contribution as with a t-distribution. In the more rigorous treatment described above and presented in Cannady et al. (2018), a King function (a parameterization of a t-distribution initially

presented in King (1962) and adapted in Ackermann et al. (2012)) is used. The functional form is

$$K(\alpha, \sigma, \gamma) = \frac{1}{2\pi\sigma^2}\left(1 - \frac{1}{\gamma}\right)\left[1 + \frac{1}{2\gamma}\frac{\alpha^2}{\sigma^2}\right]^{-\gamma} \tag{3.6}$$

where α is the independent variable and σ and γ are parameters. The function automatically satisfies the normalization condition

$$\int_0^\infty K(\alpha)\ 2\pi\ \sin(\alpha) d\alpha = 1 \tag{3.7}$$

For angular quantities such as the angular error in track reconstruction, the upper bound of integration should be π. The normalization is still valid if the contribution to the integral for $\alpha > \pi$ is small. Under the small angle approximation, $\sin\ \alpha \approx \alpha$, the normalization condition then simplifies to

$$\int_0^\pi K(\alpha)\ 2\pi\alpha d\alpha = 1 \tag{3.8}$$

This simplified condition can be used for the normalization of the empirical distribution assuming that the contribution to the integrated PSF due to angles where the small angle approximation fails is small. We note that this normalization is still valid for the scaled angular error x despite it being dimensionless if the approximations are valid separately in each bin in energy and N_p used in the construction of the distribution. In more straightforward language, it is easy to see that the normalization condition is unchanged under the transformation $\delta\nu \to x$ when the width of the distribution, σ, is also scaled to account for the change in units ($\sigma_{\delta\nu} = S_p(E, N_p)\sigma_x$). We find that the error implicit in the small angle approximation for our distribution is no more than $\sim$1 % for angular error $x \leq 10$.

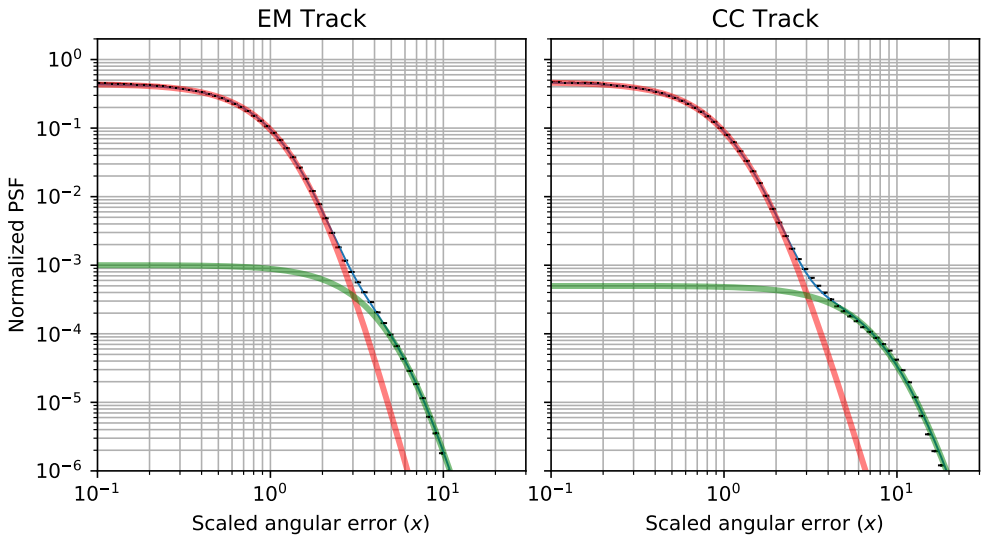

Figure 3.9: The simulated PSF. Distributions for the EM Track (left panel) and CC Track (right panel) and the corresponding best fit function. The solid red and green curves correspond to the core and tail functions, respectively, and the sum is given by the thin blue curve.

The empirical PSF of the CAL is, in fact, best fitted by a pair of these King functions representing a core and a tail contribution.

$$\begin{aligned} P(x) &= fK_{core} + (1-f)K_{tail} \\ &= fK(x,\gamma_1,\sigma_1) + (1-f)K(x,\gamma_2,\sigma_2) \end{aligned} \tag{3.9}$$

It is clear that $0 \leq f \leq 1$ preserves the normalization implicit in the King functions (Equation 3.8). The fits shown in Figure 3.9 are obtained by a chi-squared minimization and correspond to 68%, 95%, and 99% containment radii of $x = 1$ (1), $x = 1.9$ (2.0), and $x = 2.6$ (3.5) respectively for the EM Track (CC Track) distribution. The validity of limiting the upper bound for integration was tested independently in each bin of energy and N_p and the resulting error in the normalization is found to be on the order of 10^{-4}.

This result is obtained using only simulated data. In Section 4.3, the consistency of the result with flight data observations will be discussed.

3.4.5 Incorporation of Zenith-Angle Dependence

The characterization of the angular resolution and consequentially the PSF in terms of the energy and N_p neglects any dependence of the behavior on the incidence angle of the photon event. In this section the results are expanded beyond those contained in Cannady et al. (2018) to properly account for this dependence.

The methodology used closely follows that in the previous section with the additional division of the dataset into bins equally spaced in cos θ, where θ will be used to denote the incidence angle of the event in the CAL coordinate frame. Figure 3.10 shows the angular resolution results in three zenith angle bins. The longer pathlength in the IMC corresponding to the larger incidence angles improves the angular resolution at high energies ($> 30GeV$). This improvement is nearly by a factor of 2 at $\theta \sim 45°$.

The goal of this study was to factor out the θ-dependence of the angular resolution with functions analogous to the S_p used above when constructing the PSF. To this end, the functional form of the scaling functions was modified to clearly separate the effect of each parameter. For a given bin in θ, the scaling function will follow the form

$$S_p(E, N_p) = \sqrt{c_0^2 + c_1^2 E^{-2\beta} + c_2^2 E^{2\alpha}} \tag{3.10}$$

In this form, the slope of the falling power law is given by β and the slope of the rising power law is given by α. The energy-independent base of the function corresponds to c_0, and the amplitudes of the falling and rising power laws are coupled to c_1 and c_2, respectively. An example of the function is given in Figure 3.11.

Initially, fits were performed separately in coarse bins of θ. Several trials of holding some parameters constant and checking the dependence on the zenith angle for the others suggested two main effects: quadratic dependences for the amplitudes of the falling power law and the base function on cos θ. Taking this into account in designing a function to be

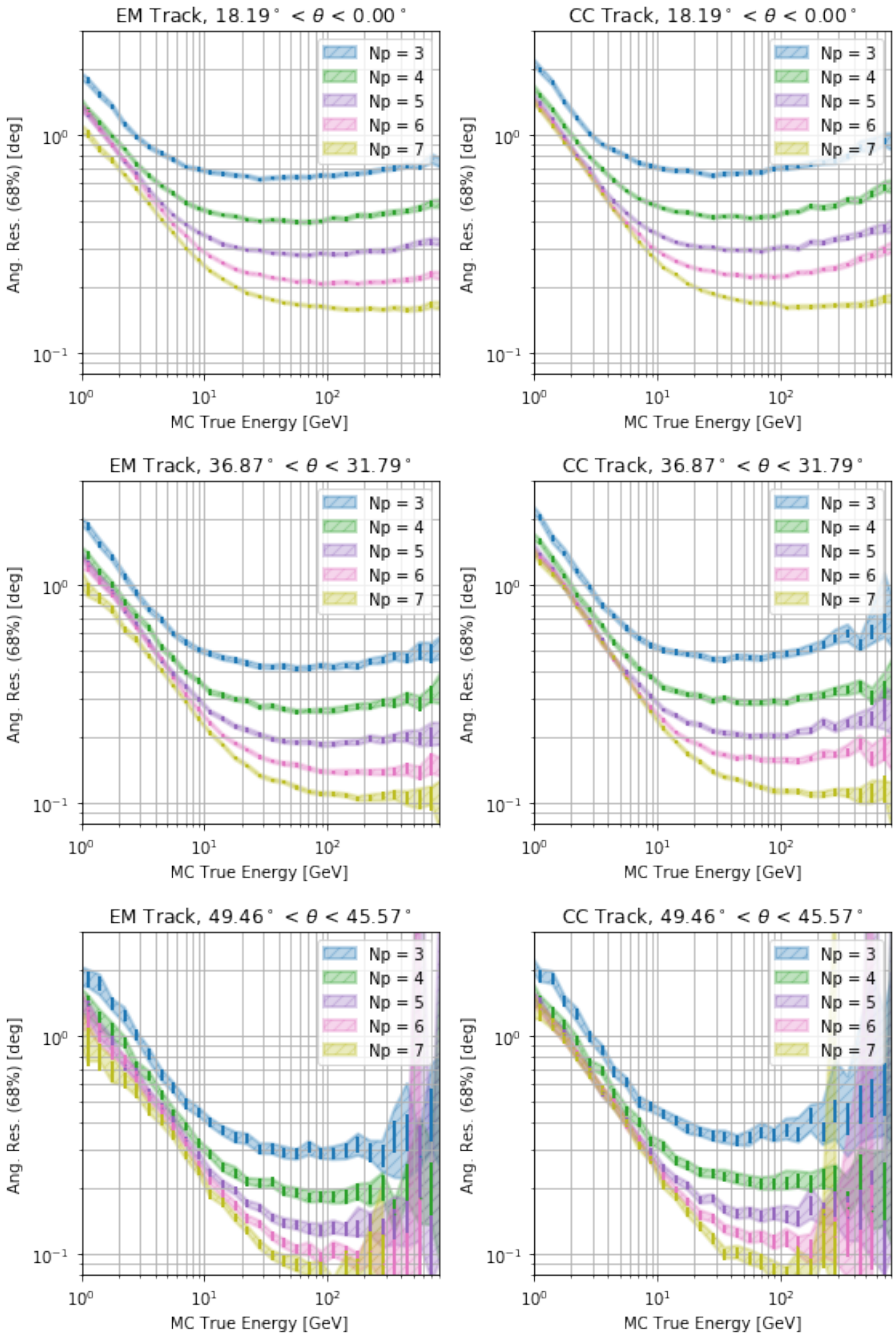

Figure 3.10: Zenith-angle dependence of the angular resolution. Angular resolution in three zenith-angle bins for EM Track (left column) and CC Track (right column) events. The shaded regions correspond to the 95% Poisson confidence intervals based on the number of events in each bin, whereas the solid error bars correspond to statistical errors.

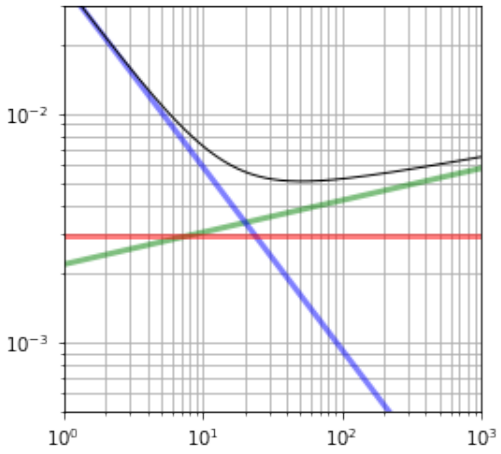

Figure 3.11: A slice of the expanded scaling functional form for the angular resolution. The blue and green curves represent the contributions from the falling and rising power laws, respectively. The red function is the energy-independent base and controls the smoothness of the transition between the regions where each power law contribution dominates. The net function is given by the black curve.

fit in E and θ simultaneously, the form chosen for S_p becomes

$$S_p(E, N_p, \theta) = \sqrt{(c_{00} + c_{01}\ \cos^2\theta)^2 + (c_{10} + c_{11}\ \cos^2\theta)^2 E^{-2\beta} + c_2^2 E^{2\alpha}} \tag{3.11}$$

A chi-squared fitting of this functional form converges well for each tracking algorithm and value of N_p (Figures 3.12 and 3.13 show the fit visually). An examination of the covariance matrices reveals that the $\cos^2\theta$ dependence does not perfectly describe the falling power law, especially for EM Track at higher values of N_p (fractional error $\sim$20%).

Since the θ-dependence is accounted for in this prescription of S_p, there is no need for further modification of the PSF function or the method for constructing the empirical distribution. The resulting distributions and the corresponding fitted functions are shown in Figure 3.14.

The results for the EM Track algorithm are similar in character to those without the zenith angle dependence (c.f. Figure 3.9). One change of note in the result is the narrowing of the tail contribution for the CC Track distribution. This reveals itself in the fitting

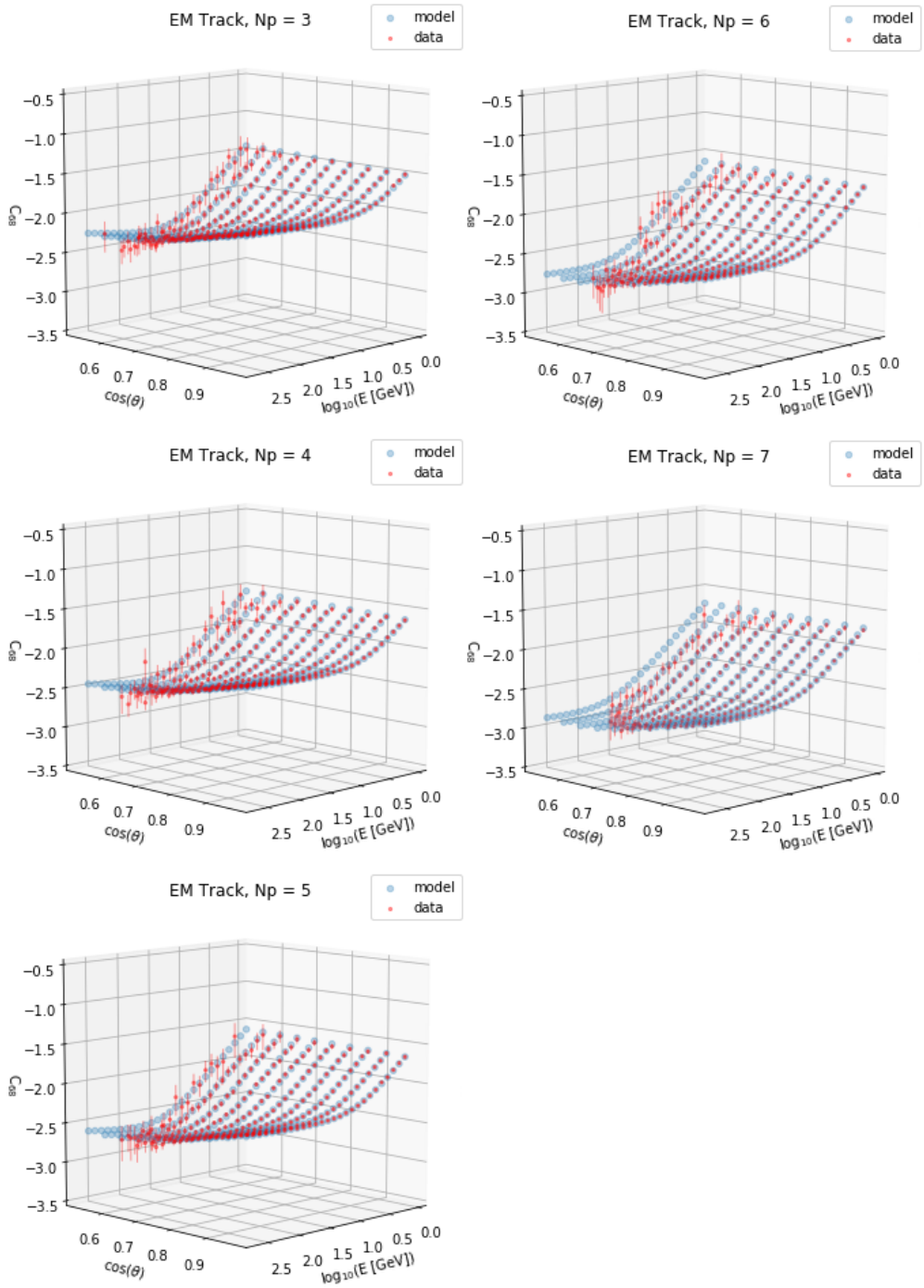

Figure 3.12: Simultaneous 2D fits of the angular resolution in energy and zenith angle for EM Track events. Red points are data and the blue grid shows the fit function value at the same points.

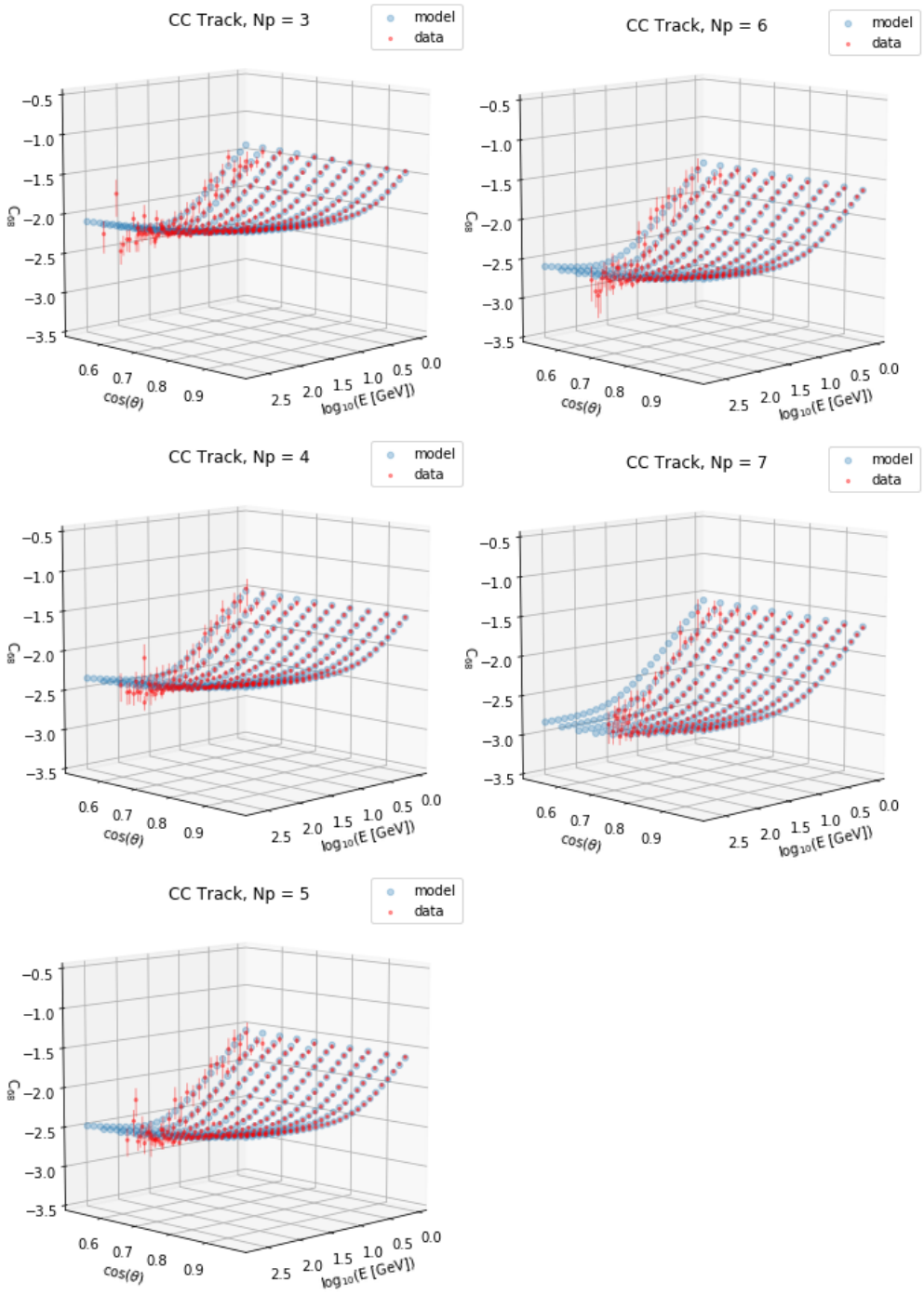

Figure 3.13: Simultaneous 2D fits of the angular resolution in energy and zenith angle for CC Track events. Red points are data and the blue grid shows the fit function value at the same points.

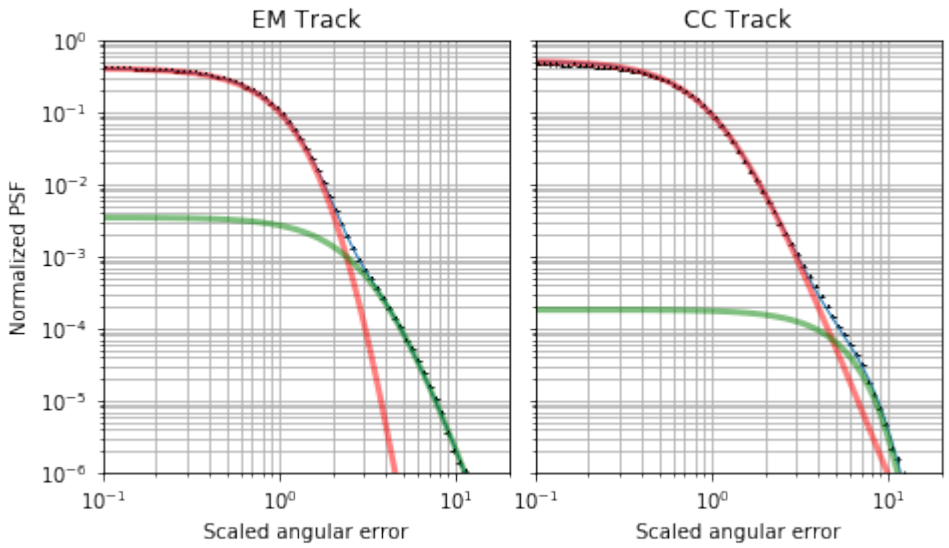

Figure 3.14: Fits for the PSF distributions constructed with the zenith angle-dependent scaling functions for the angular resolution.

uncertainties in the form of a large error on the parameter γ, which controls the steepness of the decay. This uncertainty is due to the relative insensitivity of the net function to the value of γ because of the large contribution of the core function at all values of x.

Despite the clear dependence of the angular resolution on the zenith angle at higher energies, the importance at energies below $\sim$10 GeV is minimal in regards to actual data analysis results. This is briefly discussed in more detail in Chapter 4 through its effect on the PSF validation and the flux measurements of bright point sources.

Chapter 4. Gamma-ray Observations with CAL

4.1 Observation Overview

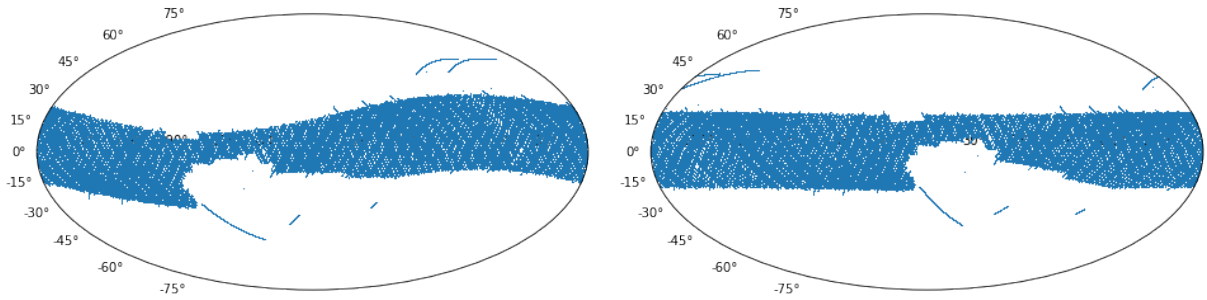

Figure 4.1: Flight data event directions. Position of the CAL in geographic (left) and geomagnetic (right) coordinates during LE-γ event triggers during the month of January 2016.

The CALET payload was launched and deployed to the ISS in August 2015. After one month of checkout operations and minimal mission success testing, scientific data collection began in late September. However, the data used in this work starts in November 2015, as the LE-γ run mode was not active on-orbit until then. LE-γ data are taken at low declinations, specifically tuned such that the geomagnetic field prevents significant contamination by low-rigidity charged particles. In geomagnetic coordinates this corresponds to geomagnetic latitudes between $\pm 20°$. Figure 4.1 illustrates this observation plan using one full month of LE-γ triggers. The instrument is not active in the South Atlantic Anomaly (SAA), creating the gap in the observation band. Observations outside of the normal region correspond to times of lowered thresholds from CGBM triggers.

4.1.1 Data Handling and Processing

Flight data handling for CALET has many stages. The raw instrumental data, referred to as Level 0, is downlinked from the ISS to the Japanese Aerospace Exploration Agency (JAXA). Some packet loss occurs in the downlink and the data are corrected over the course of approximately one week to mitigate this loss. The data are moved to the Waseda CALET

Operations Center (WCOC) and processed to Level 1, the low-level format distributed to the full collaboration. A large, robust dataset referred to as Level 2 is created through the application of calibrations, the fitting of tracking algorithms, and the setting of various flags indicating the validity of each event for analysis.

The Level 2 dataset is centrally processed at the WCOC to ensure fundamental data consistency between the collaborators worldwide. Due to the prohibitive size, however, the Level 2 dataset is distributed incrementally through the delivery of physical hard drives rather than transferred over a network. The analysis presented in this chapter is performed on a version of Level 2 current as of April 2018. Further details of the instrument operation and data handling are given in Asaoka et al. (2018).

4.1.2 ISS Structures

For the gamma-ray analysis, an unexpected source of background was discovered in the first six months of data collection. Mentioned briefly in Section 3.4.1, several structures of the ISS are visible in the CALET FOV. While fixed structures can be accounted for through the simple application of a mask at the event selection level, it was discovered that time-dependent features appear as well. In addition to periodic obstructions such as the solar panel arrays or the Active Thermal Control System radiators, the robotic arms used for manipulating payloads and parts of the station are sometimes present. In the most extreme case, the Space Station Remote Manipulator System (SSRMS) occupied nearly 1/4 of the CALET FOV for nearly one full month.

Discussions between JAXA and NASA have established general practice that CALET will be taken into account when determining where to park the SSRMS and more thorough communication of the movement of different structures is being established. A robust treatment of the background at the data analysis level is still in development. Thanks to the efforts of JAXA personnel, the time-dependent positions of many (not all) structures is now known well enough to flag events based on whether their direction is clear of obstructions (Figure 4.2). Accounting for these vetos in the calculation of the CAL exposure in

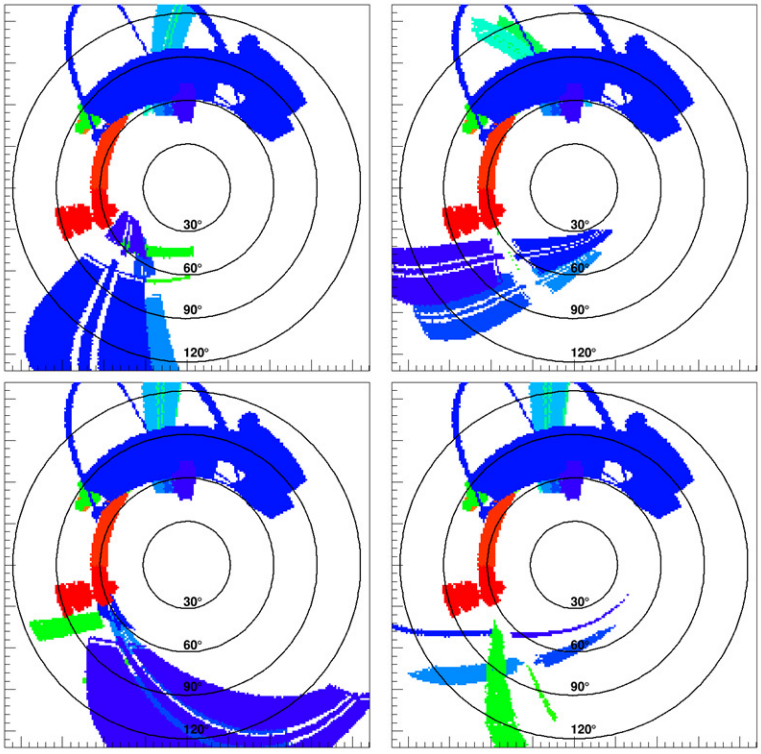

Figure 4.2: Time-dependent ISS structure obstructions. Fish-eye views for four different snapshots in time of the ISS structures in terms of the CALET coordinate system. Note that the 60° circle roughly indicates the edge of the CAL FOV. The rotation of the solar panels (shown in blue in the lower FOV) in the lower half of the FOV is clear between the frames. In the upper left frame, the radiator (shown in bright green) can be seen in the lower half of the frame. Finally, the upper blue structure is the JEM-EF and the red structure is the main body of the ISS.

celestial coordinates is more challenging and the feasibility of their inclusion in the already computationally expensive calculation is being explored.

For the analysis of point sources, the flux in a region surrounding a source can be used to estimate a constant background that includes charged particle contamination and the ISS background. For the galactic diffuse emission the background contamination is harder to avoid and a very restricted FOV is used.

4.2 Dataset Extraction and Exposure Generation

For the following analyses, two data products are necessary: a set of gamma-ray candidate events together with their energies, directions, etc. and an exposure generated

incorporating the instrumental observation time, pointing direction and orientation, and the effective area as a function of energy and FOV pixel. The reconstruction algorithms and selections for the gamma-ray candidates were described in detail in Chapter 3 and the resulting effective area was derived. In this section, additional information pertaining to the calculation of the other required quantities is provided.

The Level 0 and Level 1 datasets contain data volumes updated on a periodic basis (1 volume per second) and on an event-by-event basis (many events per second). The live time of observation (the time for which the instrument was available to trigger) is not included in this information directly included in the instrumental data, but the cumulative dead time (e.g. time required for the electronic readout of the detector elements) is included in the periodic data. Since there are multiple events per periodic data volume, the live time per event must be approximated. The real time difference between two periodic volumes is calculated using timestamps from the on-board computer. Using the difference in the cumulative dead time between the two periodic volumes, a total live time is determined for the period and is divided evenly among the events triggering therein. This uncertainty is immaterial for the electron analysis over long time periods as the total live time is the relevant quantity for calculating the flux. For the gamma-ray analysis, a more precise determination would be ideal. However, given the small amount by which the pointing direction changes over such a time scale and the more significant error introduced by the necessary pixellization of the sky, this averaged live time is acceptable.

As mentioned in Section 2.3, the ASC is the primary means by which the pointing direction of the CAL is determined. Correlating images at zenith pointing with reference star maps, a rotation quaternion between instrument and celestial coordinates is generated. At times, however, the ASC is unable to find reasonable matches with star maps due to the presence of the Sun or Moon in its FOV. In these cases, the telemetry stream of the ISS can be used instead to determine the pointing direction (albeit with somewhat lower accuracy). Using times where both ASC and ISS orientations are available, a correction quaternion for

rotating between the ISS reference system and the CALET coordinate frame is determined. Then, for short time gaps when the ASC data are not available, the rotated ISS orientation is used to convert directions to celestial coordinates. For rare periods where larger gaps exist, the quaternions are interpolated using Spherical Linear Interpolation (Shoemake, 1985). These calculations are performed in the generation of the Level 2 dataset. In Section 4.3, the approach and its long-term stability are validated using the signals from bright pulsars.

The generation of the exposure is computationally expensive. The effective area is discretized in pixels for the CAL FOV and the sky in celestial coordinates is similarly divided. Given the energy-dependence of the effective area, a separate exposure map must be generated for each energy bin. Each time the exposure maps are incremented, the direction vector to each sky pixel in celestial coordinates (equatorial or galactic) is rotated into the CAL instrument frame according to the orientation quaternion discussed above. Each pixel is then incremented by the appropriate effective area for its position in the FOV and the energy bin corresponding to the map, scaled to the live time. In order to complete this task in a manageable time, the live time is buffered for events until a threshold is met, then the exposure is incremented using the orientation for the final event. Given an orbital period of approximately 90 minutes, the pointing direction of the instrument shifts by roughly 0.07° per second. The buffer time used in the analyses that follow, 5 seconds, then corresponds to a maximum uncertainty in pointing direction of $\sim 0.35^\circ$. The order of the HEALPix scheme used in the analysis (nside $= 2^6$) corresponds roughly to a 1° resolution, larger than the error imposed by the live time buffering by nearly a factor of 3.

Combining the extracted datasets and the exposure on the sky, Figure 4.3 gives a clear view of the objects analyzed in the remainder of this chapter. The Galactic plane is clearly visible, as are the Crab, Geminga, and Vela pulsars and the Active Galactic Nucleus (AGN) CTA 102 in a bright flare state.

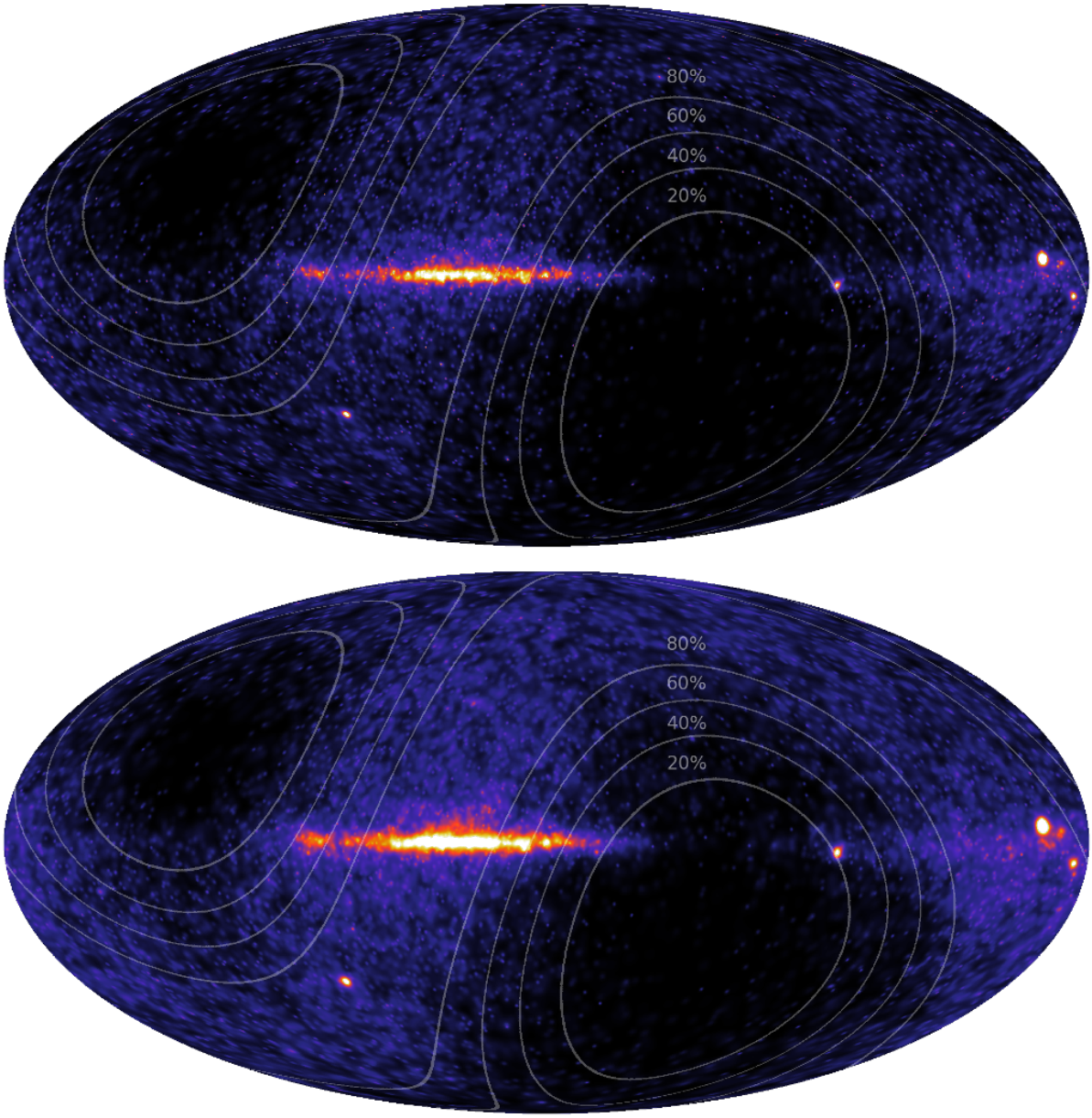

Figure 4.3: Flight data count maps. Maps of the photon candidates in galactic coordinates from the EM Track (top) and CC Track (bottom) analyses smeared by the angular resolution for each event individually for the two years between 2015/11/01 - 2017/10/31. The white contours correspond to various levels of the exposure with respect to the maximum. In regions where it is viewed, the Galactic plane can be seen prominently along the center of the maps. At the far right, the Geminga and Crab pulsars are clearly seen. The Vela pulsar is seen nearer the Galactic center, but is viewed consistently near the edge of the FOV. Below the Galactic plane, the AGN CTA 102 prominently appears due to a very bright flare in late 2016 - early 2017.

4.3 Measurement of Bright Point-sources

With the PSF characterized in Section 3.4.4, it is possible to define the energy-dependent confinement radii for association of photon candidates with a given location on the sky for any given efficiency. As a result, given the position of a source, it is straightforward to measure the observed signal consistent with origin at that source. In this section the analysis of three bright pulsars using the CAL LE-γ data is described for the purposes of determining the accuracy with which a point source can be localized, presenting the best determination of the flux currently possible with the CAL, and efficiently characterizing the background implicit in this derived flux.

4.3.1 Consistency of Observations with the Simulated PSF

For this study the Geminga, Crab, and Vela pulsars are considered due to the relatively high number of associated photon candidates detected with the CAL. These sources are clearly visible in the sky maps shown in Figure 4.3.

Nominal source positions are taken from the Fermi-LAT 3FGL[1] catalog of bright point sources (Fermi-LAT Collaboration, 2015). Given the potential for small discrepancies in the coordinate frames used in the reference sky maps of the ASC and in the 3FGL catalog, a log-likelihood minimization is performed to find the best fit position for the sources in the CAL data. The function minimized is

$$\begin{aligned} -2L &= -2 \log \left(\prod_i P(x_i) \right) \\ &= -2 \sum_i \log P(x_i) \end{aligned} \tag{4.1}$$

where i spans the events selected near the source and $P(x_i)$ is the value of the PSF (given by the fits of Equation 3.9 using the scaling functions with the form of Equation 3.4) for event i. For the determination of the source position, the 99% containment radii according to the PSF for EM Track and CC Track are used relative to the catalog position to avoid

[1] https://fermi.gsfc.nasa.gov/ssc/data/access/lat/4yr_catalog/

confusion from other sources. Figure 4.4 shows the result of the minimization for each source and tracking algorithm. The shifts found for EM Track and CC Track differ slightly in magnitude, but are consistent in direction with respect to the 3FGL coordinates. This suggests an overall rotation in the coordinate system, which is discussed in Section 4.3.2.

These best fit positions for the pulsar positions are used in the analysis in Section 4.3.3. Additionally, they can be used in a validation of the simulated PSF derived in Section 3.4.4. Taking the scaled angular errors x calculated as the difference between candidate position and best fit source position, an empirical probability density can be constructed analogously to the treatment of the simulated dataset.

The resulting distributions are shown in Figure 4.5. A constant background term is added to the PSF to achieve consistency with the observed distributions. This is justified by the background produced by the galactic diffuse emission, especially in the region of the Galactic plane (where all three sources are located). Another source of background that should scale purely with exposure is residual charged particle contamination after the gamma-ray event selection. In this study, given the relative flatness of the galactic background in the narrow source windows, no distinction between the contributions of these backgrounds is made.

The improvement of the characterization of the angular response with the inclusion of the zenith angle dependence introduced in Section 3.4.5 is tested by repeating the above analysis using the scaling functions with form according to Equation 3.11 and the corresponding PSF fits. No significant difference is found by using this expanded treatment of the response (see Figure 4.6). This suggests that the error introduced by neglecting the zenith-angle dependence of the angular resolution is insignificant compared to the other systematics currently present in the analysis.

4.3.2 Absolute Pointing Accuracy

The signal from bright point sources can also be used to test the accuracy and stability of the orientation determination described in Section 4.2. Taking the 3FGL to be a fully

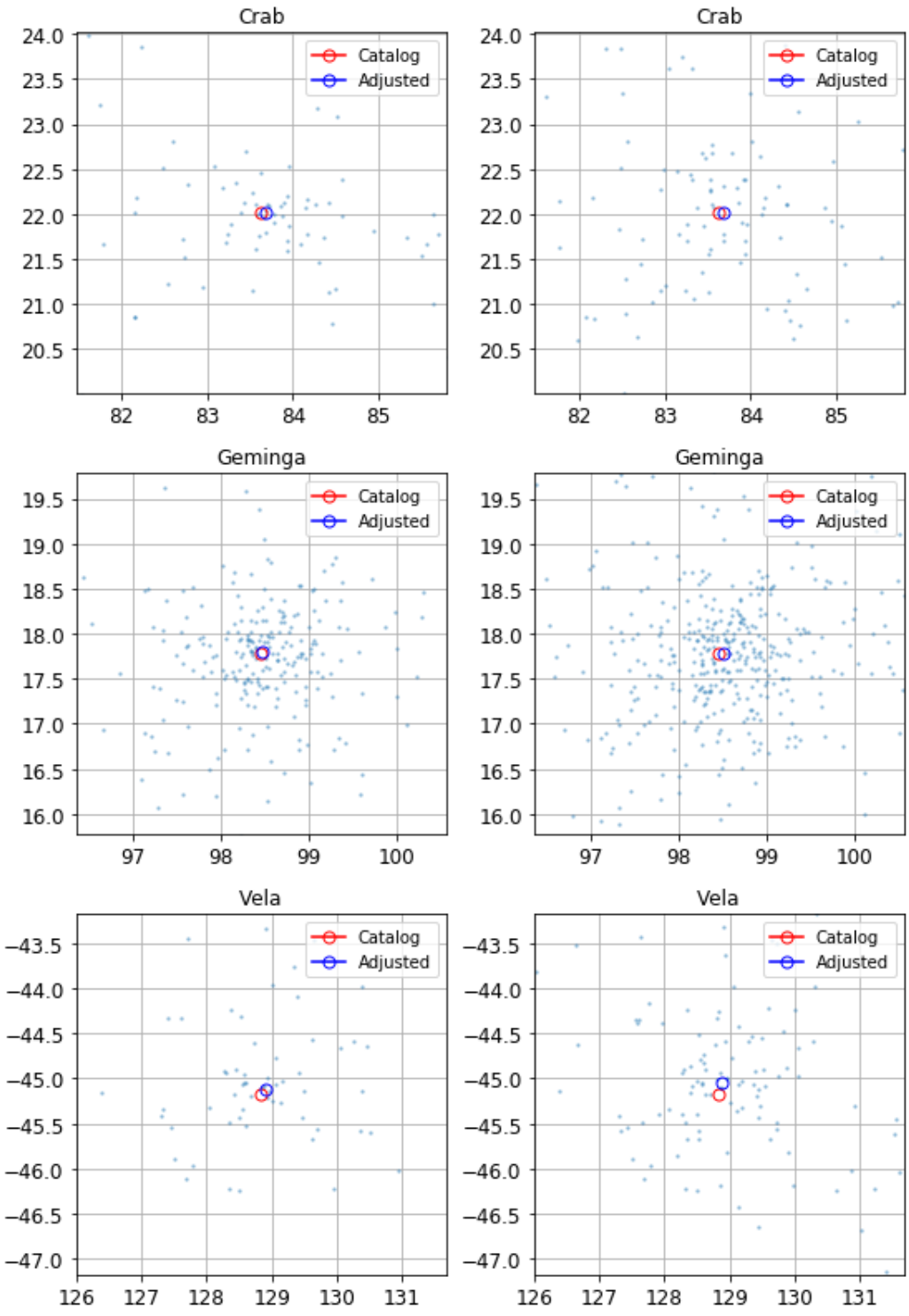

Figure 4.4: Corrected pulsar positions. Catalog and best fit positions for the Crab, Geminga, and Vela pulsars for the EM Track (left column) and CC Track (right column) algorithms.

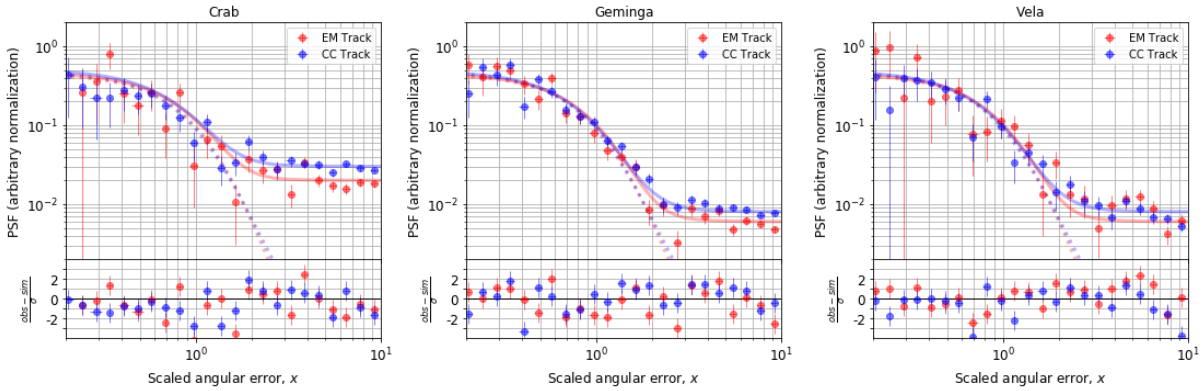

Figure 4.5: Distributions of scaled angular errors in the flight data relative to the best fit pulsar positions. The dotted lines in each frame show the unmodified PSF function, while a constant background term has been added to obtain the smooth lines. Residuals are shown in the lower frame in units of the observational statistical error.

self-consistent catalog, the residual differences between the catalog and CAL positions after removal of any overall coordinate frame rotations represent the current limit of CAL pointing determination. To remove such an overall rotation, a correction quaternion is obtained using a log-likelihood minimization. For the discussion that follows, only the EM Track is considered due to the better angular resolution and lower background contribution as compared to CC Track.

The likelihood function is constructed with the quaternion components as the free parameters for optimization. The gamma-ray candidate arrival directions are rotated by the correction quaternion. The scaled angular errors, x, are calculated using the angular difference between the arrival direction for an event and the 3FGL position of its associated source. The log-likelihood is determined as in Equation 4.1, again using the PSF for the probabilities. This calculation is again restricted to x corresponding to the 99% containment radius of the PSF. In addition to the pulsars considered previously, CTA 102 (visible south of the Galactic plane in Figure 4.3) is also used given its high signal over background.

After obtaining the coefficients for the correction quaternion, the rotation is applied to the candidate directions in the CAL flight dataset. The best fit positions for the sources are again obtained and the residual angular difference is found with respect to the cata-

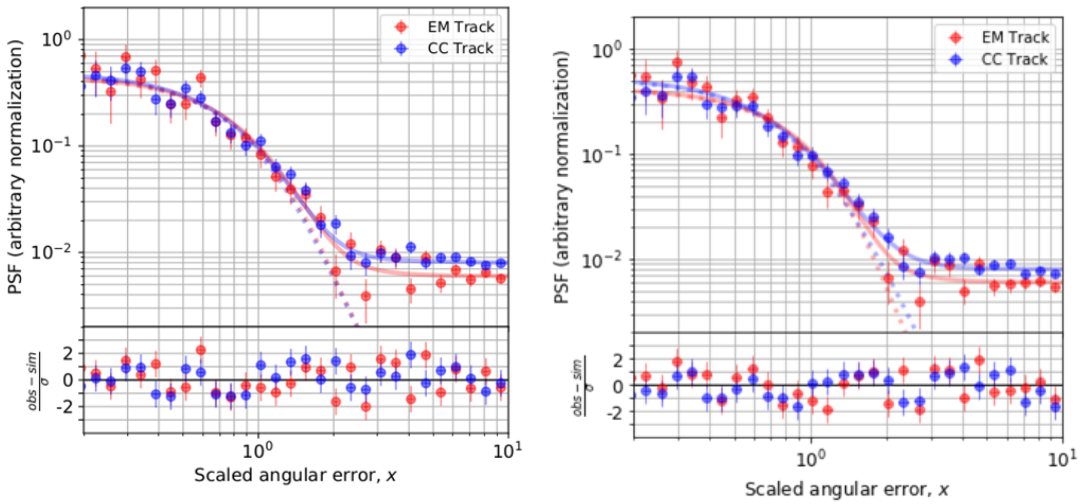

Figure 4.6: Flight data empirical PSF for Geminga. Density of events near the Geminga source position compared to the simulated PSF using the scaling functions not including event incidence angle (left) and the scaling functions incorporating incidence angle dependence (right).

log positions. The results for the four sources are shown in Table 4.1. The discrepancies in position are less than 0.1° for all of the sources, which satisfies the design goal of the calorimeter for pointing determination. The residual error in the position is largely consistent with the fitting errors on the source positions, which range from 0.02° for Geminga to 0.06° for Vela. These figures represent the current statistics-limited pointing accuracy for CALET and therefore an upper limit on the absolute pointing accuracy, demonstrating the stability of the orientation determination over the first two years of observation.

Table 4.1: Absolute pointing accuracy. Angular separation between CAL best fit source positions and 3FGL catalog source positions before and after application of a correction quaternion.

Source	Diff. before rotation [deg.]	Diff. after rotation [deg.]
Crab	0.11	0.049
Geminga	0.047	0.018
Vela	0.19	0.088
CTA 102	0.12	0.048

4.3.3 Calculation of Fluxes

The differential photon flux in energy bin i for a point-like source can be written as

$$\left(\frac{d\Phi}{dE}\right)_i = \frac{N_i}{\Delta E_i (S_{eff}T)_i} \tag{4.2}$$

where N_i is the number of photons in the bin associated with the source, ΔE_i is the width of the energy bin, and $(S_{eff}T)_i$ is the accumulated exposure at the source position. With the energy bin size determined by choice in the analysis and the exposure calculated according to the methodology described in Section 4.2, the only term left to consider is N_i.

The association of events with sources, as in the previous section, is performed using the PSF with a set efficiency. The size of the source window is important - a larger window contains a larger fraction of the events truly associated with the source, but also includes a larger background contribution. For the results in this section, the source window is chosen to correspond to the 99% containment radius according to the PSF for each tracking algorithm and the number of events therein is scaled by 1/0.99 to account for the corresponding inefficiency in the measurement.

The background for the measurement is a function of the exposure, nearby sources, and the contribution of the Galactic diffuse flux in the region of interest. In this section, the Crab, Geminga, and Vela pulsars are analyzed for the consistency of the flux measured by the CAL with established results from Fermi-LAT. For the 99% containment radii of the PSF fits, the source regions are well-separated and the dominant background is due to charged particle contamination and the galactic diffuse emission. We can estimate this background by checking the flux in a small annulus beyond the source window.

Figure 4.7 shows the selected event distributions for the source and background regions for the pulsars. Although the signal windows for Crab and Geminga are well-separated, there is overlap of the background apertures. The number of events associated with Crab, Geminga, and Vela, respectively, are 81 (185), 242 (458), and 63 (138) for the EM Track

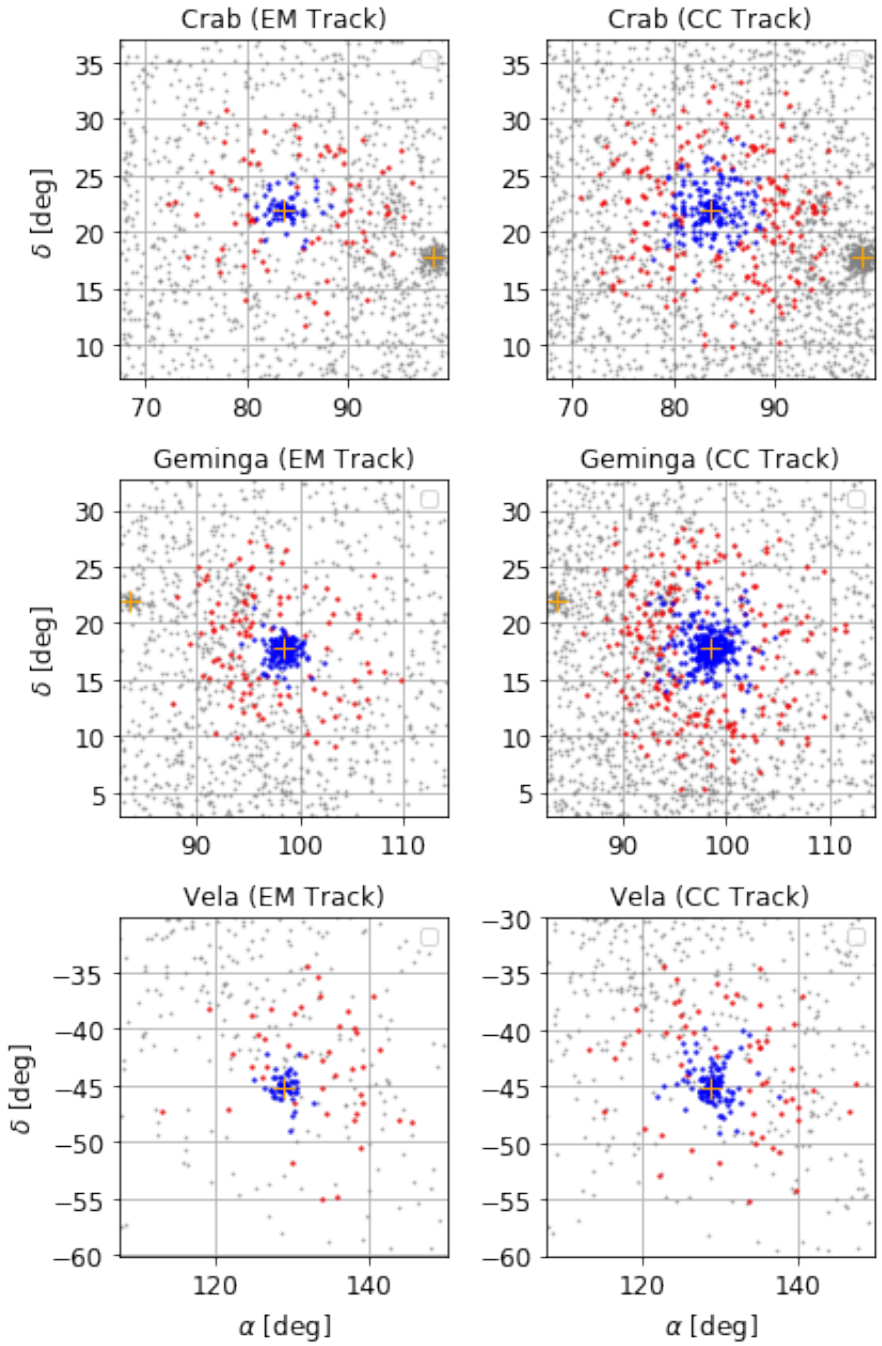

Figure 4.7: Selected events for the pulsar flux calculation. Selection of events associated with the source (blue points) and the background (red points) regions for the EM Track (left column) and CC Track (right column) for the Crab, Geminga, and Vela pulsars. Gray points are events not associated with the signal or background regions. Source positions are marked with orange crosses.

(CC Track) algorithm. Note that the large difference in these numbers is due to the increased CC Track efficiency at low energies. These numbers differ (and are generally lower) than the expectation given in Moiseev et al. (2013) and Cannady et al. (2015). In the both cases a major contributor was an overestimation of the duty cycle for low energy observations. This is especially noticeable in that the signal from Vela was expected to be higher than that from Geminga. Because of the operation of the LE-γ run mode only at low latitudes, the exposure of Vela is considerably lower than expected. Furthermore, the effective area was also previously overestimated (i.e. Mori et al. (2013)) due to uncertainties in the efficiencies for identification and track reconstruction in the development stages of the analysis.

The number of events in each energy bin for the signal and background regions is determined, and the background contribution is scaled in solid angle to match the source aperture size. This scaled background is subtracted from the signal from the source window and the flux is then calculated according to Equation 4.2. The results are plotted in Figure 4.8. For comparison, parameterized fluxes published by Fermi-LAT (Crab: Abdo et al. (2009a), Geminga: Abdo et al. (2010), Vela: Abdo et al. (2009b)) are shown by the black lines.

Chi-squared statistics are calculated for the results to check the consistency with the Fermi-LAT fluxes. Despite a relatively high background fraction, the Crab measurement gives a chi-squared of 4.64 (4.16) with 7 degrees of freedom. Vela is not found to be consistent with the published flux (chi-squared of 39.1 (32.9) with 9 degrees of freedom). Consistent measurement at the edge of the FOV contribute unclear systematic effects including potential errors in the exposure calculation and contamination from masked ISS structures (due to the relatively poor angular resolution at low energies ($\sim$1 GeV). Relatively low statistics for both the signal and background regions also contribute to fluctuations in the background subtraction, leading to over-subtraction in some energy bins and under-subtraction in others.

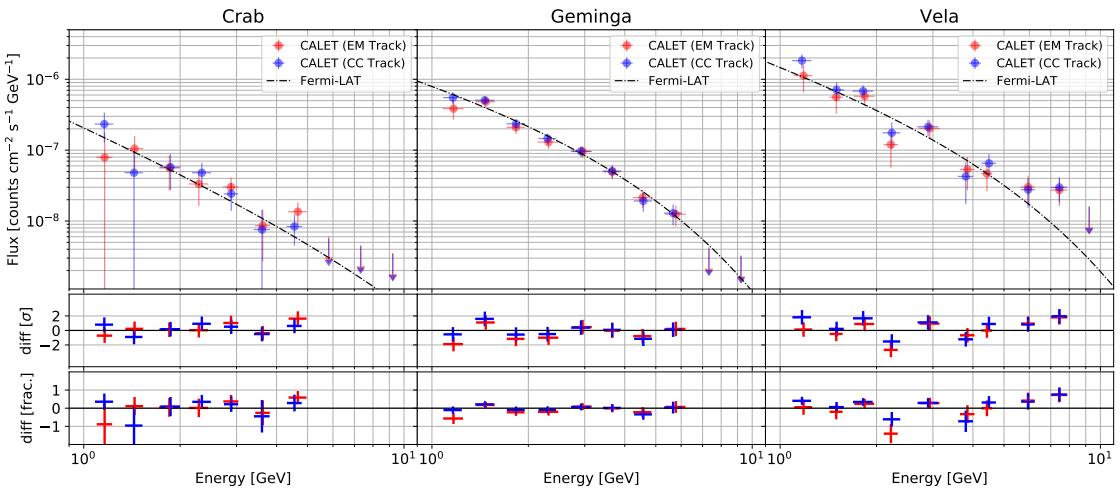

Figure 4.8: Fluxes for bright pulsars. Frames show fluxes of the Crab, Geminga, and Vela pulsars as measured in the CALET calorimeter. Red and blue points show the EM Track and CC Track algorithms, respectively. Error bars on these points are statistical only. The black curves show Fermi-LAT parameterized fluxes for comparison.

Geminga is measured with a high signal over background and is found to be consistent with the LAT spectrum with chi-squared statistics of 6.73 and 5.74 for EM Track and CC Track, respectively, with 8 degrees of freedom. Given the relatively high statistics, the spectrum is fitted with three function templates: a power law, a broken power law, and a power law with exponential cutoff. The single power law fit is excluded by the observations, but the other functions are both found to be consistent. The fits and their corresponding chi-squared statistics are shown in Figure 4.9. The broken power law best fit gives a break energy $E_{th} = 3.7$, low-energy index $\alpha_1 = 2.1$ and high energy index $\alpha_2 = 4.1$. The cutoff power law is slightly favored by the data, and the best fit parameters give a spectral index of $\alpha = 1.19$ and cutoff energy $E_c = 2.04$. The cutoff power law is also the best fit reported by Fermi-LAT, and parameters are within errors of those found in this analysis.

When the calculation of the fluxes is repeated including the zenith-angle dependence of the angular resolution, the fluxes shown in Figure 4.10 are obtained. Again, no significant improvement is found in the more rigorous treatment: for Crab using EM Track (CC Track), χ^2/ d.o.f. = 5.05/7 (2.88/7); for Geminga, χ^2/ d.o.f. = 7.08/8 (6.06/7); for Vela, χ^2/ d.o.f.

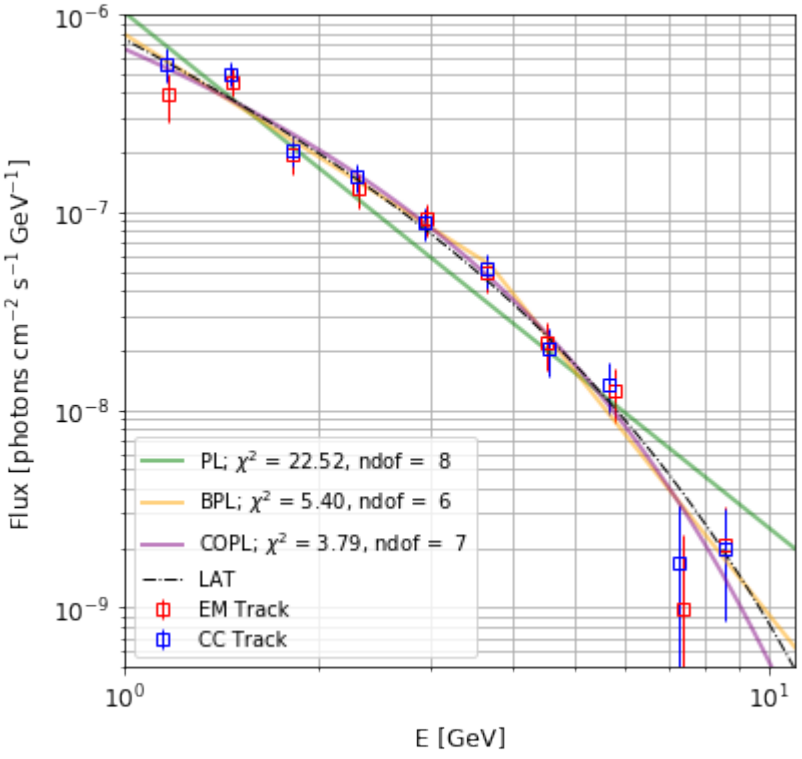

Figure 4.9: Fits with different template functions for the Geminga flux.

= 50.1/9 (33.9/9). At this stage of the analysis, we conclude that the added complexity introduced by incorporating the incidence angle for the response is not warranted.

4.4 Diffuse Galactic and Isotropic Emission

An additional validation of the instrument response characterization is the consistency of the measured diffuse gamma-ray signal with expectations based on long-term Fermi-LAT observations. For this comparison, Fermi-LAT Pass 8 data are pulled from the public archive[2] for the time period from August 2008 to March 2017. An averaged flux map is calculated using these public data for energies up to 100 GeV. No removal of point sources is included in this treatment. As a consequence, this is not an independent measurement of the diffuse fluxes, but a test of the consistency of the CAL observations with the established LAT measurement.

[2]https://fermi.gsfc.nasa.gov/ssc/data/access/lat/

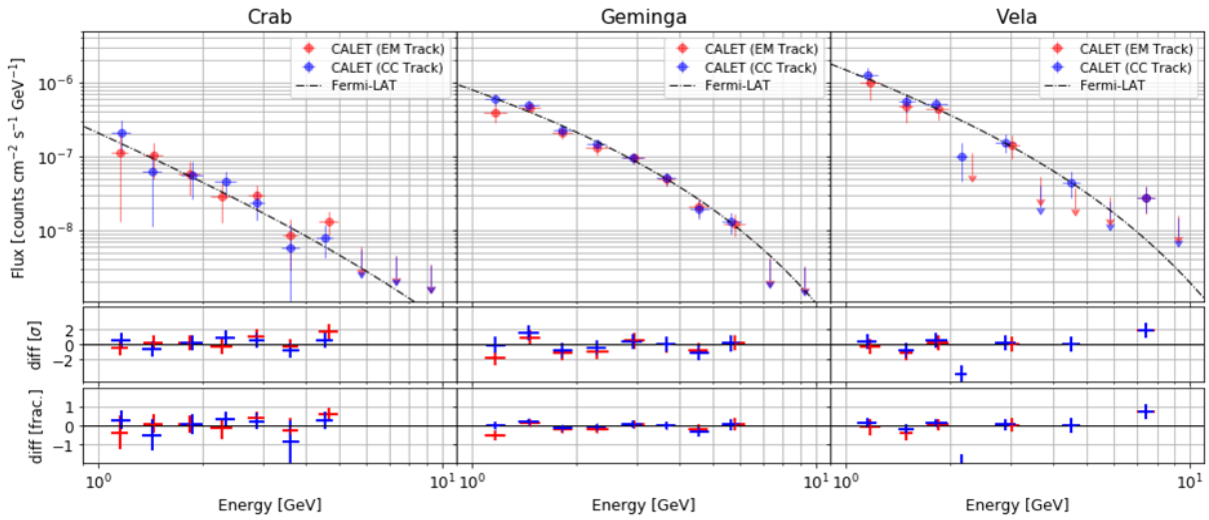

Figure 4.10: Zenith-angle dependent pulsar fluxes. The scaling functions taking into account the dependence on the incidence angle of each event and the corresponding PSFs were used.

For the analysis in this section, a very restricted FOV was used. Based on investigation of the excess photon candidates from time-dependent ISS structures, a limited region was found where the contamination is negligible (Figure 4.11). The effective area is calculated using only this region and the exposure is regenerated using this limit. On average, the value of the exposure is decreased by 75% with this restriction compared to the full observation.

Figure 4.12 demonstrates the calculation of the expectation based on the CAL exposure map and the LAT averaged map as a function of energy. The LAT data as distributed are spatially binned in square pixels of galactic longitude (ℓ) and galactic latitude (b). For each CALET energy bin, a HEALPix map equal in order to that of the exposure is created. Each pixel in the HEALPix map contains multiple pixels of the original map. The fluxes in the original pixels in each new pixel are averaged, weighted by their corresponding solid angle.

With this rebinning, the exposure can be directly applied to the LAT average flux in each sky pixel. Multiplying as well by the energy bin width and the pixel solid angle, an expected number of photons is obtained. We divide the pixels into subsets of on-plane and off-plane. These regions (indicated in Figure 4.13) are defined such that off-plane

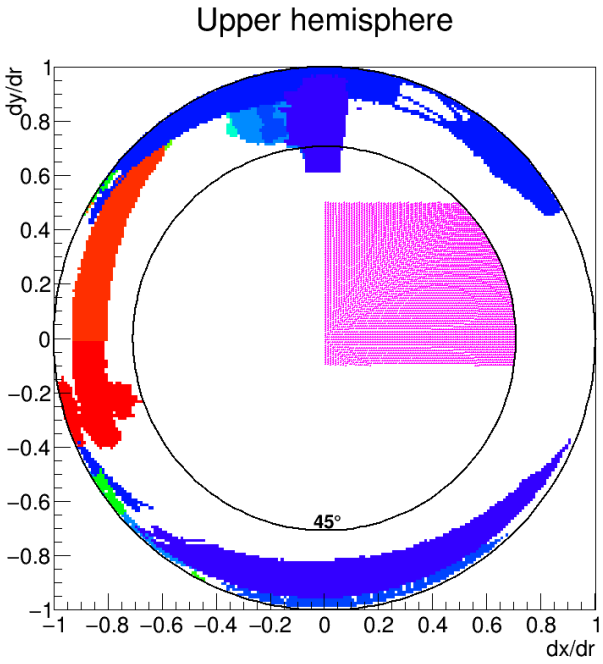

Figure 4.11: Selected clean FOV region. The magenta shaded region is used for the studies pertaining to diffuse emission. It is found to be relatively clear of ISS structures for the full two year period analyzed. Red, blue, and green structures same as described in Figure 4.2.

regions have $|b| > 10°$ and on-plane regions require both $|\ell| < 80°$ and $|b| < 8°$. This guarantees that the on-plane measurement is dominated by the galactic disk emission and is not contaminated by the bright pulsars considered previously.

For both the CAL observations and the expectation based on the LAT flux, we project the number of events into bins of galactic latitude. We restrict the region used to $|\ell| < 80°$ to avoid contamination from the bright pulsars analyzed in the previous section. These distributions are shown in Figure 4.14. For the EM Track result, calculating a chi-squared for the CAL data with respect to the expectation yields 88.34 with 86 degrees of freedom, indicating a high level of consistency. The CC Track result is consistent when limited to $|b| < 20°$, where the chi-squared is 19.15 with 20 degrees of freedom. However, the result as a whole displays an excess at higher latitudes, with a chi-squared of 150 with 89 degrees of freedom.

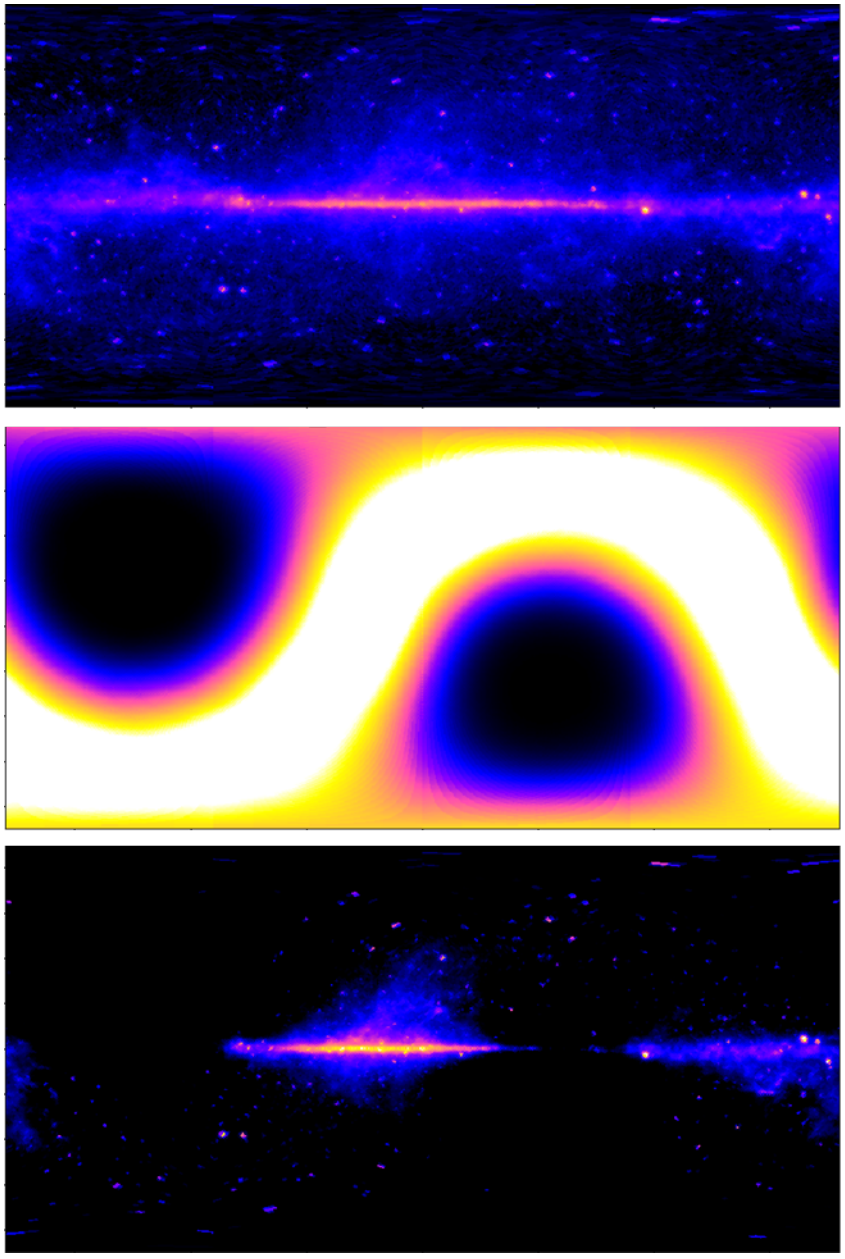

Figure 4.12: Using the LAT averaged map to calculate the CAL expectation for the galactic diffuse emission. *Top:* the LAT map for $E \sim 1$ GeV in galactic coordinates. *Middle:* the CAL exposure for the first two years of LE-γ observations. *Bottom:* the number of photons expected based on the LAT map and the CAL exposure summed over the range 1 GeV $< E <$ 100 GeV.

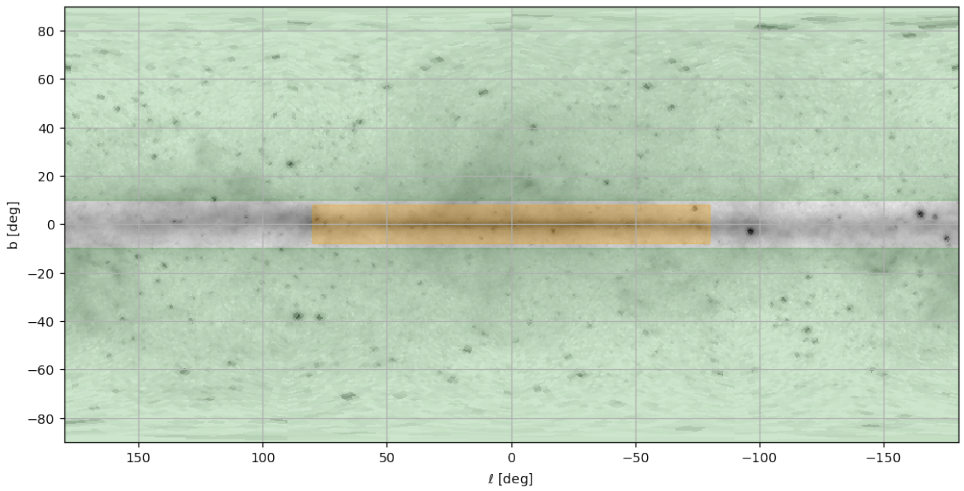

Figure 4.13: Galactic on-plane (orange shading) and off-plane (green shading) regions. The unshaded region is not used in the averaged flux calculation.

This excess is likely pronounced in the CC Track result due to the increased sensitivity for photons with $E < 5GeV$. Unresolved contributions from transient events play a role in the excess. The most extreme example is the signal from CTA 102, which, while seen in both instruments, is averaged over a much longer quiescent time period in the LAT fluxes. Removal of a 5° window around the CTA 102 source position in the above calculations leads to an improved (but still not consistent) chi-squared of 133.6 with 89 degrees of freedom. Additional potential sources of background are unaccounted-for ISS structures entering the limited FOV and residual charged particle contamination.

An additional test of the consistency can be performed by calculating fluxes in each of the energy and sky pixels for the CAL observations. The averaged fluxes on-plane and off-plane should agree with the corresponding quantities from the Fermi-LAT map weighted by the CAL exposure. These averages are shown in Figure 4.15, and immediately show in the off-plane regions that there is some residual background in the CAL observations. Compared to the on-plane measurements, this background is small enough that consistency with the Fermi-LAT expectation is achieved ($\chi^2 = 16.5$ with 19 degrees of freedom for EM Track; $\chi^2 = 5.31$ with 10 degrees of freedom for CC Track).

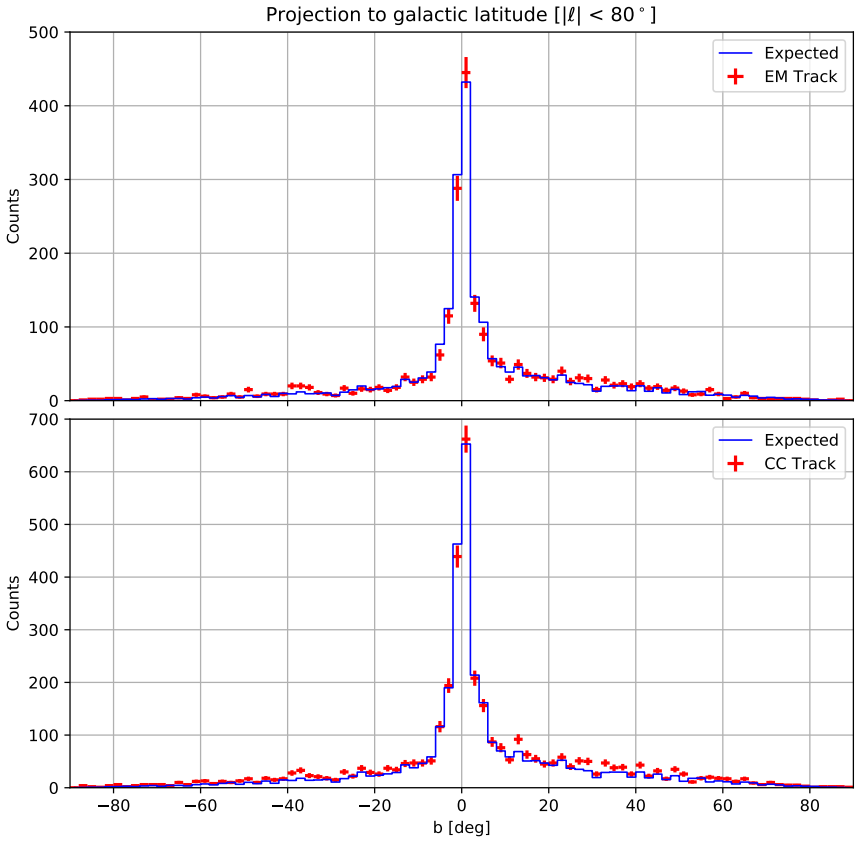

Figure 4.14: Diffuse latitude projection. Number of events in the CAL observations (red points) and the LAT expectations (blue lines) projected onto galactic latitude for the region $|\ell| < 80°$.

As stated in the comparison of the galactic latitude projections, the background could be (at least in part) due to an unhandled ISS structure in the FOV. We also know from the event selection study that there will be some residual charged particle contamination of the gamma-ray dataset. In order to estimate the effect of such a background, EPICS/COSMOS-simulated electrons and protons are fed through the event selection criteria in Section 3.3. The electron dataset is distributed in energy according to an E^{-1} power law for equal population of logarithmic energy bins, and comprises 2×10^7 events per decade spanning the energy range 2 GeV $< E <$ 2 TeV. The proton dataset comprises 3×10^8 events per decade up energies of 20 TeV also logarithmically distributed.

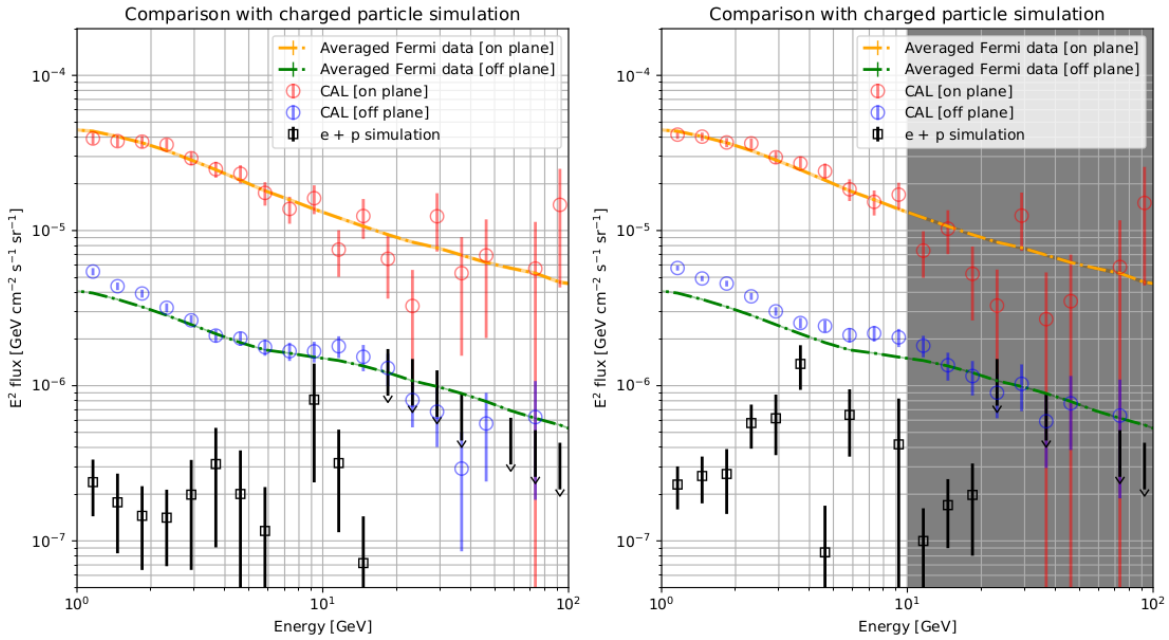

Figure 4.15: Average fluxes calculated in the on-plane and off-plane regions. The left and right panels represent the CAL measurements for EM Track and CC Track, respectively. The open circles show the CAL averages on-plane (red) and off-plane (blue). The error bars represent the error in the weighted mean of the sky pixels. The dashed orange and green lines show the corresponding averages of the Fermi-LAT fluxes, where the shaded region gives the 1σ errors on those figures. The black points give the estimated charged particle background based on simulations considering protons trapped in the magnetosphere and cosmic-ray electron and proton fluxes.

The events are weighted to mimic real electron and proton fluxes on-orbit. The proportion of time the LE-γ run mode is active at varying L-shell parameters is calculated. The electrons are then weighted to reproduce the CALET electron flux, taking into account the variation of the rigidity cutoff corresponding to the time at different L-shell. The protons above 30 GeV are weighted to match the maximum of the CREAM-III flux (Yoon et al., 2017) and the AMS-02 flux (Aguilar et al., 2015) in order to obtain a conservative estimate. At lower energies, the PAMELA results for galactic cosmic-ray protons and downward-moving albedo protons (Adriani et al., 2015) are used. Similar to the weighting in L-shell, this requires calculation of the fraction of LE-γ observation time spent at different latitudes in Altitude Adjusted Corrected Geomagnetic Coordinates (Shepherd, 2014),

the frame used by PAMELA. The results of the simulated contamination are shown by the black data points in Figure 4.15. While the level of the contamination is similar to the excess seen in the off-plane measurements, the shape of both are non-trivial and do not adequately agree to definitively explain the discrepancy with the LAT average.

4.5 The Bright Flare of AGN CTA 102

Starting in late October 2016, a bright flare of the AGN CTA 102 was detected by the CAL and remained clearly visible for 2 months. The first peak in the flare was observed in December, with smaller peaks following in February and April of 2017. Additionally, a smaller, earlier flare was detected in February 2016. Both of these flares were also detected by Fermi-LAT, reported in ATel 8722 (2016) and ATel 9869 (2016).

Figure 4.16 shows a time-dependent analysis of the signal seen in the CAL from CTA 102. In a quiescent state, only a few photons per month are seen. The flare states previously mentioned are clearly visible in the monthly frames in the lower panel of the figure. Low event statistics when the system is not flaring limit the investigation of a change in spectral shape. Additionally, a better treatment of the background from ISS structures is necessary for a robust result. The analysis of this system is ongoing, but demonstrates the ability of the CAL to detect GeV-energy emission from such long-term flaring systems.

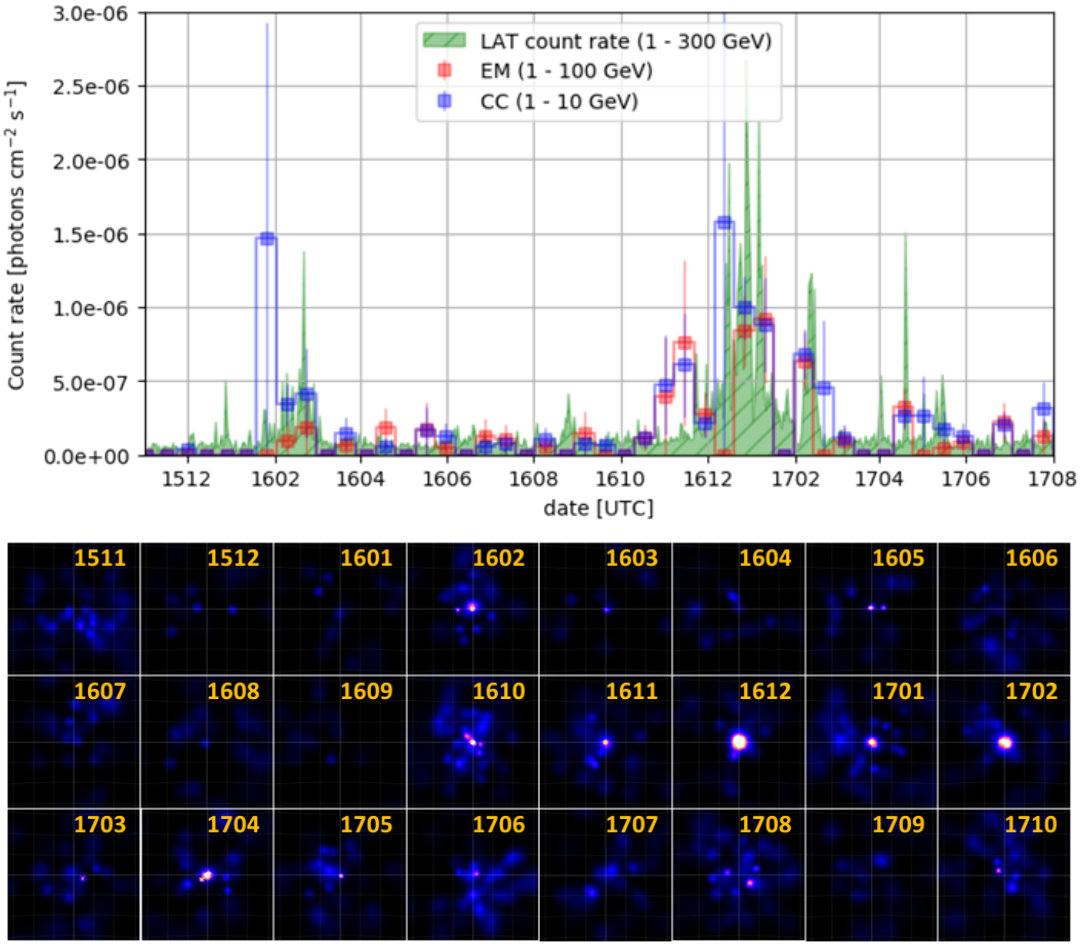

Figure 4.16: Time-dependent behavior of CTA 102 in CAL observations. Note that, due to the precession of the ISS orbit, the exposure of CTA 102 varies by tens of percent month-to-month. *Top:* Counts per exposure over the two year observation period. The red and blue connected points represent the CAL observations with EM Track and CC Track, respectively, with statistical error bars. The green shaded region gives the Fermi-LAT count rate for CTA 102 over the same time range. *Bottom:* Monthly frames of the signal seen from CTA 102 in the CAL using CC Track.

Chapter 5. Transient Event Search and Automation

The previous discussion has described the CAL GeV gamma-ray analysis and demonstrated the CAL performance. Although the CAL sensitivity for steady sources is less than that of Fermi-LAT, CAL is a very useful instrument for observations of transient high-energy events.

Counterparts to GRBs at GeV energies, in general, and particularly to gravitational wave triggers, are a major observational target for CALET. Initial upper limits for gamma rays associated with the LIGO GW151226 event were published using a previous analysis in Adriani et al. (2016). The CAL observations pertaining to four subsequent GW triggers, including afterglow upper limits for the NS-NS merger GW170817, have recently been published in Adriani et al. (2018b). These GW counterpart results will be summarized briefly in Section 5.1.

In Section 5.2, the search for counterparts to triggers from CGBM, along with triggers from the Swift and Fermi-GBM instruments is described. An algorithm for the detection of transient events not localized by other instruments is described in detail in the final section of the chapter.

5.1 Gravitational Wave Events

CALET has been active for five LIGO GW events: GW151226 (Abbott et al., 2016), GW170104 (Abbott et al., 2017b), GW170608 (Abbott et al., 2017c), GW170814 (Abbott et al., 2017d), and GW170817 (Abbott et al., 2017e). Of these five events, the CAL FOV only overlapped with the LIGO constrained source regions for two, GW151226 (in LE-γ run mode) and GW170104 (in HE run mode). In spite of an increased sensitivity with this updated analysis for GW151226 as opposed to that in Adriani et al. (2016), no events are found in the window $[T_0 - 525$ s, $T_0 + 211$ s$]$ around the GW trigger time (T_0). For GW170104, no events are found in the window $[T_0 - 60$ s, $T_0 + 60$ s$]$. In the case of GW170817, CAL observations in the two months following yielded no events consistent with the source position known from the optical detection.

In these cases, upper limits can be set on the integrated flux by assuming that the spectrum follows a power law with an index of -2 ($J(E) = AE^{-2}$), typical for Fermi-LAT GRBs (Ackermann et al., 2013a). Using the energy-dependent exposure $X(E)$ in a given pixel, the number of expected events can be calculated as a function of the power law scale, A, by

$$\begin{aligned} N_{exp} &= \int_{E_{min}}^{E_{max}} X(E)J(E)dE \\ &= A\int_{E_{min}}^{E_{max}} X(E)E^{-2}dE \end{aligned} \tag{5.1}$$

With this equation and given an exposure, we have a relation between a number of events and A. From Feldman and Cousins (1998) we get that the 90% confidence upper limit for null detection for a Poisson process with a potential background corresponds to $\lambda = N_{exp} = 2.44$. Inserting this into 5.1, we can solve for A to determine the limiting flux in pixel i.

$$A_i = N_{exp}\left[\int_{E_{min}}^{E_{max}} X_i(E)E^{-2}dE\right]^{-1} \tag{5.2}$$

Inserting A back into the simple power law, the integrated flux is

$$\begin{aligned} I_i &= \int_{E_{min}}^{E_{max}} A_i E^{-2}dE \\ &= A_i\left(\frac{1}{E_{min}} - \frac{1}{E_{max}}\right) \end{aligned} \tag{5.3}$$

Likewise, the energy flux is

$$\begin{aligned} (EI)_i &= \int_{E_{min}}^{E_{max}} EJ_i(E)dE \\ &= A_i\int_{E_{min}}^{E_{max}} E^{-1}dE \\ &= A_i\ \ln(E_{max}/E_{min}) \end{aligned} \tag{5.4}$$

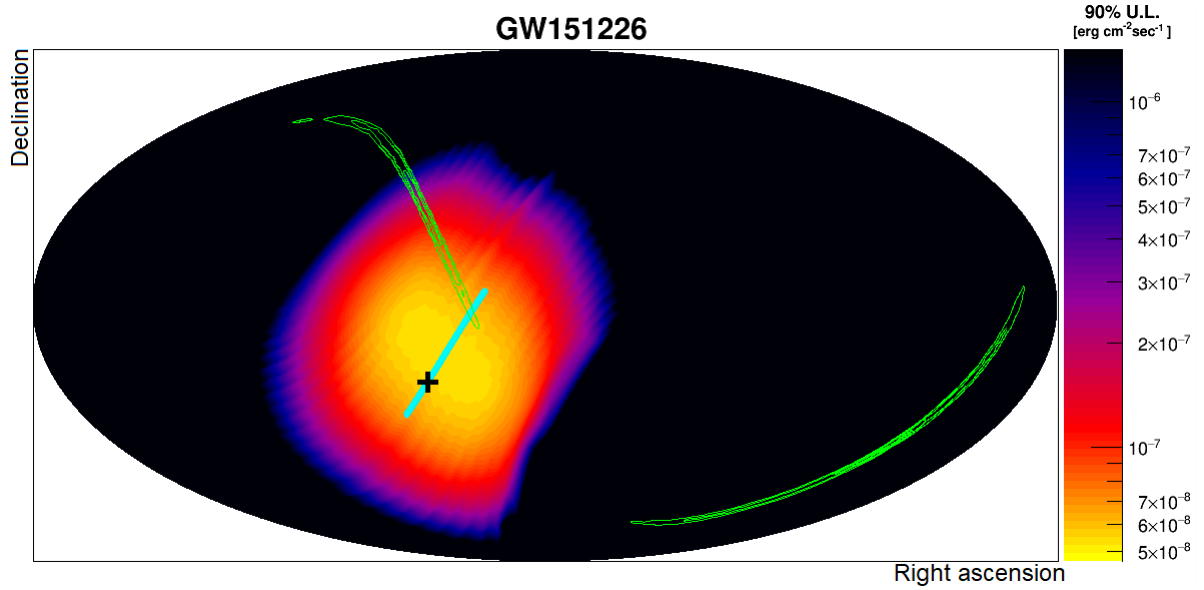

Figure 5.1: CALET search for an EM counterpart to LIGO event GW151226. As discussed in Adriani et al. (2018b). Green contours give the LIGO constrained source regions. The cyan line shows the movement of the CALET zenith pointing during the observation window, with the black crosshatch indicating the trigger time. Intensity map illustrates the upper limits on the energy flux in the 1 - 10 GeV range assuming an E^{-2} power law spectrum.

The resulting sky map with upper limits is shown for the GW151226 event in Figure 5.1. Approximately 15% of the integrated LIGO source region is constrained to an upper limit on energy flux in the 1 - 10 GeV region of 9.3×10^{-8} erg cm^{-2} s^{-1} at the 90% confidence level. A further 10% of the LIGO source region has upper limit 2.8×10^{-7} under the same assumptions.

For the GW170104 event the CAL FOV covered approximately 30% of the integrated LIGO source region. Unfortunately, the CAL was not in the LE-γ run mode so an observation below 10 GeV is not possible. Using the HE run mode data, the limiting energy flux is calculated in the energy range 10 - 100 GeV to be 6.4×10^{-6} erg cm^{-2} s^{-1} in the window $[T_0 - 60$ s, $T_0 + 60$ s$]$.

5.2 Externally-observed GRBs

Public data access for Fermi-GBM[1] and Swift[2] were used to retrieve the trigger times and locations of all GRB events detected by these instruments during the CALET operational period up through May 2018. Checking the LE-γ dataset for photon events with reconstructed direction consistent with the reported position and in a time window [T_0+0.1 s, $T_0 + 60$ s] results in no positive associations. Associated upper limits are calculated as for the GW counterpart search (Eq. 5.4). Limits corresponding to [$T_0 + 0.1$ s, $T_0 + 60$ s] are given in Table 5.1 and limits corresponding to [$T_0 + 0.1$ s, $T_0 + 600$ s] are given in Table 5.2.

In addition, the CGBM trigger list, although lacking positional information, was checked for events within the same time windows. Multiple coincident photons are not seen in the CAL for any of the CGBM triggers checked. Events in the CGBM catalog with reliable localization from Fermi-GBM or Swift are excluded from this blind search since more stringent results are placed in Table 5.1 and Table 5.2. For the remaining triggers, co-detections, if any, are from instruments such as Konus-Wind[3], which has no localization capability, or INTEGRAL-SPI[4], which has a coded mask aperture and can only localize persistent sources.

At this stage, the FOV of these instruments has not been checked for consistency with the CAL FOV due to the lack of publicly available data. Instead, the upper limit as a function of sky position is calculated from the CAL exposure. In Table 5.3, the upper limit at the position of maximum exposure is given for each of the bursts for one minute and ten minute follow-up exposures.

[1] https://heasarc.gsfc.nasa.gov/W3Browse/fermi/fermigtrig.html
[2] https://swift.gsfc.nasa.gov/archive/grb_table/
[3] https://heasarc.gsfc.nasa.gov/docs/heasarc/missions/wind.html
[4] https://www.cosmos.esa.int/web/integral/instruments-spi

Table 5.1: 60 second CAL upper limits for Fermi-GBM and Swift GRBs. 90% confidence level upper limit from CAL observations $[T_0 + 0.1$ s, $T_0 + 60$ s$]$ of Fermi-GBM and Swift event triggers for which LE-γ run mode data is available and the event position is within the CAL FOV. Events with names starting with *GRB* are Fermi events and those suffixed with a single letter are Swift events.

Event	T_0 [s]	α [°]	δ [°]	U.L. [erg cm^{-2} s^{-1}]
GRB151229486	1451389206	346.49	+6.91	1.29e-06
GRB160223416	1456221541	94.994	+33.407	1.53e-05
GRB160419637	1461078995	16.424	-27.343	1.60e-05
160419A	1461078997	16.418	-27.341	1.66e-05
GRB160530667	1464624071	133.48	+43.48	1.36e-05
GRB160628136	1467083781	87.92	+38.17	4.54e-04
160705B	1467752527	168.109	+46.7	9.62e-06
GRB160715298	1468566551	293.73	+21.887	1.54e-06
GRB160720767	1469039036	42.65	+75.68	1.26e-03
GRB160721806	1469128858	38.15	+34.52	1.85e-06
160726A	1469496847	98.809	-6.617	3.19e-06
GRB160726065	1469496847	98.821	-6.644	3.19e-06
160801A	1470043710	212.763	+13.489	1.23e-06
GRB160818230	1471498253	163.6	+37.4	2.00e-05
160824A	1472080945	80.088	+40.028	9.18e-06
GRB160909061	1473384476	242.68	-51.16	2.11e-06
GRB160910722	1473527979	221.442	+39.067	1.24e-03
GRB160917921	1474149937	145.68	+22.95	2.75e-06
161001A	1475283916	71.92	-57.261	1.93e-04
GRB161001045	1475283916	71.918	-57.261	1.93e-04
GRB161105417	1478340048	249.25	-65.217	4.52e-05
GRB161109263	1478672325	157.86	+61.8	3.16e-06
GRB161207224	1481088167	294.81	-9.93	2.00e-06
GRB161217128	1481943825	216.63	+51.98	2.52e-06
161218A	1482032856	245.25	-4.113	1.77e-06
GRB161228405	1482918205	358.42	-24.6	8.28e-06
GRB170121133	1484968252	241.99	+13.81	7.17e-06
GRB170124874	1485291486	282.04	-75.51	8.95e-05
GRB170219002	1487462587	54.843	+50.072	2.57e-06
GRB170228773	1488306780	355.94	+15.73	1.88e-06
170307A	1488918261	13.51	+9.538	1.40e-06
GRB170307851	1488918317	13.535	+9.537	1.40e-06
GRB170313125	1489374028	359.62	+29.27	2.54e-06
170317A	1489743959	93.062	+50.493	7.12e-05
GRB170323058	1490232203	145.19	-39	6.15e-04

Table 5.1 cont'd

Event	T_0 [s]	α [°]	δ [°]	U.L. [erg cm^{-2} s^{-1}]
170330A	1490912991	283.331	-13.431	1.70e-06
GRB170412917	1492034447	201.75	+25.28	3.50e-06
GRB170412988	1492040575	164.38	+22.03	1.91e-06
GRB170428136	1493349377	4.76	+56.23	1.47e-04
GRB170429799	1493493072	259.71	-32.77	1.68e-06
GRB170510217	1494393145	159.911	-39.328	1.07e-03
GRB170516808	1494962646	12.26	-6.41	6.79e-06
170710B	1499674206	43.122	+42.679	4.17e-06
GRB170710340	1499674207	43.122	+42.679	4.07e-06
170711A	1499811625	45.8	+47.849	1.76e-03
GRB170711931	1499811625	45.786	+47.85	1.76e-03
GRB170723882	1500844218	212.58	+39.83	2.04e-06
GRB170821265	1503296520	252.86	+19.11	1.31e-06
GRB170830328	1504079511	219.95	+32.41	2.22e-06
GRB170906030	1504658588	203.955	-47.101	1.66e-06
170906A	1504658591	203.955	-47.101	1.57e-06
GRB170915161	1505447490	120.26	-38.42	2.85e-06
GRB170916700	1505580451	98.43	+7.17	2.52e-06
GRB171008080	1507427678	232.59	+24.02	1.64e-06
GRB171009138	1507519100	348.14	+42.31	4.04e-04
171010B	1507669164	34.134	-54.391	2.68e-04
GRB171010875	1507669166	34.123	-54.41	2.67e-04
GRB171011162	1507693964	147.87	-9.8	2.26e-06
GRB171011810	1507749987	177.04	+26.93	4.31e-06
GRB171013350	1507883082	171.28	-26.64	1.60e-06
GRB171023097	1508725186	325.36	-30.4	1.38e-06
GRB171102107	1509590015	187.73	+54.03	2.50e-06
GRB171108656	1510155886	109.952	+29.091	2.45e-06
GRB171215705	1513356925	19.68	+34.73	5.09e-06
GRB171230048	1514596188	246.73	+13.09	5.19e-06
GRB171230119	1514602286	325.29	-12.35	1.51e-06
180111A	1515688926	149.78	+48.267	1.44e-05
180113A	1515811626	19.211	+68.682	3.98e-05
GRB180113116	1515811626	19.215	+68.682	3.98e-05
GRB180116026	1516063012	215.655	+18.959	1.28e-06
GRB180120207	1516424293	151.77	+27.79	5.06e-05
GRB180128215	1517116196	12.26	-26.1	1.68e-06
180224A	1519510867	202.684	+38.079	2.36e-06
180311A	1520791429	3.388	-54.491	4.43e-05
GRB180416924	1523916611	353.54	+74.63	9.74e-04
GRB180417689	1523982765	309.2	-19.51	1.29e-06
GRB180420107	1524191634	83.23	-25.25	1.11e-02
GRB180524920	1527199502	83.75	+30.11	3.72e-04
GRB180528465	1527505789	206.46	+30.18	6.51e-05

Table 5.2: 600 second CAL upper limits for Fermi-GBM and Swift GRBs. Same as Table 5.1 for time windows $[T_0 + 0.1 \text{ s}, T_0 + 600 \text{ s}]$.

Event	T_0	α	δ	U.L.
GRB151210041	1449709156	293.97	-42.7	3.64E-07
GRB151227218	1451193228	287.89	+31.94	9.73E-07
151229A	1451371827	329.37	-20.732	4.95E-05
GRB151229285	1451371827	329.37	-20.732	4.95E-05
GRB151229486	1451389206	346.49	+6.91	2.06E-07
GRB151231568	1451569088	150.08	+28.81	1.38E-06
GRB160106948	1452120330	181.61	+17.45	7.91E-07
GRB160107931	1452205241	299.67	+6.413	5.96E-06
160203A	1454465590	161.951	-24.789	5.50E-06
GRB160223416	1456221541	94.994	+33.407	8.25E-06
GRB160225720	1456420600	80.59	-9.19	2.85E-07
GRB160228034	1456620532	32.21	+39.38	4.39E-06
GRB160316139	1458098384	355.33	-52.38	5.08E-05
GRB160419637	1461078995	16.424	-27.343	8.41E-07
160419A	1461078997	16.418	-27.341	8.43E-07
GRB160530667	1464624071	133.48	+43.48	6.84E-06
GRB160628136	1467083781	87.92	+38.17	1.05E-05
GRB160629930	1467238778	4.864	+76.967	1.97E-05
160705B	1467752527	168.109	+46.7	3.25E-06
GRB160715298	1468566551	293.73	+21.887	2.23E-07
GRB160720767	1469039036	42.65	+75.68	9.63E-07
GRB160721806	1469128858	38.15	+34.52	1.60E-07
GRB160724444	1469356802	56.42	+16.23	1.11E-06
160726A	1469496847	98.809	-6.617	4.66E-07
GRB160726065	1469496847	98.821	-6.644	4.66E-07
160801A	1470043710	212.763	+13.489	3.63E-07
GRB160818230	1471498253	163.6	+37.4	3.71E-07
160824A	1472080945	80.088	+40.028	2.26E-07
GRB160909061	1473384476	242.68	-51.16	3.03E-07
GRB160910722	1473527979	221.442	+39.067	9.73E-04
GRB160917921	1474149937	145.68	+22.95	1.53E-07
161001A	1475283916	71.92	-57.261	8.83E-06
GRB161001045	1475283916	71.918	-57.261	8.83E-06
161004B	1475622479	112.151	-39.898	1.16E-02
161104A	1478252546	77.894	-51.46	8.20E-07
GRB161105417	1478340048	249.25	-65.217	2.81E-06
GRB161109263	1478672325	157.86	+61.8	2.66E-06
161129A	1480403499	316.227	+32.135	1.94E-06

Table 5.2 cont.'d

Event	T_0	α	δ	U.L.
GRB161129300	1480403499	316.229	+32.136	1.94E-06
161202A	1480720372	356.903	+19.646	1.61E-03
GRB161207224	1481088167	294.81	-9.93	9.78E-07
GRB161217128	1481943825	216.63	+51.98	6.04E-07
161218A	1482032856	245.25	-4.113	9.95E-07
GRB161228405	1482918205	358.42	-24.6	2.10E-07
GRB170121133	1484968252	241.99	+13.81	1.50E-07
GRB170121614	1485009862	72.84	-12.65	3.78E-07
GRB170124874	1485291486	282.04	-75.51	6.60E-07
GRB170131969	1485904499	341.447	+64.006	9.67E-05
170131A	1485904513	341.447	+64.006	5.10E-05
GRB170219002	1487462587	54.843	+50.072	7.34E-07
GRB170228773	1488306780	355.94	+15.73	2.08E-07
170307A	1488918261	13.51	+9.538	1.41E-07
GRB170307851	1488918317	13.535	+9.537	1.45E-07
GRB170313125	1489374028	359.62	+29.27	8.12E-07
170317A	1489743959	93.062	+50.493	1.81E-05
GRB170323058	1490232203	145.19	-39	2.93E-04
170330A	1490912991	283.331	-13.431	1.70E-06
GRB170405777	1491417562	219.81	-25.244	9.54E-07
170405A	1491417588	219.828	-25.243	8.07E-07
GRB170412917	1492034447	201.75	+25.28	2.10E-07
GRB170412988	1492040575	164.38	+22.03	5.48E-07
GRB170428136	1493349377	4.76	+56.23	1.02E-05
170428A	1493370822	330.078	+26.916	1.23E-06
GRB170429799	1493493072	259.71	-32.77	2.19E-07
GRB170510217	1494393145	159.911	-39.328	1.04E-03
GRB170516808	1494962646	12.26	-6.41	1.48E-07
170519A	1495170602	163.427	+25.374	1.48E-06
170531B	1496268129	286.884	-16.418	2.99E-07
170710B	1499674206	43.122	+42.679	2.58E-06
GRB170710340	1499674207	43.122	+42.679	2.58E-06
170711A	1499811625	45.8	+47.849	2.19E-06
GRB170711931	1499811625	45.786	+47.85	2.19E-06
GRB170723882	1500844218	212.58	+39.83	8.11E-07
GRB170726794	1501095779	297.78	+6.62	4.38E-05
GRB170816258	1502863871	10.7	-15.61	9.36E-03
GRB170821265	1503296520	252.86	+19.11	1.45E-07
GRB170830328	1504079511	219.95	+32.41	1.82E-07
GRB170906030	1504658588	203.955	-47.101	4.84E-07
170906A	1504658591	203.955	-47.101	4.84E-07

Table 5.2 cont.'d

Event	T_0	α	δ	U.L.
170912A	1505180056	167.373	-54.326	2.48E-06
GRB170915161	1505447490	120.26	-38.42	1.01E-06
GRB170916700	1505580451	98.43	+7.17	9.15E-07
GRB171008080	1507427678	232.59	+24.02	2.45E-07
GRB171009138	1507519100	348.14	+42.31	3.15E-04
171010B	1507669164	34.134	-54.391	2.66E-06
GRB171010875	1507669166	34.123	-54.41	2.66E-06
GRB171011162	1507693964	147.87	-9.8	3.09E-07
GRB171011810	1507749987	177.04	+26.93	4.31E-06
GRB171013350	1507883082	171.28	-26.64	3.77E-07
GRB171023097	1508725186	325.36	-30.4	6.36E-07
GRB171102107	1509590015	187.73	+54.03	3.83E-07
GRB171108656	1510155886	109.952	+29.091	3.57E-07
GRB171119992	1511135307	135.51	-46.99	7.96E-04
GRB171215705	1513356925	19.68	+34.73	9.81E-07
171216A	1513393619	211.991	-50.485	1.34E-06
GRB171222684	1513959910	148.277	+35.627	2.38E-04
GRB171230048	1514596188	246.73	+13.09	1.69E-06
GRB171230119	1514602286	325.29	-12.35	1.34E-07
180111A	1515688926	149.78	+48.267	1.27E-06
180113A	1515811626	19.211	+68.682	2.12E-05
GRB180113116	1515811626	19.215	+68.682	2.12E-05
GRB180116026	1516063012	215.655	+18.959	1.43E-07
GRB180120207	1516424293	151.77	+27.79	3.87E-05
GRB180127049	1517015472	20.48	+25.79	2.79E-06
GRB180128215	1517116196	12.26	-26.1	3.02E-07
GRB180130744	1517334686	136.83	+52.69	4.99E-07
180224A	1519510867	202.684	+38.079	2.24E-07
GRB180227211	1519707856	98.61	-5.44	1.65E-04
180311A	1520791429	3.388	-54.491	2.80E-07
GRB180314030	1520988199	99.265	-24.496	2.68E-05
180314A	1520988211	99.265	-24.496	2.68E-05
180324A	1521866229	76.527	+56.714	1.44E-06
180407A	1523066089	35.236	+33.513	3.07E-07
GRB180416924	1523916611	353.54	+74.63	5.04E-06
GRB180417689	1523982765	309.2	-19.51	1.89E-07
GRB180420031	1524185109	93.51	-28.32	3.18E-03
GRB180420107	1524191634	83.23	-25.25	1.02E-04
GRB180506077	1525571425	249.38	+5.08	3.58E-07
GRB180524920	1527199502	83.75	+30.11	6.38E-05
GRB180528465	1527505789	206.46	+30.18	1.97E-05

Table 5.3: CAL maximum upper limits for CGBM GRBs. Maximum upper limits inferred from CAL observations on CGBM on-board triggers without reliable localization from other instruments for one-minute and ten-minute time windows.

Event	UTC Time [s]	U.L. [erg cm^{-2} s^{-1}] (60 s)	(600 s)	Also detected by
GRB 160307A	1457313514	1.57E-06	1.80E-07	
GRB 160324A	1458835117	1.26E-06	1.28E-07	INTEGRAL-SPI, Konus-Wind
GRB 160508A	1462717951	1.27E-06	1.38E-07	INTEGRAL-SPI, Konus-Wind
GRB 160525C	1464173660	1.29E-06	7.19E-07	Konus-Wind
GRB 160608A	1465373783	1.95E-06	3.60E-07	
GRB 160624B	1466764854	2.39E-06	5.49E-07	
GRB 160814A	1471209162	1.29E-06	1.35E-07	MAXI, Konus-Wind
GRB 160908A	1473311820	1.49E-06	2.23E-07	INTEGRAL-SPI, Konus-Wind
GRB 161203A	1480790467	1.86E-06	1.38E-07	INTEGRAL-SPI, Konus-Wind
GRB 161207A	1481143380	1.27E-06	4.83E-07	Fermi-GBM
GRB 170626B	1498438676	1.32E-06	4.89E-07	Konus-Wind
GRB 170702A	1499038895	1.27E-06	1.67E-07	Swift, INTEGRAL-SPI
GRB 170703A	1499071445	1.29E-06	3.43E-07	Konus-Wind
GRB 170708B	1499546214	1.34E-06	1.42E-07	Konus-Wind
GRB 170710D	1499713970	1.75E-06	1.44E-07	Konus-Wind
GRB 171011B	1507683936	1.98E-06	1.80E-07	INTEGRAL-SPI, Konus-Wind
GRB 171101A	1509533387	1.84E-06	3.96E-07	INTEGRAL-SPI
GRB 171212C	1513119217	1.36E-06	4.35E-07	Konus-Wind
GRB 171229A	1514541577	4.57E-06	4.57E-06	INTEGRAL-SPI, Konus-Wind
GRB 180112A	1515774548	1.36E-06	1.36E-07	INTEGRAL-SPI, Konus-Wind
GRB 180411B	1523435849	1.30E-06	1.71E-07	INTEGRAL-SPI, Konus-Wind
GRB 180523A	1527099626	1.33E-06	1.80E-07	INTEGRAL-SPI

5.3 Unknown Transient Search

For transient events where the location is known, through association with a known source or with additional localization information from other experiments, the detection of a single photon coincident with the known could, depending on the background, be sufficient to establish the detection of a high-energy counterpart. On the other hand, the detection of a transient event with unknown location requires multiple coincident photons within some time window to establish a correlation. In this section, a method for identifying such a signal and the sensitivity of the CAL based on the instrument response to such an event is presented.

5.3.1 Algorithm and Sensitivity

Central to the task of identifying unlocalized transients is the association of multiple events based on their spatial separation. As seen in Section 3.4.3, the angular separation over which two events with trajectories reconstructed in the CAL can be considered coincident with a given probability is dependent on the primary energies and the minimum number of layers used in the tracking, N_p, of each event. Supposing that we have found two events in a set time window, the value of the scaling function S_p can be determined for each. This provides a means for translating between a true angular separation from a source position and the scaled angular error according to Equation 3.5.

The PSF is the probability density for an event trajectory to be reconstructed at a scaled angular distance x from the true incident direction. To check the consistency of the two events having originated from a common source, a sampling method taking into account both of the detected events is used. For each sample, a value of x is randomly drawn from the PSF for each of the events. Scaling each of these back to a real angular error according to the appropriate values of S_p provides polar angles, θ_1 and θ_2. Azimuthal angles are drawn from a uniform distribution on $[0, 2\pi)$ as well, ϕ_1 and ϕ_2. The (θ, ϕ) pair for each event and each sample represent one possible place the event could be reconstructed relative to an unspecified source position.

The angular separation between the hypothetical positions is calculated through simple geometry and is stored as the result of the sample. This process is repeated to build up an empirical probability density function in angular separation given the parameters of the two events. If the observed angular separation between the events in celestial coordinates is less than the 68% containment radius (or other confidence level) of the distribution, the events are considered to be associated.

To test the false alarm rate (FAR) of this method, the LE-γ flight data sample is divided into consecutive windows of 100 seconds each. Each window is checked for multiple events and, if applicable, the sampling method is applied to test their association. This division

represents 100,884 trials for the search, within which 25 pairs were found, corresponding to a FAR of 0.025%. Checking for 10,351 time windows of 10 minutes each, 50 pairs were found, increasing the FAR to 0.48%. It should be noted that these are conservative estimates because of the use of real flight data. Real pairs not previously identified could be included. Furthermore, the full FOV was included in this test, so unhandled ISS structure background is also potentially present.

The resulting sensitivity is evaluated using simulated GRB events with assumed E^{-2} spectra and t^{-1} time-dependence at an assumed zenith angle. These simulated GRB events are injected into the flight data and processed through the transient search algorithm. Figure 5.2 shows for CC Track the limiting energy flux for which 90% of simulated events are identified. For comparison, the light curves of short GRB 090510 (Fermi-LAT Collaboration, 2017) and long GRB 130427A (Ackermann et al., 2013b) as measured by Fermi-LAT are shown. Note that the energy range used for the plot is 0.1 - 100 GeV due to these being the reported quantities for the LAT light curves despite the CC Track range being [1 GeV, 10 GeV]. For the energy range 1 - 10 GeV only, the sensitivity is improved by approximately a factor of 3. For an event such as GRB 130427A, taking the energy-dependence and time-dependence of the flux in Tam et al. (2013), if the trigger time were near the center of the CAL FOV, the CAL could expect to localize the source with $\sim$3 photon events.

5.3.2 Automation

The automated application of the transient search algorithm to the flight data is being developed and tested at the Waseda CALET Operations Center (WCOC) with the eventual goal of providing near-real-time alerts to the wider gamma-ray community. Upon receipt of the Level 0 data (Section 4.1.1), the process to convert to Level 1 is automatically triggered. The LE-γ dataset is then processed to Level 2 and searched for candidate events, which are then tested with the transient search pipeline and flagged for further analysis if passing.

A challenge to the automated implementation is the time-consuming process of converting the data to Level 2 (currently requiring 10 CPU-hours of processing time per 1 hour

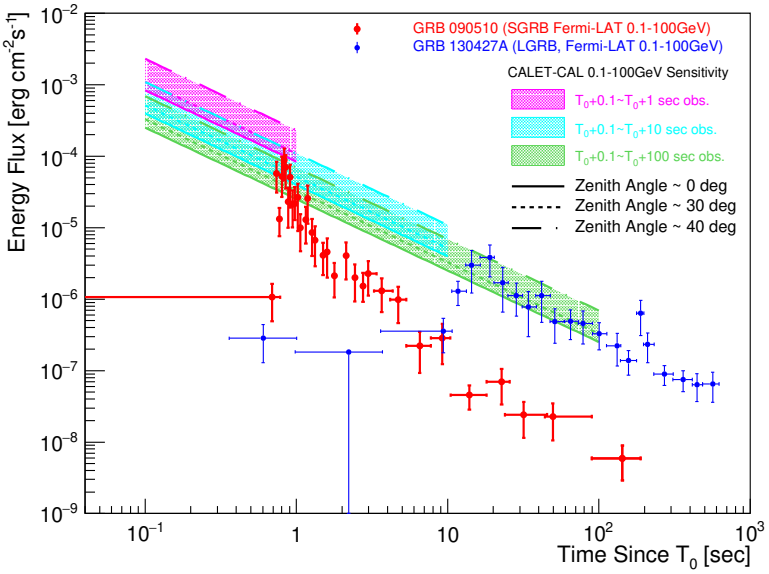

Figure 5.2: Derived limiting energy flux of the blind transient search algorithm at various assumed zenith angles using CC Track. For comparison, a short GRB (GRB 090510) and a long GRB (GRB 130427A) as measured by Fermi-LAT are shown in red and blue, respectively.

of flight data). The conversion process has been modified to split the dataset and process these in parallel in order to mitigate the actual time impact of the process. The prototype system is in the validation stages on the main WCOC data handling server and is expected to be available for the LIGO/Virgo O3 science run.

Chapter 6. Conclusions

In addition to its primary cosmic ray observation targets, the CALET instrument is sensitive to a broad range of photons, from x-rays to soft gamma rays with CGBM, and at GeV energies with the CAL. This broadband coverage provides another eye to the sky for the detection and localization of transient events at a critical time, when multi-wavelength follow-up observations to GW events can provide important new insights to the environments of sGRBs and the mechanisms responsible for the high-energy emission of GRBs in general. In this work, the capabilities of the CAL for gamma-ray observations, the resulting sensitivity to GRB counterparts based on Fermi-LAT observations, and the current status of the high-energy transient search were presented.

From detailed simulations with high statistics, the instrument response functions are carefully considered. The effective area as a function of energy and direction relative to the instrument is determined using an event selection tuned for performance at energies 1 GeV $< E <$ 100 GeV. Using two track reconstruction algorithms, the angular resolution and the resulting PSF are derived and the dependence of this response on event incidence angle is investigated. Using the first two years of flight data, these results are validated through analysis of bright point sources and through consistency with measurements from Fermi-LAT. The potential for analysis of long-term flaring systems is demonstrated through the CAL observations of the AGN CTA 102.

One major obstacle to current CAL gamma-ray observations previously discussed is the unexpected background of secondary photons from cosmic-ray interactions in ISS structures. Removal of static obstructions from all aspects of the analysis has been achieved, but a full, time-dependent characterization of moving elements such as the SSRMS robotic arm are still under development. While the motion of the solar panels and radiators are predictable and verifiable, and have been used to veto individual events based on their arrival direction, the incorporation of this information into the calculation of long-term exposures is extremely computationally expensive and requires further consideration. Furthermore,

energy-dependent effects based on the angular resolution of the CAL for removing these secondaries present yet another challenge.

In spite of these complications, comparing to the high-energy emission measured previously by other instruments, the derived instrument response functions establish the potential for CAL observations of GRB counterparts. The methodology and null result of searches corresponding to CGBM, Fermi-GBM, and Swift are presented, and the flux sensitivity for potential future observations is calculated. An algorithm for detection of transient events not localized by external measurements has been developed, and a system for near-real time checks of the CAL data with this method is in testing at the WCOC.

The ability of CALET to quickly follow-up on GW triggers by LIGO and Virgo and to provide further localization information in the case of a detection complements the efforts being made by other gamma ray detectors worldwide. For the groundbreaking multi-wavelength observation of the GW170817 event, the coincident detection of GRB 170817A by Fermi-GBM constrained the source region beyond the capabilities of LIGO/Virgo and enabled the successful optical detection. The science value of such cooperative observation campaigns is unquestionable. Through the multi-messenger study of the GW170817 system, the identification of (at least some) sGRB progenitors as binary neutron star mergers and the confirmation of a resulting kilonova advanced the understanding of these systems. Future observations are necessary to answer new and outstanding questions pertaining to the universality of this origin for sGRBs and to further the understanding of the high-energy emission from GRB systems. In the upcoming third observation run for the GW detectors, CALET will be ready to participate fully in this campaign.

References

Aab, A. et al., Observation of a large-scale anisotropy in the arrival directions of cosmic rays above $8 \times 10^1 8$ eV, Science 357, 6357, 1266 (2017).

Abbott, B.P. et al., GW151226: Observation of gravitational waves from a 22-solar-mass black hole binary coalescence, Phys. Rev. Lett. 116, 241103 (2016).

Abbott, B.P. et al., Gravitational waves and gamma-rays from a binary neutron star merger: GW170817 and GRB 170817A, Astrophys. J. Letters 848, 2 (2017).

Abbott, B.P. et al., GW170104: Observation of a 50-solar-mass binary black hole coalescence at redshift 0.2, Phys. Rev. Lett. 118, 221101 (2017).

Abbott, B.P. et al., GW170608: Observation of a 19 solar-mass binary black hole coalescence, Astrophys. J. Letters 851, 2 (2017).

Abbott, B.P. et al., GW170814: A three-detector observation of gravitational waves from a binary black hole coalescence, Phys. Rev. Lett. 119, 141101 (2017).

Abbott, B.P. et al., GW170817: Observation of gravitational waves from a binary neutro n star inspiral, Phys. Rev. Lett. 119, 161101 (2017).

Abdo, A.A. et al., Fermi Large Area Telescope observations of the Crab Pulsar and Nebula, Astrophys. J. 708, 1254 (2009).

Abdo, A.A. et al., Fermi-LAT observations of the Geminga Pulsar, Astrophys. J. 720, 272 (2010).

Abdo, A.A. et al., Fermi Large Area Telescope observations of the Vela Pulsar, Astrophys. J. 696, 1084 (2009).

Ackermann, M. et al., Fermi LAT observations of cosmic-ray electrons from 7 GeV to 1 TeV, Phys. Rev. D 82, 092004 (2010).

Ackermann, M. et al., Detection of a spectral break in the extra hard component of GRB 090926A, Astrophys. J. 729, 114 (2011).

Ackermann, M. et al., The Fermi Large Area Telescope on orbit: event classification, instrument response functions, and calibration, Astrophys. J. Suppl. Ser. 203, 4 (2012).

Ackermann, M. et al., The first Fermi-LAT gamma-ray burst catalog, Astrophys. J. Suppl. Ser. 209, 90 (2013).

Ackermann, M. et al., Fermi-LAT observations of the gamma-ray bursts GRB130427A, Science 343 (6166), 42 (2013).

Adriani, O. et al., Reentrant albedo proton fluxes measured by the PAMELA experiment, J. Geophys. Res. 120, 5, 3728 (2015).

Adriani, O. et al., CALET upper limits on x-ray and gamma-ray counterparts of GW151226, Astrophys. J. Letters 829, 20 (2016).

Adriani, O. et al., Energy spectrum of cosmic-ray electron and positron from 10 GeV to 3 TeV observed with the Calorimetric Electron Telescope on the International Space Station, Phys. Rev. Lett. 119, 181101 (2017).

Adriani, O. et al., Extended measurement of cosmic-ray electron and positron spectrum from 11 GeV to 4.8 TeV with the Calorimetric Electron Telescope on the International Space Station, Phys. Rev. Lett. 120, 261102 (2018).

Adriani, O. et al., Search for GeV gamma-ray counterparts of gravitational wave events by CALET, accepted in Astrophys. J., pre-print: https://arxiv.org/abs/1807.01435 (2018).

Aguilar, M. et al., The Alpha Magnetic Spectrometer (AMS) on the International Space Station: Part I. Results from the test flight on the space shuttle, Phys. Rep. 366, 331 (2002).

Aguilar, M. et al., Precision measurement of the proton flux in primary cosmic rays from rigidity 1 TV to 1.8 TV with the Alpha Magnetic Spectrometer on the International Space Station, Phys. Rev. Lett. 114, 171103 (2015).

Akaike, Y. et al., CALET observational performance expected by CERN beam test, Proceedings of the 33rd ICRC (Rio de Janeiro), #0726 (2013).

Ansoldi, S. et al., The blazar TXS 0506+056 associated with a high-energy neutrino: insights into extragalactic jets and cosmic-ray acceleration, Astrophys. J. Letters 863, 10 (2018).

Asaoka, Y. et al., Energy calibration of CALET onboard the International Space Station, Astroparticle Physics 91, 1 (2017).

Asaoka, Y. et al., On-orbit operations and offline data processing of CALET onboard the ISS, Astroparticle Physics 100, 29 (2018).

Becerra, J. et al., Fermi-LAT detection of strong flaring activity from the FSRQ CTA 102, The Astronomer's Telegram, No. 8722 (2016).

Cannady, N. et al., Gamma-ray observations with CALET: exposure map, response functions, and simulated results, Proceedings of Science (ICRC 2015) 995 (2015).

Cannady, N. et al., Characteristics and performance of the CALorimetric Electron Telescope (CALET) calorimeter for gamma-ray observations, Astrophys. J. Supp. Ser., submitted (2018).

Chang, J. et al., An excess of cosmic ray electrons at energies of 300 - 800 GeV, Nature 456, 20 (2008).

Ciprini, S., Fermi LAT observation of renewed and strong GeV gamma-ray activity from blazar CTA 102, The Astronomer's Telegram, No. 9869 (2016).

Coulter, D.A. et al., LIGO/Virgo G298048: Potential optical counterpart discovered by Swope telescope, GCN 21529 (2017).

Feldman, G.J. and Cousins, R.D., Unified approach to the classical statistical analysis of small signals, Phys. Rev. D 57, 7 (1998).

The Fermi-LAT Collaboration, Fermi Large Area Telescope third source catalog, arXiv.org e-prints, arXiv:1501.02003v3 (2015).

Fermi-LAT Collaboration, Fermi-LAT observations of the LIGO/Virgo event GW170817, arXiv.org e-prints, arXiv:1710.05450v1 (2017).

Gonzàlez et al., A γ-ray burst with a high-energy spectral component inconsistent with the synchrotron shock model, Nature 424, 749 (2003).

Górski, K.M. et al., HEALPix: A framework for high-resolution discretization and fast analysis of data distributed on the sphere, Astrophys. J. 622, 759 (2005).

Honda, M. et al., New calculation of the atmospheric neutrino flux in a three-dimensional scheme, PRD 70, 043008 (2004).

The IceCube Collaboration et al., Multi-messenger observations of a flaring blazar coincident with high-energy neutrino IceCube-170922A, Science 361, 146 (2018).

Jørgensen, J.L. and Liebe, C.C., The advanced stellar compass, development and operations, Acta Astronatica 39, 775 (1996).

Kasahara, K., Introduction to COSMOS and some relevance to ultra high-energy cosmic ray air showers, Proceedings of the 24th ICRC (Rome), 1, 399 (1995).

King, I., The structure of star clusters. I. an empirical density law, Astron. J. 67, 471 (1962).

Kouveliotou, C. et al., Identification of two classes of gamma-ray bursts, Astrophys. J. Letters, 413, 101 (1993).

Maestro, P. et al., Particle tracking in the CALET experiment, Proceedings of Science (ICRC 2017) 208 (2017).

Merck, M. et al., Observations of High-Energy Gamma-ray Bursts with EGRET, Proceedings of the IAU Colloquium No. 151: Flares and Flashes (Sonneberg 1994) XXII, 477 (1994).

Moiseev, A. et al., CALET perspectives in high-energy gamma-ray observations, Proceedings of the 33rd ICRC (Rio de Janeiro), #0627 (2013).

Mori, M. et al., Expected performance of CALET as a high-energy gamma-ray observatory, Proc. of 33rd ICRC (Rio de Janeiro), #0248 (2013).

Nava, L., High-energy emission from gamma-ray bursts, International Journal of Modern Physics D, retrieved from arXiv.org on April 5, 2018, https://arxiv.org/abs/1804.01524.

Picozza, P. et al., PAMELA - A payload for antimatter matter exploration and light-nuclei analysis, Astroparticle Physics 27, 4, 296 (2007).

Sullivan, J.D., Nucl. Instrum. and Meth., 95, 5 (1971).

Shoemake, K., Animating rotation with quaternion curves, Proceedings of SIGGRAPH85 12th Annual Conference on Computer Graphics 245 (1985).

Shepherd, S.G., Altitude-adjusted corrected geomagnetic coordinates: Definition and functional approximations, J. Geophys. Res. Space Physics, 119, 1 (2014).

Spurio, M., 2015, Particles and Astrophysics, 1st ed., Switzerland, Springer International Publishing.

Tam, P. et al., Discovery of an extra hard spectral component in the high-energy afterglow emission of GRB 130427A, Astrophys. J. Letters 771, 1 (2013).

Tamura, T. et al., Particle beam tests of the Calorimetric Electron Telescope, Proceedings of the 33rd ICRC (Rio de Janeiro), #0986 (2013).

Torii, S. et al., The CALorimetric Electron Telescope (CALET): High Energy Astroparticle Physics Observatory on the International Space Station, Proceedings of Science (ICRC 2015) 581 (2015).

Veres, P. et al., Gamma-ray burst models in light of the GRB 170817A - GW170817 connection, arXiv.org e-prints, arXiv:1802.07328v1 (2018).

Yamamoto, M. et al., Search for cosmic-ray antiproton origins and for cosmological antimatter with BESS, Advances in Space Research 51, 2, 227 (2013)

Yamaoka, K. et al., CALET GBM Observations of Gamma-ray Bursts and Gravitational Wave Sources, Proceedings of Science (ICRC 2017) 614 (2017).

Yoon, Y.S. et al., Proton and helium spectra from the CREAM-III flight, Astrophys. J. 839, 1 (2017).

Yoshida, K. et al., Cosmic-ray electron spectrum above 100 GeV from PPB-BETS experiment in Antarctica, Advances in Space Research 42, 10, 1670 (2008).

Vita

Nicholas Cannady was born in Poplar Bluff, Missouri in July 1988. Although he was raised primarily in rural Liddieville, LA, many of his childhood summers were spent playing in his grandparents' garden in northeastern Arkansas. He attended the Louisiana School for Math, Science, and the Arts in Natchitoches, Louisiana for his final two years of high school, graduating in May 2006. He received two undergraduate B.S. degrees in Physics (Astronomy) and Mathematics from Louisiana State University in Baton Rouge in May 2011. He lives in Baton Rouge, Louisiana with his partner Laura and their two cats while pursuing his doctorate in Physics under Michael L. Cherry.